

Marco Ariola  
Alfredo Pironti

AIC

Advances in  
Industrial Control

# Magnetic Control of Tokamak Plasmas



Springer

# Advances in Industrial Control

## Other titles published in this series:

*Digital Controller Implementation and Fragility*

Robert S.H. Istepanian and James F. Whidborne (Eds.)

*Optimisation of Industrial Processes at Supervisory Level*

Doris Sáez, Aldo Cipriano and Andrzej W. Ordys

*Robust Control of Diesel Ship Propulsion*

Nikolaos Xiros

*Hydraulic Servo-systems*

Mohieddine Jelali and Andreas Kroll

*Model-based Fault Diagnosis in Dynamic Systems Using Identification Techniques*

Silvio Simani, Cesare Fantuzzi and Ron J. Patton

*Strategies for Feedback Linearisation*

Freddy Garces, Victor M. Becerra, Chandrasekhar Kambhampati and Kevin Warwick

*Robust Autonomous Guidance*

Alberto Isidori, Lorenzo Marconi and Andrea Serrani

*Dynamic Modelling of Gas Turbines*

Gennady G. Kulikov and Haydn A. Thompson (Eds.)

*Control of Fuel Cell Power Systems*

Jay T. Pukrushpan, Anna G. Stefanopoulou and Hwei Peng

*Fuzzy Logic, Identification and Predictive Control*

Jairo Espinosa, Joos Vandewalle and Vincent Wertz

*Optimal Real-time Control of Sewer Networks*

Magdalene Marinaki and Markos Papageorgiou

*Process Modelling for Control*

Benoît Codrons

*Computational Intelligence in Time Series Forecasting*

Ajoy K. Palit and Dobrivoje Popovic

*Modelling and Control of Mini-Flying Machines*

Pedro Castillo, Rogelio Lozano and Alejandro Dzul

*Ship Motion Control*

Tristan Perez

*Hard Disk Drive Servo Systems (2nd Ed.)*

Ben M. Chen, Tong H. Lee, Kemao Peng and Venkatakrishnan Venkataramanan

*Measurement, Control, and Communication Using IEEE 1588*

John C. Eidson

*Piezoelectric Transducers for Vibration Control and Damping*

S.O. Reza Moheimani and Andrew J. Fleming

*Manufacturing Systems Control Design*

Stjepan Bogdan, Frank L. Lewis, Zdenko Kovačić and José Mireles Jr.

*Windup in Control*

Peter Hippe

*Nonlinear  $H_2/H_\infty$  Constrained Feedback Control*

Murad Abu-Khalaf, Jie Huang and Frank L. Lewis

*Practical Grey-box Process Identification*

Torsten Bohlin

*Control of Traffic Systems in Buildings*

Sandor Markon, Hajime Kita, Hiroshi Kise and Thomas Bartz-Beielstein

*Wind Turbine Control Systems*

Fernando D. Bianchi, Hernán De Battista and Ricardo J. Mantz

*Advanced Fuzzy Logic Technologies in Industrial Applications*

Ying Bai, Hanqi Zhuang and Dali Wang (Eds.)

*Practical PID Control*

Antonio Visioli

(continued after Index)

Marco Ariola • Alfredo Pironti

# Magnetic Control of Tokamak Plasmas

 Springer

Marco Ariola, PhD  
Dipartimento per le Tecnologie  
Università degli Studi di Napoli Parthenope  
Centro Direzionale di Napoli, Isola C4  
80143 Napoli  
Italy

Alfredo Pironti, PhD  
Dipartimento di Informatica e Sistemistica  
Università degli Studi di Napoli Federico II  
Via Claudio 21  
80125 Napoli  
Italy

ISBN 978-1-84800-323-1

e-ISBN 978-1-84800-324-8

DOI 10.1007/978-1-84800-324-8

Advances in Industrial Control series ISSN 1430-9491

British Library Cataloguing in Publication Data  
Ariola, M.

Magnetic control of tokamak plasmas. - (Advances in industrial control)

1. Tokamaks 2. Feedback control systems 3. Electromagnetic induction

I. Title II. Pironti, Alfredo  
621.4'84

ISBN-13: 9781848003231

Library of Congress Control Number: 2008927412

© 2008 Springer-Verlag London Limited

Apart from any fair dealing for the purposes of research or private study, or criticism or review, as permitted under the Copyright, Designs and Patents Act 1988, this publication may only be reproduced, stored or transmitted, in any form or by any means, with the prior permission in writing of the publishers, or in the case of reprographic reproduction in accordance with the terms of licences issued by the Copyright Licensing Agency. Enquiries concerning reproduction outside those terms should be sent to the publishers.

The use of registered names, trademarks, etc. in this publication does not imply, even in the absence of a specific statement, that such names are exempt from the relevant laws and regulations and therefore free for general use.

The publisher makes no representation, express or implied, with regard to the accuracy of the information contained in this book and cannot accept any legal responsibility or liability for any errors or omissions that may be made.

*Cover design:* eStudio Calamar S.L., Girona, Spain

Printed on acid-free paper

9 8 7 6 5 4 3 2 1

springer.com

# **Advances in Industrial Control**

## **Series Editors**

Professor Michael J. Grimble, Professor of Industrial Systems and Director  
Professor Michael A. Johnson, Professor (Emeritus) of Control Systems and Deputy Director  
Industrial Control Centre  
Department of Electronic and Electrical Engineering  
University of Strathclyde  
Graham Hills Building  
50 George Street  
Glasgow G1 1QE  
United Kingdom

## **Series Advisory Board**

Professor E.F. Camacho  
Escuela Superior de Ingenieros  
Universidad de Sevilla  
Camino de los Descubrimientos s/n  
41092 Sevilla  
Spain

Professor S. Engell  
Lehrstuhl für Anlagensteuerungstechnik  
Fachbereich Chemietechnik  
Universität Dortmund  
44221 Dortmund  
Germany

Professor G. Goodwin  
Department of Electrical and Computer Engineering  
The University of Newcastle  
Callaghan  
NSW 2308  
Australia

Professor T.J. Harris  
Department of Chemical Engineering  
Queen's University  
Kingston, Ontario  
K7L 3N6  
Canada

Professor T.H. Lee  
Department of Electrical Engineering  
National University of Singapore  
4 Engineering Drive 3  
Singapore 117576

Professor Emeritus O.P. Malik  
Department of Electrical and Computer Engineering  
University of Calgary  
2500, University Drive, NW  
Calgary  
Alberta  
T2N 1N4  
Canada

Professor K.-F. Man  
Electronic Engineering Department  
City University of Hong Kong  
Tat Chee Avenue  
Kowloon  
Hong Kong

Professor G. Olsson  
Department of Industrial Electrical Engineering and Automation  
Lund Institute of Technology  
Box 118  
S-221 00 Lund  
Sweden

Professor A. Ray  
Pennsylvania State University  
Department of Mechanical Engineering  
0329 Reber Building  
University Park  
PA 16802  
USA

Professor D.E. Seborg  
Chemical Engineering  
3335 Engineering II  
University of California Santa Barbara  
Santa Barbara  
CA 93106  
USA

Doctor K.K. Tan  
Department of Electrical Engineering  
National University of Singapore  
4 Engineering Drive 3  
Singapore 117576

Professor Ikuo Yamamoto  
The University of Kitakyushu  
Department of Mechanical Systems and Environmental Engineering  
Faculty of Environmental Engineering  
1-1, Hibikino, Wakamatsu-ku, Kitakyushu, Fukuoka, 808-0135  
Japan

To Angela and to my family (M.A.)

To Teresa and Andrea (A.P.)



---

## Series Editors' Foreword

The series *Advances in Industrial Control* aims to report and encourage technology transfer in control engineering. The rapid development of control technology has an impact on all areas of the control discipline. New theory, new controllers, actuators, sensors, new industrial processes, computer methods, new applications, new philosophies..., new challenges. Much of this development work resides in industrial reports, feasibility study papers and the reports of advanced collaborative projects. The series offers an opportunity for researchers to present an extended exposition of such new work in all aspects of industrial control for wider and rapid dissemination.

Internationally, there is much concern about climate change, global warming, and environmental pollution. Two of the major issues are the world's reliance on fossil fuels (coal, oil, and gas) for energy production and the bludgeoning demand for energy as more nations become economically developed and the world becomes increasingly urbanized. If the technological challenges can be overcome, the use of nuclear fusion reactors could provide a sustainable and clean way of meeting the ever-increasing demand for energy in the long term. As evidenced by this monograph, it is inspiring to learn that control engineers are already deeply involved in the international experiments designed to explore the potential of this advanced energy production technology. The tokamak design of nuclear fusion reactor is at the centre of a new research programme, the International Thermonuclear Experimental Reactor (ITER) project and in this *Advances in Industrial Control* monograph, Marco Ariola and Alfredo Pironti explore the problems of tokamak plasma control.

Despite the esoteric technology of tokamak nuclear fusion reactors, there is much that is familiar to the process control or industrial control engineer in this volume; for example, these nuclear fusion reactors have an operational profile that can be divided into the stages of start-up, steady-state and shut-down. The steady-state operational phase is characterized by high-performance control to achieve stable, efficient, and optimized operation whilst meeting the demanding objective of accurate spatial plasma distribution. A key preliminary in any process control project is a study of the process and the authors provide a concise and clear introduction to the basics of plasma physics and models in Part I of the monograph;

this part is supported by two useful appendices on some of the mathematical tools used and the physical units of plasma physics. State-space models, state observers,  $H_\infty$  control, and process simulations are some of the familiar techniques used by the authors to meet the demanding spatial control specifications for these processes; however, the research reported in the monograph is more than just simulation studies and proposals for possible future hypothetical controllers, for the authors have worked with some of the world's leading existing tokamak facilities. Chapter 5, 8, and 9 respectively, give practical results of implementations of their control schemes on the FTU Tokamak (Italy), the TCV Tokamak (Switzerland), and the JET Tokamak (United Kingdom). Additionally, the authors present simulation results of their ideas for the control of the new tokamak proposed for the ITER project.

In conclusion, being very aware that most control engineers will not be conversant with the complexities of tokamak nuclear fusion reactor control, the authors have taken special care to give a useful introduction to the background of nuclear fusion, the science of plasma physics and appropriate models in the first part of the monograph (Chapters 1 to 3). This introduction is followed by six chapters (4 to 9) of control studies. In Chapter 4, the generic control problem is established and then five case study chapters follow. These later chapters marry different aspects of the control problem with actual practical results from the different tokamak installations mentioned above. This well structured and staged presentation should make this important and fascinating application accessible to a wide range of readers including process and industrial engineers, academic researchers and postgraduate students in the control and power disciplines.

Industrial Control Centre  
Glasgow  
Scotland, UK  
2008

*M.J. Grimble*  
*M.A. Johnson*

---

## Preface

This book offers a thorough coverage of the magnetic control of a plasma in a tokamak. A plasma is a gas in which an important fraction of the particles is ionized, so that the electrons and ions are separately free; tokamaks are devices constructed in the shape of a torus (or doughnut), in which the plasma is confined by means of magnetic fields. Tokamaks have been proved to be the most promising approach to obtaining energy production from nuclear fusion. For nuclear fusion to happen in a plasma, it is necessary to heat the plasma to a sufficiently high temperature of around 100 million degrees centigrade: this motivates the need for devices in which the plasma is restricted to a finite spatial region without any physical boundary. In a tokamak the confinement is obtained through balancing the expansion pressure in the plasma with the forces exerted by a magnetic field produced by currents flowing in a number of circuits surrounding the plasma. The equilibrium between these forces is such that the plasma assumes the geometrical form of a ring inside the vacuum chamber of the tokamak. The importance of tokamaks for the future of nuclear fusion is demonstrated by the decision to build a new experimental facility, called ITER, as a joint effort by most of the industrialized countries in the world. ITER, whose cost is estimated at about 10 billion euros, will be in operation in 2016, and it is expected to open the way to the commercial exploitation of nuclear fusion.

The magnetic control system is a feedback system, sometimes divided into separate sub-systems, that has the aim of guaranteeing that the plasma equilibrium inside the tokamak is maintained with a prescribed position and shape of the plasma ring. The design of this control system is the main topic of this book. Historically the first problem that was faced was the vertical stabilization of the plasma. Indeed, physical studies demonstrated that the efficiency of the confinement configuration was improved if the plasma exhibited a vertically elongated shape. Unfortunately, with this elongated configuration the equilibrium turned out to be unstable. This problem was tackled using a simple SISO (single-input–single-output) loop, typically with a PID (proportional–integral–derivative) controller whose gains were experimentally

tuned. Following this, simple stabilization of the plasma was no longer enough for the experimental activities, and the problem of controlling the overall shape of the plasma gained more and more importance. As a matter of fact, at present, for most tokamak devices there are programmes aimed at improving the performance of the magnetic control systems. This improvement is being achieved with a substantial paradigm shift, from an empirical design approach to a more formal, model-based design approach.

Models deriving from a description of the interaction between the plasma and the circuits are described in terms of a set of nonlinear partial differential equations. The main modelling problem is then that of introducing physical simplifying assumptions and of using approximate numerical methods to obtain a model detailed enough to catch the principal phenomena, but simple enough to make it useful for controller design. Even after these simplifying assumptions, controller design remains a nontrivial problem, mainly for the following reasons:

- the models are typically of high order (more than 100 state variables);
- the model is multi-input–multi-output with a strong coupling between the channels;
- the controller should exhibit stability and performance robustness; indeed it is usually designed on the basis of a nominal plasma equilibrium configuration, but it is expected to perform well during an entire phase of a discharge when some plasma parameters change;
- the control variables are subject to physical limits due to the actuator constraints: voltage, current and power limits should therefore be taken into account in the design phase.

Along with the presentation of various controller schemes, both for plasma vertical stabilization, and for plasma shape, the book gives insight to the basic principles of nuclear fusion and tokamak operation, and a detailed derivation of the linearized model used for the design. In some cases, the controllers described have been implemented on existing tokamaks, and are now in operation. Some of these control schemes can be proposed for use with the experimental tokamak ITER.

The book is divided into two parts: Plasma Modelling and Plasma Control. Then it is organized into nine chapters plus two appendices.

1. *Introduction.* This chapter gives some basic notions about nuclear fusion and plasmas. Then a description of tokamaks and of the main magnetic control problems is given.
2. *Plasma Modelling for Magnetic Control.* In this chapter a description of the plasma model used for the controller design is given. The main simplifying assumptions are illustrated and the steps to derive the model are discussed. An overview of the mathematical tools used in this chapter can be found in the first of the two appendices.
3. *The Plasma Boundary and its Identification.* In this chapter the most common magnetic sensors used in magnetic control are described. Then

the plasma shape identification problem is discussed and an algorithm commonly used to solve this problem is presented.

4. *The Plasma Magnetic Control Problem.* In this chapter the problem of controlling the plasma current, position and shape is discussed. All aspects are covered: the choice of geometrical variables to control; the formulation of the control problem in terms of desired performance and plant limits; the presentation and comparison of the most commonly used control schemes.
5. *Plasma Position and Current Control at FTU.* This chapter describes the design of a current and position controller for the FTU/indexFTU tokamak, a tokamak in operation in Italy. This design is presented as a first example since in this case the problem is made much easier by the fact that the plasma is not vertically unstable.
6. *Plasma Vertical Stabilization.* This chapter focuses on the most basic control problem in a tokamak: the vertical stabilization problem. It is shown how it is possible to separate this problem from the problem of controlling the overall shape, and two solutions are presented.
7. *Plasma Shape Control for ITER.* In this chapter the plasma shape control for the ITER tokamak is discussed. A possible solution is presented; this solution exploits the fact that the vertical position control and the plasma current and shape control can be performed on different time scales.
8. *Plasma Shape Control at TCV.* This chapter presents the design of a high-order multivariable compensator for plasma current, position and shape control in TCV, a tokamak in operation in Switzerland. The problem is formulated in the  $H_\infty$  framework.
9. *Plasma Shape Control at JET.* This chapter describes the design of a new plasma shape controller implemented on the JET tokamak, the world's largest tokamak. From a control point of view, the design is a case of optimal output regulation for a non-right invertible plant, *i.e.* for a plant with fewer control inputs than controlled outputs.
10. *Appendices.* The appendices cover some mathematical notions that do not typically belong to the background of control engineers, along with a tutorial describing the various measurement units used in plasma physics.

This work would not have been possible without the help of many people. First of all we have to thank Professor Giuseppe Ambrosino, who initiated us into *automatic control* and introduced us to the problem of plasma control in tokamaks. Without his support and most of all his constant advice, we would never have gained the experience and the knowledge that led us to write this monograph. Thanks, Peppe!

Then we would like to thank Professor Raffaele Albanese, Professor Vincenzo Coccia, and all the CREATE team: we are really proud to be part of it.

Our sincere gratitude goes to all the people working at the sites where we gained our experience on operating tokamaks. In particular:

- Dr Flavio Crisanti of ENEA of Frascati and all the FTU team for the work done at FTU;
- Dr Jonathan Lister of the CRPP of Lausanne and the TCV team for the work done at TCV;
- Dr Filippo Sartori of UKAEA and the JET team for all the experiments we carried out at JET;
- Dr Alfredo Portone of EFDA, with whom we have been collaborating for more than 15 years on ITER magnetic control.

Finally, we really have to thank our families and loved ones for their support during this task: very often in recent months we have taken time away from them because of this book.

Napoli,  
March 2008

*Marco Ariola*  
*Alfredo Pironti*

---

# Contents

<b>1</b>	<b>Introduction</b>	1
1.1	Why Fusion?	1
1.2	What is Fusion?	2
1.3	What is a Plasma?	3
1.3.1	Fusion Energy Production and the Lawson Criterion	6
1.4	What is a Tokamak?	9
1.5	Feedback Control in Tokamaks	14
1.6	Electromagnetic Control	15
1.6.1	Modelling for Control	15
1.6.2	Plasma Boundary Estimation	16
1.6.3	Vertical Position Control	16
1.6.4	Plasma Radial Position and Current Control	18
1.6.5	Plasma Shape Control	19
1.6.6	Other Magnetic Control Problems	20

---

## Part I Plasma Modelling

---

<b>2</b>	<b>Plasma Modelling for Magnetic Control</b>	25
2.1	The Ideal Magnetohydrodynamics Theory	25
2.2	Magnetohydrodynamics in Axisymmetric Toroidal Geometry	26
2.3	A Plasmaless Model	30
2.4	The Plasma Equilibrium	35
2.5	A Linearized Model for Plasma Behaviour	40
<b>3</b>	<b>The Plasma Boundary and its Identification</b>	43
3.1	Plasma Boundary Definition	43
3.2	The Plasma Boundary Descriptors	46
3.3	Tokamak Magnetic Diagnostics for Plasma Shape Identification	50
3.4	Plasma Shape Identification	53
3.5	An Algorithm for Plasma Shape Identification	55

3.5.1	Choice of the Eigenfunctions for the Fourier Expansion .	56
3.5.2	Choice of the Singular Point for the Toroidal Harmonics	57
3.5.3	Numerical Results . . . . .	60
3.6	Taking into Account the Eddy Currents . . . . .	60

---

## Part II Plasma Control

---

<b>4</b>	<b>Plasma Magnetic Control Problem . . . . .</b>	<b>65</b>
4.1	Model for Controller Design . . . . .	66
4.1.1	Simulation Model . . . . .	68
4.2	Requirements for the Controller Design . . . . .	68
4.2.1	Gap Control Approach . . . . .	69
4.2.2	Typical Requirements and Constraints . . . . .	71
4.3	Plasma Vertical Stabilization Problem . . . . .	72
4.4	Control of the Currents in the Active Coils . . . . .	73
4.5	Possible Different Solutions . . . . .	75
<b>5</b>	<b>Plasma Position and Current Control at FTU . . . . .</b>	<b>79</b>
5.1	The FTU Simulation Model . . . . .	80
5.1.1	Plasma Model . . . . .	81
5.1.2	Plasma Shape Identification Block . . . . .	83
5.1.3	The Radial and Plasma Current Controllers . . . . .	84
5.1.4	The F and T Circuit Converter Models . . . . .	85
5.2	Choice of the Controller Gains . . . . .	86
<b>6</b>	<b>Plasma Vertical Stabilization . . . . .</b>	<b>89</b>
6.1	Vertical Stabilization Problem in the ITER Tokamak . . . . .	89
6.2	Vertical Stabilization Problem for the TCV Tokamak . . . . .	93
6.2.1	Design of the Vertical Position Controller . . . . .	96
<b>7</b>	<b>Plasma Shape Control for ITER . . . . .</b>	<b>99</b>
7.1	Singular Perturbation Decomposition for the ITER Tokamak . . . . .	100
7.1.1	Current and Shape Controller . . . . .	103
7.2	Simulation Results . . . . .	105
<b>8</b>	<b>Plasma Shape Control at TCV . . . . .</b>	<b>111</b>
8.1	Description of the TCV . . . . .	111
8.1.1	Magnetic Diagnostics . . . . .	112
8.1.2	Description of the Controlled Variables . . . . .	114
8.2	Design Specifications . . . . .	115
8.2.1	Controller Robustness . . . . .	115
8.2.2	Quantization Errors in the Measurements . . . . .	116
8.3	A Solution Based on the $H_\infty$ theory . . . . .	117
8.3.1	Choice of the Plant for the Design . . . . .	118
8.3.2	Description of the Weighting Functions . . . . .	118



8.3.3	Robust Stability .....	120
8.3.4	Current and Shape Controller Synthesis .....	121
8.4	Simulation Results .....	121
<b>9</b>	<b>Plasma Shape Control at JET .....</b>	<b>125</b>
9.1	Control Requirements and Simplified Plasma Modelling .....	125
9.2	The Controller Design .....	131
9.2.1	Requirements and Motivations .....	131
9.2.2	Optimal Output Regulation .....	132
9.2.3	Design of PI Controllers .....	137
9.3	Simulation Results .....	139
<b>A</b>	<b>Some Mathematical Background .....</b>	<b>143</b>
A.1	Green's Functions for the Homogeneous Grad-Shafranov Equation .....	143
A.2	Solutions of the Homogeneous Grad-Shafranov Equation .....	144
A.2.1	Green's Functions .....	145
A.2.2	Toroidal Harmonics .....	145
A.3	Ill-posedness and Plasma Shape Identification Problem .....	147
<b>B</b>	<b>Units Used in Plasma Physics .....</b>	<b>151</b>
	<b>References .....</b>	<b>153</b>
	<b>Index .....</b>	<b>159</b>

# Introduction

In this chapter we present the basics of nuclear fusion, plasmas, and of magnetic confinement of plasmas in toroidal machines called “tokamaks”. Feedback control plays an importance role in the operation of tokamaks: nowadays all tokamaks are equipped with feedback systems to control certain quantities during experiments. Some of these feedback systems are fundamental to the operation of tokamaks. Tutorial books on nuclear fusion and tokamaks include [1] and [2].

## 1.1 Why Fusion?

The energy demand by humanity is continuously rising. This is especially true because of the fast industrial development taking place in many “emerging countries”. As shown in Figure 1.1, about 80% of the energy used on earth comes from fossil fuels: oil, gas and coal. Fossil fuels are a limited resource. It has been estimated that in 150 years about one half of the available resources will have been exploited. At the present rate of annual increase of energy use, experts predict that in about 30 years oil extraction will become inconvenient, whereas there should be about two centuries left for coal, and natural gas should last 45–60 more years [3].

Besides being limited resources, fossil fuels pose serious problems of pollution: burning these fuels for energy production is the largest source of emissions of carbon dioxide, which is one of the greenhouse gases that contributes to global warming. Therefore the need for new sources of energy to take the place of fossil fuels will become a critical problem in the near future. Many alternative energy sources such as wind, water, solar, geothermal, biofuel seem to be attractive from an ecological viewpoint but there is serious scepticism concerning the possibility of them replacing diminishing supplies of fossil fuels in an increasingly urbanized world because of the limited energy density (*e.g.*, megajoules per square kilometre) provided by these sources. It is estimated that all these alternative energy sources together will provide no more than

25% of the energy needed in 2050 for an estimated world population of 10 billion people. For these reasons, alternative sources of energy need to be found: one of the best candidates is nuclear fusion.

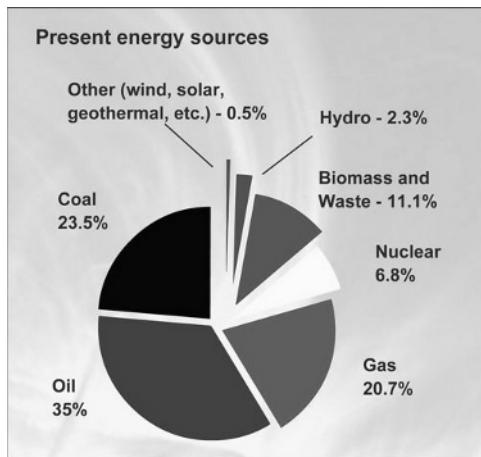


**Figure 1.1.** Energy sources. Most of the energy currently supplied to humanity comes from fossil fuels. Alternative sources provide about 20% of the energy used on earth. (Image Source: European Fusion Development Agreement (EFDA) website: <http://www.efda.org/>. Used with permission.)

## 1.2 What is Fusion?

Nuclear fusion is a promising source of energy to support the increasing world demand. Fusion reactions power the sun and other stars. In fusion reactions, low-mass nuclei combine, or fuse, to form more massive nuclei. In the sun, a sequence of fusion reactions, named the p-p chain, begins with protons, the nuclei of ordinary hydrogen, and ends with alpha particles, the nuclei of helium atoms. After a fusion reaction, the total masses are less than before: the “missing” mass is converted into energy, as quantified by the well known Einstein equation

$$E = (m_r - m_p)c^2 \quad (1.1)$$

where  $E$  is the energy resulting from the reaction,  $m_r$  is the mass of the nuclei before the reaction,  $m_p$  is the mass of the nuclei after the reaction, and  $c$  is the speed of light.

Nuclear fission also relies upon the same principle: in a fission reaction, a heavier nucleus divides into smaller nuclei. The principles of nuclear fission have been exploited in current nuclear power reactors that operate in many

countries in the world. Although nuclear fission does not cause any air pollution or greenhouse gas production, its production poses many problems: there are risks of serious accidents; there is significant production of radioactive waste, which needs appropriate treatment; and moreover, fission technology can be used for the production of nuclear weapons. On the other hand, the fusion process is inherently safe, although the fusion reaction also produces radioactive waste. However, management of this waste poses much less of a problem than in the fission case: byproducts of fusion reactions are tritium, a radioisotope of hydrogen, and neutrons; the flux of neutrons in a reactor will make the structural materials radioactive (will “activate” the materials). Tritium has a short half-life of 12 years, whereas appropriate choice of materials could result in waste that have half-lives of tens of years rather than thousands of years, as for fission. Another great advantage of fusion over fission is that the fuel sources can easily and cheaply be extracted from sea water, and therefore, in principle, these sources are essentially inexhaustible. Finally, major accidents are impossible since fusion must be continuously fuelled, so it is easily stopped. Furthermore, the large volume of hot gas at the heart of a fusion reactor will only be at around atmospheric pressure, and will not have enough stored energy to cause dangerous accidents. Regarding the radioactive tritium, very little will be used (fractions of a gram in the active part of the system, with more in secure storage): it will be easy to design a reactor so that even in the worst imaginable accidents or incidents (such as earthquakes or aircraft crashes) only a small percentage of the tritium inventory could be released and evacuation of the neighbouring population would not be necessary.

### 1.3 What is a Plasma?

Since nuclei carry positive charges, they normally repel one another. To overcome the Coulomb barrier, the kinetic energy of the nuclei is increased by heating. The higher the temperature, the faster the atoms or nuclei move. The fuel must be heated to temperatures around 100 million degrees, at which the nuclei overcome the force of repulsion of the positive charges when they collide, and fuse. At much lower temperatures (about 10 thousand degrees), the electrons and nuclei separate and create an ionized gas called plasma.

Plasmas are also known as the fourth state of matter. The other three states are solids, liquids, and gases. Each atom in a solid, liquid or gas is electrically neutral, with a positively charged nucleus surrounded by negatively charged electrons. In a plasma, the electrons are stripped from the nuclei of the atoms resulting in an ionized gas where positively and negatively charged particles move independently. Hence, since the particles in a plasma are charged, they conduct electricity and interact with magnetic fields.

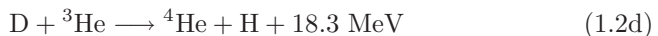
The difficulty in producing fusion energy is the development of a device that can heat the fuel to a sufficiently high temperature and then confine it for

a long enough time so that more energy is released through fusion reactions than is used for heating. There are three known ways to accomplish this:

- a) by gravitational confinement. This is how fusion occurs in the stars. In this case the plasma is compressed to a high density and temperature by a gravitational field. This field also balances the thermal expansion forces. This confinement method needs a large amount of mass that can only be found in stars;
- b) by inertial confinement. In this case a large amount of energy is transferred to the particles in such a way as to determine values of density and temperature giving a favorable fusion reaction rate. If these values of density and temperature are maintained for a sufficient time, a net amount of energy can be produced;
- c) by magnetic confinement. In this case the physical principle used is the interaction between the charged particles of the plasma and a magnetic field produced by external sources. As will be discussed later in this book, this interaction enables a plasma to be confined in a well-defined limited region.

The most promising of these approaches is the magnetic confinement [4], which is the one used in tokamak machines.

To make fusion happen, it is necessary to bring two nuclei close enough to overcome the mutual repulsion due to their positive charges. The principal nuclear reactions are those involving light nuclei, such as the hydrogen isotopes deuterium D and tritium T. The symbol for deuterium is  $^2\text{H}$ , whereas the symbol for tritium is  $^3\text{H}$ , where the superscript on the left of the element indicates the mass number, *i.e.*, the total number of protons and neutrons. The possible reactions involving deuterium and tritium are



In Equations 1.2 He is the symbol for helium, and  $n$  indicates a neutron. As a result of the fusion, the products of the reactions carry energy, which is measured in MeV (millions of electronvolts, see Appendix B for a tutorial on the most common units used in plasma physics).

To induce fusion of the nuclei, it is necessary to overcome the repulsion due to their positive charges. The collision or interaction of two particles is generally described in terms of the reaction “cross-section”, typically indicated by  $\sigma$ . This quantity essentially gives a measure of the probability for a reaction to occur: the higher the cross-section, the higher the probability that the fusion reaction occurs. The cross-section of the interaction may be calculated if the form of the basic interaction between the particles is known. The cross-section is a function of the particles impact energies: at low energies, the

cross-section is small because of the Coulomb barrier, which prevents the nuclei from approaching to within nuclear dimensions, as is required for fusion to take place; then the cross-section increases with energy.

The two reactions (1.2b) and (1.2c) occur with about equal probability. The energy is released in the form of kinetic energy of the reaction products, *e.g.*, for reaction (1.2a) the helium atom carries 3.5 MeV and the neutron carries 14.1 MeV.

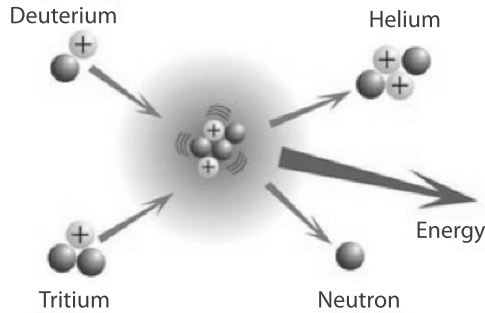


**Figure 1.2.** The D–T fusion reaction (1.2a). A deuterium nucleus (one proton and one neutron) and a tritium nucleus (one proton and two neutrons), two isotopes of hydrogen, are fused to form a helium nucleus (two protons and two neutrons) and a free energetic neutron. As a result of the reaction energy is released. (Image source: ITER website <http://www.iter.org/>. Used with permission.)

By far the most promising fusion reaction is (1.2a) (see Figure 1.2). The reason is that its cross-section is considerably less than that for the other reactions (1.2b)–(1.2d) except at impractically high energies. For this reason the first generation of fusion power systems will be based on the deuterium–tritium (D–T) reaction (1.2a). The major fuel, deuterium, may be readily extracted from ordinary water, which is available to all nations. The concentration of deuterium in water is 1 atom out of 6,500 atoms of hydrogen. Nuclear fusion has enormous potential: from 100 mg of deuterium (contained in about 3 l of sea water) plus 150 mg of tritium, it is possible to obtain the same energy produced by about 1,100 l of oil (approximately 7 barrels of oil).

Reaction (1.2a) needs tritium; tritium undergoes radioactive decay with a half-life of 12.3 years and therefore does not occur naturally, but would be produced from lithium by the reaction



using neutrons from the reaction (1.2a) itself. Fortunately  ${}^6\text{Li}$  is an abundant isotope, comprising 7.5% of natural lithium, which is copiously present in the earth's crust.

The world-wide availability of these materials would thus eliminate international tensions caused by imbalances in fuel supply. In the fusion reaction, very small quantities of matter are converted into huge amounts of energy, according to Einstein's formula (1.1). The fraction of mass "lost" and converted into energy is just about 38 parts out of 10,000.

The D-T reaction requires the smallest input energy ( $\sim 10$  keV) or lowest temperature ( $\sim 10^8$  degrees), and yields almost the largest output energy (17.6 MeV). The energy gain for this type of reaction is around 2,000. The D-T fusion reaction produces neutrons which escape from the magnetic field due to their lack of charge and carry 80% (14.1 MeV) of the fusion energy to a specially designed wall, called the blanket. The energy in the neutron is what is captured to produce electrical power. In a working power plant, the blanket would capture the neutrons, convert their kinetic energy into heat which drives the electrical generators, and breed the tritium fuel. The other 20% (3.5 MeV) of the fusion energy is released in helium ions or "alpha particles", which are contained by the magnetic field and which self-heat the plasma.

### 1.3.1 Fusion Energy Production and the Lawson Criterion

The aim of a fusion reactor device is net energy production; in other words a useful reactor must produce more power from the reaction than the power required for heating the plasma and operating the machine. In this section we present some conditions that must be met to achieve this goal.

Let us focus on the D-T reaction (1.2a). The thermal energy density (*i.e.*, the energy per unit volume)  $W$  in the plasma is given by

$$W = \frac{3}{2}(n_D + n_T + n_e)T,$$

where  $n_D$  is the deuterium ion density (ions per unit volume),  $n_T$  is the tritium ion density,  $n_e$  is the electron density, and  $T$  is the temperature expressed in eV. Throughout this section the temperature will always be expressed in eV.

Assuming a fuel for the reaction consisting of deuterium and tritium in the same quantities, and taking into account that there is an electron for each tritium or deuterium ion, then

$$n_D = n_T = \frac{n_e}{2}.$$

Letting  $n = n_e$ , it is then possible to write

$$W = 3nT. \tag{1.4}$$

A simple energy balance in the plasma can be written as

$$\dot{W} = P'_{fus} + P_{ext} - P_{loss}, \tag{1.5}$$

where  $P'_{fus}$  is the power density produced by the nuclear fusion reactions remaining inside the plasma, which contributes to the plasma thermal energy,  $P_{ext}$  is the power density produced by external additional heating devices, and finally  $P_{loss}$  is a term which represents all the power losses.

There are two main causes of losses in a plasma: the first is due to the fact that plasma confinement cannot be perfect, and therefore particles and heat diffuse from the plasma centre towards the outside; the second is due to the *bremsstrahlung*; this term indicates the radiation produced when electrons in the plasma hit other charged particles, such as electrons or ions, at a cooler temperature and suddenly decelerate. The power density lost by bremsstrahlung is given by [5]

$$P_{br} = 1.69 \times 10^{-38} n^2 Z_i^2 T^{1/2}. \quad (1.6)$$

In Equation 1.6,  $Z_i$  indicates the ion charge (for D–T mix it is equal to 1).

The power density produced by nuclear fusion is a function of the particle density and of the thermal energy itself. Indeed, high thermal energy allows the plasma nuclei to overcome the Coulomb repulsion force more easily, while the density determines the probability for two nuclei to interact. The reaction rate is given by

$$R_{DT} = n_D n_T \langle \sigma v \rangle = \frac{1}{4} n^2 \langle \sigma v \rangle, \quad (1.7)$$

where  $\langle \sigma v \rangle$  is the product between the cross-section  $\sigma$  of the reaction and the relative velocity  $v$  of the nuclei, averaged over a Maxwellian distribution. The reactivity  $\langle \sigma v \rangle$  depends on the plasma temperature; Figure 1.3 shows this dependence for the D–T reaction.

In order to calculate the fusion density power  $P_{fus}$  we need to multiply the reaction rate given by Equation 1.7 by the energy  $E$  given by the reaction (1.2a), which is equal to 17.6 MeV; in this way we obtain

$$P_{fus} = R_{DT} E = \frac{1}{4} n^2 \langle \sigma v \rangle E. \quad (1.8)$$

The part of this power density which remains inside the plasma can be evaluated as

$$P'_{fus} = R_{DT} E' = \frac{1}{4} n^2 \langle \sigma v \rangle E', \quad (1.9)$$

where  $E' = 3.5$  MeV is the energy carried by the helium ion after the fusion reaction (1.2a); the remaining part of the power density (1.8) is associated with the neutron particles that leave the plasma core to reach the blanket.

Coming back to Equation 1.5, if the source term  $P'_{fus} + P_{ext}$  is larger than the loss term  $P_{loss}$ , then the plasma gains energy, otherwise the plasma loses energy. In the stationary case the source term compensate for the losses, and the thermal energy of the plasma remains constant. In this conditions it is useful to define the *energy confinement time*  $\tau_E$ , and the *amplification factor*  $Q$ . The energy confinement time is defined as



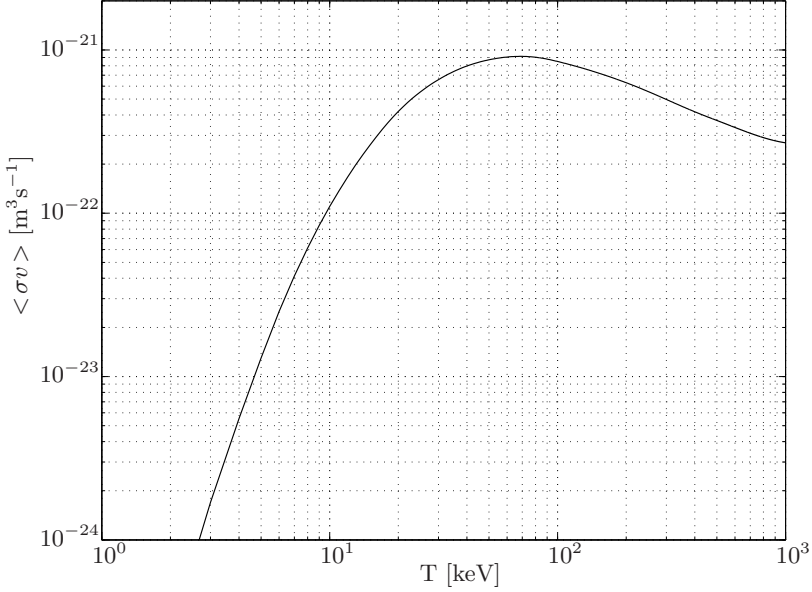


**Figure 1.3.** The reactivity  $\langle \sigma v \rangle$  as a function of the plasma temperature for the D-T reaction. The data are from [6]

$$\tau_E = \frac{W}{P_{loss}}. \quad (1.10)$$

The time  $\tau_E$  is the characteristic time of decrease of the plasma thermal energy; it is linked to the time necessary to completely dissipate the plasma energy if the sources supplying it are cut off.

The amplification factor is the ratio between the power produced by the fusion reactions and the power supplied by the external heating devices

$$Q = \frac{P_{fus}}{P_{ext}}. \quad (1.11)$$

If  $Q = 1$  then the power produced by the nuclear fusion is equal to the power provided by the external heating devices. This is the so called *break-even* condition. In this condition the heating of the plasma is, to a great extent, done by the helium ions, and not only by the additional heating. Note that this is not a situation which allows production of energy. If  $Q = \infty$  the *ignition* condition is reached. In this case  $P_{ext} = 0$  and the thermal energy of the plasma is completely sustained by the nuclear fusion reactions. A nuclear fusion reactor will have to operate with an amplification factor  $Q$  significantly larger than 1. The break-even condition has been reached in D-T experiments in the tokamaks JET [7] and JT-60, in particular, in JT-60 the world record value of  $Q = 1.25$  has been obtained transiently [8].

Conditions at break-even or ignition are usually expressed in terms of the so-called *Lawson's criterion*, which originally appeared in [9]. Assuming a stationary condition, that is  $\dot{W} = 0$ , the balance energy Equation 1.5 becomes

$$P_{fus} \left( \frac{E'}{E} + \frac{1}{Q} \right) = \frac{W}{\tau_E}, \quad (1.12)$$

where the following relationships have been used

$$\begin{aligned} P'_{fus} &= \frac{E'}{E} P_{fus} \\ P_{ext} &= \frac{P_{fus}}{Q} \\ P_{loss} &= \frac{W}{\tau_E}. \end{aligned}$$

Using (1.4) and (1.8), Equation 1.12 can be written as

$$n\tau_E = \frac{12}{E \left( \frac{E'}{E} + \frac{1}{Q} \right)} \frac{T}{\langle \sigma v \rangle}. \quad (1.13)$$

Equation 1.13 expresses Lawson's criterion; for example, Lawson's criterion for ignition in the D-T fusion reaction under consideration is

$$n\tau_E = \frac{12}{E'} \frac{T}{\langle \sigma v \rangle}. \quad (1.14)$$

For  $T = 25$  keV (which is a temperature close to the minimum of  $T/\langle \sigma v \rangle$ ), we obtain

$$n\tau_E \simeq 1.7 \times 10^{20} \text{ m}^{-3} \text{ s}.$$

Once the plasma temperature has been chosen, Lawson's criterion determines conditions on the density and the energy confinement time that have to be met. A difference between inertial and magnetic confinement methods is in the fact that in inertial confinement devices the energy confinement time is very small (between 10 and 100 ps) and the density is extremely large (in the order of  $10^{31} \text{ m}^{-3}$ , three orders of magnitude larger than the density of solid state hydrogen); on the contrary, in magnetic confinement devices, densities are smaller (in the order of  $10^{20} \text{ m}^{-3}$ , much lower than air density), so the energy confinement time has to be larger (in the order of 1 s).

## 1.4 What is a Tokamak?

The tokamak [2] concept invented in the Soviet Union in the late 1950s is now the major and most promising magnetic confinement approach being pursued

around the world. Tokamak is an acronym developed from the Russian words TOroidalnaya KAmera ee MAgnitaya Katushka which means “toroidal chamber with magnetic coils”. As the name suggests, it is a magnetic confinement device with toroidal geometry.

The largest tokamak in the world is the Joint European Torus (JET) in Culham, England (Chapter 9). The DIII-D tokamak, is one of roughly a dozen medium-sized tokamaks around the world; other tokamak, which will be presented in the following chapters, are FTU in Italy (Chapter 5) and TCV, in Switzerland (Chapter 8).

Tokamaks are nowadays the most promising devices for the development of nuclear fusion power plants. These devices could be one of the best approaches to energy generation in the long term and therefore are the subject of intensive international programmes of research, one of the most important being the ITER project (Chapter 7).

Figure 1.4 shows a drawing of the ITER tokamak with

- the vacuum vessel, the chamber where the plasma is contained;
- the blanket, which has the main roles of absorbing the 14 MeV neutrons (see Equation 1.2a) and of breeding the plasma with tritium, which is needed for the reaction (1.2a). For this reason, the blanket is usually composed of lithium so that reaction (1.3) can occur;
- the toroidal coils. The currents flowing in these coils generate a poloidal field (poloidal field coils, or PF coils). The coils in the centre of the machine (Figure 1.5) are called central solenoids (CS); the plasma current is built up by transformer action, where the central solenoids are the transformer primary and the plasma itself acts as the transformer secondary;
- the poloidal coils. The currents flowing in these coils generate a toroidal field (toroidal field coils, or TF coils).

In the presence of a prescribed magnetic field, a charged particle will describe a simple cyclotron gyration around the magnetic field line. The dynamics of the charged particle is determined by the Lorentz force,

$$m \frac{d}{dt} \mathbf{v} = q(\mathbf{v} \times \mathbf{B}), \quad (1.15)$$

where  $m$  and  $q$  are the mass and charge of the particle, respectively,  $\mathbf{v}$  is the particle velocity, and  $\mathbf{B}$  is the magnetic field. When the component of the velocity parallel to the magnetic field, which is not affected by the Lorentz force, is different from zero, the trajectory of the charged particle is a helix. In this case the particle would fall out from the ends of the magnetic field line, contrary to our desire to keep them confined. To solve this, the tokamak uses field lines bent into a torus so that there is no end. In a tokamak, the toroidal magnetic field is produced by the TF coils. The addition of a poloidal field generated by the toroidal plasma current, which is necessary for magnetohydrodynamic (MHD) equilibrium [10] (Chapter 2), produces a combined field

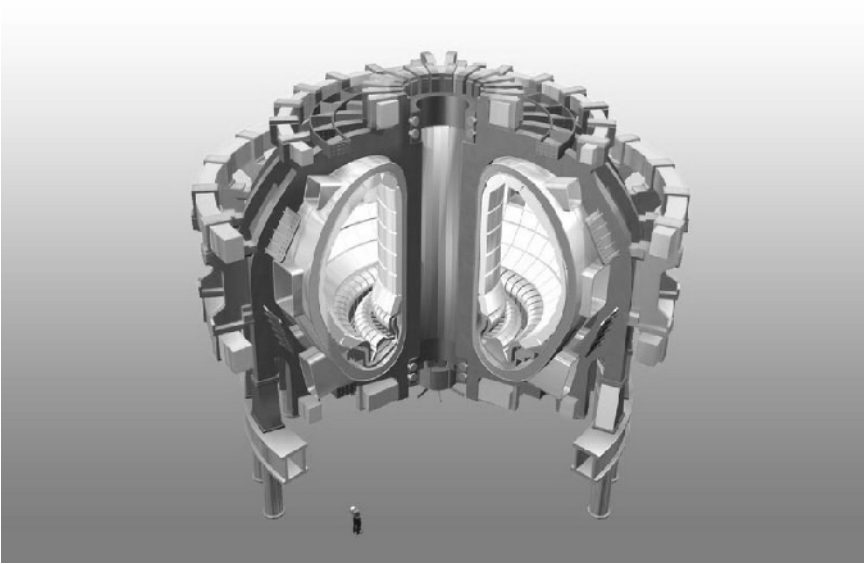


**Figure 1.4.** Tokamak view. Toroidal and poloidal field coils, vacuum vessel and blanket. (Image source: picture by Eric Verdult of Kennis in Beeld/New Media Design: <http://www.kennisinbeeld.nl/>. Used with permission.)

in which the magnetic field lines twist their way around the tokamak to form a helical structure (Figure 1.5).

Tokamak reactors are pulsed machines (Figure 1.6); in each pulse the plasma is created (“start-up” phase), then its current is ramped up to a reference constant value, called the “flat-top” current, which is maintained in a burning state along the main phase of the discharge, and eventually the current is ramped down and the plasma is terminated. The time trajectories of the PF and TF coil currents and of the main plasma parameters that guarantee this sequence define a “scenario”.

To initiate the discharge, hydrogen gas is puffed into the tokamak vacuum vessel and the toroidal field coil current is increased to create a steady-state magnetic field to contain the plasma when initially created. Then a large electric field is produced within the torus using the CS (ohmic heating) coils. This electric field rips apart the neutral gas atoms and produces the plasma. The plasma current in the plasma is built up by transformer action. The collisions of the ions in the plasma make the plasma resistive. It is this resistance that heats up the plasma (thus the origin of the term “ohmic heating”). When the temperature increases, the resistance decreases and the ohmic heating loses effectiveness. To significantly increase fusion reactions, the temperature must

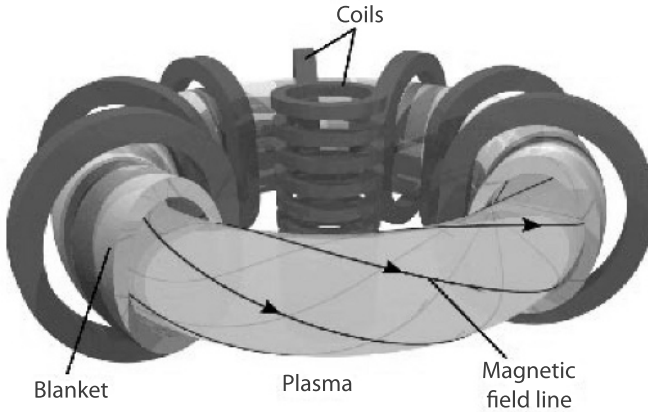


**Figure 1.5.** The principle of a tokamak. The plasma is contained in a doughnut-shaped vessel. Using external coils a magnetic field is generated, which causes the plasma particles to run around in circles, without touching the vessel wall. (Image Source: European Fusion Development Agreement (EFDA) website: <http://www.efda.org/>. Used with permission.)

be increased to over 100 million degrees, which is six times the temperature at the centre of the sun. This heating is accomplished by particle beams (injecting energetic ions) or by radio frequency or microwaves (heating ions or electrons). Shortly after the discharge starts, additional gas is puffed into the chamber to increase the density and/or pressure to the desired levels.

The plasma magnetic control action varies the current in the PF coils; these currents generate magnetic fields which interact with the plasma, modifying its current (plasma current control), position, and shape (plasma shape control). The PF coil currents are then decomposed into the sum of two terms: a preprogrammed nominal (feedforward) part, that is decided before the discharge in order to have the desired plasma parameters along the prescribed trajectories corresponding to given scenarios, plus a component used for feedback control, that is needed to counteract the effect of disturbances, model inaccuracies, *etc.*

As a matter of fact, in the control of plasma position, current and shape, the use of feedback control is mandatory, not just a choice. Indeed, in order to maximize performance-to-cost ratio, it is necessary to use plasmas with vertically elongated (*i.e.*, egg-shaped) cross-sections; unfortunately this elongation, leads to instability of the plasma vertical movements [11]. As a consequence, at least for vertical position stabilization, feedback control needs to be adopted for vertically elongated plasmas. In addition, a strong motivation for improving plasma control in next generation tokamaks is that the plasma boundary must be maintained as close as possible to nearby components. This objective guarantees the best use of the available volume, and helps to induce mirror

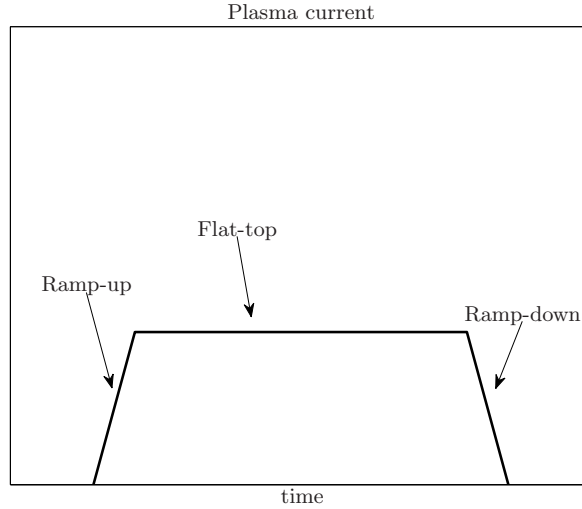


**Figure 1.6.** A typical reference for the plasma current during a discharge. After plasma initiation (break-down phase), the plasma current is ramped up (during the ramp-up or start-up phase) till its final target value, which is then kept constant during the flat-top phase. Finally with the current ramp-down, the plasma is cooled down and extinguished.

currents in the neighbouring metallic structures; these currents, called *eddy* or *passive* currents, generate a magnetic field that opposes plasma movement and therefore ensures a sort of passive stabilization. Hence the ability to control the shape of the plasma, while ensuring good clearance, is an essential feature of plasma control systems.

In the JET tokamak the toroidal component of the magnetic field, used to confine the plasma within the torus, is generated by large D-shaped coils (toroidal field coils) with copper windings, which are equally spaced around the machine. The primary winding (inner poloidal field coils) of the transformer, used to induce the plasma current which generates the poloidal component of the field and heats the plasma, is situated at the centre of the machine. Coupling between the primary winding and the toroidal plasma, acting as the single turn secondary, is enhanced by the massive eight-limbed transformer core. Around the outside of the machine, but within the confines of the transformer limbs, is the set of field coils (outer poloidal field coils) used for positioning, shaping and stabilizing the position of the plasma inside the vessel. The plasma inside the torus essentially constitutes a big fat wire, since it is made up of charged particles in motion, *i.e.*, it has a current. The large current-carrying coils on the outside of the torus push or pull against the plasma based on a version of the basic principle of forces between parallel conductors: if the currents are in the same direction, the magnetic fields exert

a force to push the wires together; if the currents are in opposite directions, the force exerted tends to push them apart. For this reason the structure of the tokamak must be built in such a way as to be able to withstand this mechanical stress.

## 1.5 Feedback Control in Tokamaks

Experimental fusion technology has now reached a point where experimental devices are able to produce about as much energy as is expended in heating the plasma, and a long range plan for the development of fusion energy has been proposed. The immediate next step in this roadmap is the construction and operation of the International Thermonuclear Experimental Reactor (ITER). The ITER tokamak, an international 10 billion euros project that includes the European Union, the People's Republic of China, the Republic of Korea, the Russian Federation, Japan, India and the United States, will demonstrate the physics understanding and several key technologies necessary to maintain burning plasmas.

The planned ITER device will be capable of exploring advanced tokamak (AT) modes of operation, characterized by high plasma pressure, long confinement times, and low levels of inductively driven plasma current, which allows steady-state operation. These advanced modes rely heavily on active control to develop and maintain high performance plasmas with sufficient plasma density, temperature, and confinement to maintain a self-sustaining fusion reaction for long durations.

Tokamaks are high order, distributed parameter, nonlinear systems with a large number of instabilities, so there are many extremely challenging mathematical modelling and control problems, that need to be solved; this is especially true for a fusion power reactor.

The tokamak control problems can be separated into two major classes: electromagnetic control and plasma kinetic control. Electromagnetic control refers to controlling the magnetic and electric fields, which maintain or change the plasma position, shape and current. As was previously explained, this task is performed by the poloidal coils distributed around the vessel that contains the plasma. Voltages are applied to these coils, which drive currents that generate the magnetic fields. The magnetic fields, regulated by feedback control, induce plasma current, change the plasma shape, and stabilize the intrinsically unstable plasma vertical position. AT plasma regimes require production and regulation of extreme plasma shapes that allow operation at high plasma pressure.

Plasma kinetic control refers to controlling particle feed rates and heating to modify the plasma density, temperature, pressure, and current density. Due to the distributed parameter nature of tokamaks, it is important to control not only spatially averaged values of these physical variables but also their spatial profiles. Energy confinement, stability properties, and the fraction of

noninductive current, which is fundamental for steady-state operation, can be improved through control of internal pressure and current profiles.

In addition, electromagnetic and kinetic control, including internal profile control, must be well coordinated with control action to avoid or stabilize MHD instabilities. Optimization of the plasma shape and internal profiles can reduce the strength of these instabilities, or in some cases prevent them.

In the following sections, we will present and discuss the various control problems that need to be tackled in tokamaks. For each of them, besides presenting the main issues, we will give a historical perspective, describing the way the problem has been solved over the years.

## 1.6 Electromagnetic Control

### 1.6.1 Modelling for Control

The interaction between the plasma and the external circuits can be described by a set of nonlinear partial differential equations (PDEs), whereas the controller design techniques are based upon the availability of ordinary differential equation (ODE) models, usually linear, time invariant, and of low order. The main problem is then that of introducing physical simplifying assumptions and using approximate numerical methods so as to obtain a model detailed enough to catch the principal phenomena, but reasonably simple enough to make the controller design possible. The approximations that can be made strongly depend on the plasma geometrical parameters to be controlled. A thorough presentation of the models for magnetic control, and their assumptions, can be found in Chapter 2.

The main simplifying assumptions that will be made to derive a model of the interaction between the plasma and the surrounding structures are the following.

- The first assumption is that the plasma behaviour can be described by means of a finite number of global parameters.
- The second assumption concerns the symmetry of the problem: the plasma behaviour is supposed to be axisymmetric, namely, independent of the toroidal angle. As a consequence of this assumption, our problem is reduced to a two-dimensional one.
- The third assumption is that plasma mass may be neglected.
- The fourth assumption is that the plasma can be considered as an ohmic deformable conductor. It is therefore supposed that its resistivity is somehow known. This is not rigorously correct since the plasma resistivity actually depends on the plasma temperature (the higher the temperature, the lower the resistivity); however this effect is neglected since uncertainties in resistance models are usually very high.



In Chapters 2 and 3 it is shown how, starting from the physical laws, it is possible to derive an approximated finite-dimensional-linear-time-invariant (FDLTI) model that can be used for the design of plasma current, position and shape control.

### 1.6.2 Plasma Boundary Estimation

The magnetic lines that guide the particles around the major axis of the torus are helices, *i.e.* a combination of toroidal and poloidal magnetic fields. It is possible to use the poloidal component of these magnetic lines to define nested toroidal surfaces corresponding to constant values of the poloidal flux function  $\psi$  (see Equation 2.6 for its definition).

The plasma boundary is defined as the outermost closed flux surface contained inside the device. It is the shape of this boundary that is generally referred to as plasma shape. Unfortunately, the plasma shape cannot be directly measured, and for control purposes must be estimated in real time using indirect measurements of magnetic flux and field. One of the available methods for plasma boundary estimation is based on equilibrium reconstruction. Equilibrium codes, such as EFIT [12], calculate the distributions of flux and toroidal current density over the plasma and surrounding vacuum region that best fit, in a least square sense, the external magnetic measurements, and that simultaneously satisfy the MHD equilibrium equation (Grad–Shafranov equation). Once the flux distribution is known, it is possible to reconstruct the plasma boundary. Alternatively, the boundary is sometimes calculated making use of reconstruction codes, such as XLOC [13], that are limited to locating the boundary and are not aimed at evaluating parameters describing the plasma internal features.

The problem of reconstructing the plasma shape from the available measurements is the topic of Chapter 3. In the context of plasma control, this problem is usually referred to as “plasma shape identification”.

### 1.6.3 Vertical Position Control

Tokamaks constructed in the 1970s had a circular, vertically stable plasma poloidal section, so that there were no serious vertical position control problems. Since then, however, it has become clear that improved plasma parameters, specifically an increased energy confinement time can be obtained using a vertically elongated cross-section. The first experiments performed on tokamaks such as TOSCA [14] confirmed these theoretical predictions. Unfortunately, vertically elongated plasmas are vertically unstable; theoretically, these instabilities can be stabilized by surrounding the plasma with a superconductive wall [15]. Standard conductive walls with positive electrical resistance can only slow down the unstable mode; to stabilize the plasma an active feedback system is required [16].

The plasma circuit model or simply circuit model, used for modelling the plasma–vessel–coils system, combines physical simplicity with the potential for a high degree of accuracy in the external conductor and coils model. The plasma is modelled as a rigid wire loop free to move vertically. Neglecting the plasma mass the plasma vertical motions are described by a lumped parameter model. A circuit model is used in [17] to analyse a feedback system consisting of a single passive coil and an active feedback coil. It is proved that proportional feedback of the plasma vertical position can stabilize the system, provided that the shielding effect of the passive coil, measured by the mutual inductance, is sufficiently small. However, this result is not quantitatively extendable to a massive structure of passive conductors.

The circuit model has also been used to design sophisticated controllers for plasma vertical stabilization. In [18] a modified linear-quadratic (LQ) approach, which accounts for the time delay of the power supply, enlarges the stability region with respect to the standard PD controllers. In [19] an  $H_\infty$  approach is used to design a vertical controller with low sensitivity to changes in the operating point. A low-order controller is also designed in [19] using a reduced-order plant model obtained from balanced truncation. In [20], a predictive control algorithm is implemented on the COMPASS-D tokamak. This algorithm stabilizes the plasma using only flux sensors external to the vacuum vessel, as opposed to a standard PD controller, which uses mode estimates based at least partially on magnetic field sensors internal to the vacuum system. In [21] a derivative controller is used to stabilize the plasma vertical velocity. The derivative gain is adaptively changed with the growth time of the unstable mode: the variations of the growth time are detected by measuring the frequency of the plasma vertical oscillations around the equilibrium due to a deadzone in the power supply.

The weakness of the single filament circuit model with a rigidly moving plasma is that this approach does not account for plasma shape deformations, which involve modified force equilibria. In particular, this model accounts for only the equilibrium field gradient at the chosen nominal location for the plasma filament. In [22] and [23] the plasma is represented as an array of fixed current-carrying filaments.

The multifilament model, however, does not eliminate the main problem of the circuit approach, namely, that the plasma is modelled as a rigid body with a single degree of freedom (vertical displacement). In fact, the multifilament model can impose only one global constraint, namely total vertical force balance, and does not guarantee local equilibrium of the forces. In [24] a linearized, non-rigid model of the plasma vertical displacements is presented. The resulting numerical model, which is more accurate than the multifilament models, can be used for open-loop analysis and for designing stabilizing controllers. Furthermore, this model addresses the problem of optimal sensor location for designing active stabilization systems for highly elongated plasmas [25]. A modification of the linearization procedure illustrated in [24] is proposed in [26] to include the effect of the vessel on plasma stability. This

model is obtained by approximating the plasma response to currents in the vacuum vessel in terms of equivalent poloidal field coil currents. The linearized perturbed equilibrium plasma response model is used for designing a vertical stabilization controller based on full-state-feedback pole placement combined with an observer that uses flux and field measurements and their calculated time derivatives.

Model-based control design approaches have been used recently to control the plasma vertical position in [27], where the authors use the  $H_\infty$  technique; in [28], where a nonlinear, adaptive controller is designed; in [29], where an anti-windup synthesis is proposed to allow operation of the vertical controller in the presence of saturation; and in [30], where a fuzzy-logic-based controller is designed and implemented to control the position of the plasma column throughout an entire discharge.

In [31] the authors exploit a full multivariable model of the vertical instability using a matrix pencil analysis to provide for a rigorous demonstration of necessary conditions for stabilization of the plasma by PD feedback of vertical displacement.

Vertical stabilization is discussed in Chapter 6, where we illustrate the way vertical stabilization has been tackled for ITER and TCV tokamaks.

#### 1.6.4 Plasma Radial Position and Current Control

To simplify plasma motion control, early tokamaks used sets of poloidal field coils symmetrically placed with respect to the tokamak equatorial plane to guarantee mutually independent vertical and horizontal movement of the plasma. The problem is then separated into two orthogonal parts:

- horizontal position and current control by means of up-down symmetric currents;
- vertical position control by means of up-down anti-symmetric currents.

Initially, research efforts concentrated on the radial position control of circular, vertically stable tokamak plasmas.

Coupling between the plasma radial position and current control systems depends on the active poloidal coil system. In traditional tokamak designs, a decoupled system of poloidal windings is used. This system consists of an ohmic heating (OH) winding, the central solenoid, that controls the ohmic magnetic flux and thus the plasma current, as well as a vertical field (VF) circuit that controls the plasma major radius. For these tokamaks, the simplest controller structure consists of two separate SISO controllers. For more complex systems, or when high performance is required, MIMO decoupling controllers are needed. In [32] an LQ optimal controller for plasma radial position and current in the Tokamak Fusion Test Reactor of the Princeton Plasma Physics Laboratory during the flat-top phase is proposed. This controller computes the voltages of the OH and VF coils as a linear combination of eight measurements, namely, plasma radius and current, active coil currents, and

their derivatives. In [33] this approach is extended to include the start-up phase in which the plasma shape expands and the plasma current increases so that the resulting model is time varying. Finally, control of the plasma major radius and current in the ISX-B tokamak with a  $2 \times 2$  generalized PD controller is investigated in [22].

An example of plasma current and radial position control is presented in Chapter 5 for the FTU tokamak. In this case, the plasma cross-section is not elongated and therefore the vertical stabilization loop is not needed. The problem is solved by means of two SISO PID controllers. More typically, when plasma performance is demanding, the plasma radial position control is seen as part of the more general and challenging *plasma shape control*. Therefore on most of the operating tokamaks, plasma radial control and plasma shape control are integrated, whereas the current control is typically treated separately, since the plasma current response is slower than the time response required of the shape controller.

### 1.6.5 Plasma Shape Control

Besides the mandatory feedback control of the vertical position, to use in the best possible way the available chamber volume, the plasma needs to be placed as close as possible to the plasma metallic facing components. Although the plasma facing components are designed to withstand high heat fluxes, contact with the plasma is always a major concern in tokamak operations and, therefore, adequate plasma-wall clearance must be guaranteed. As already discussed, this is obtained by means of additional magnetic fields produced by suitable currents flowing in a number of poloidal field coils surrounding the plasma ring. These currents are generated by a power supply system driven in feedback by a plasma shape control system.

In the first experiments on tokamaks with elongated plasmas, feedback control was used only to stabilize the unstable mode. Successively, other geometrical parameters were controlled by feedback. The control of a few geometrical parameters is no longer sufficient when the plasma shape has to be guaranteed with very high accuracy. In these cases, usually the controlled shape geometrical descriptors are the distances between the plasma boundary and the vessel at some specific points. These plasma-wall distances are called *gaps*.

In the next-generation tokamak, the plasma-wall distance must be carefully controlled during the main part of the experiment with an accuracy of a few centimetres. When high performance is required, the strong output coupling calls for a model-based MIMO approach to obtain adequate closed-loop performance.

There are few examples of multivariable controllers used for position, current and shape control. In [34] normalized coprime factorization is used to control the shape of the DIII-D plasma. In [35, 36] the authors propose a

controller designed using the  $H_\infty$  technique, which has been used during normal tokamak operation to control simultaneously the plasma current, vertical position and some geometrical parameters. This design is described in detail in Chapter 8.

In [37] the authors describe the features of the new controller proposed for the JET tokamak, which has been called eXtreme Shape Controller (XSC). This new controller is the first example of a multivariable tokamak controller that allows one to control with high accuracy the overall plasma boundary, specified in terms of a certain number of gaps. The XSC, which has recently been implemented at JET, is able to operate with *extremely shaped* plasmas, *i.e.*, plasmas with high elongation. The design of the XSC is based on an optimal output regulation technique; this approach is described in Chapter 9.

A software suite called *XSC Tools* [38] has been developed to automate the design procedure of the XSC. These tools make use of GUIs to allow nonspecialist users to prepare new operating scenarios, without the help of modellers and control specialists. Once a new controller is generated, all its parameters are saved into a text file, which is used to perform the validation of the scenario via simulations. The same file is then loaded by the real-time code running on the actual plant, without any further processing. This feature guarantees that the controller running on the plant during the experiments is exactly the same as the one validated in simulation.

In the design of plasma shape controllers for operating tokamaks, an important tool that needs to be available is a detailed simulation code for the testing of new control algorithms before their use on real plasma discharges. Simulation tools are becoming increasingly important, mainly for the following reasons:

- the commissioning time dedicated to new control algorithms is usually very limited on most tokamaks, where the interest is mainly focused on the physical purpose of the experiments;
- the control algorithms are becoming more and more sophisticated; this makes their fine-tuning during the experiments almost impossible.

Besides models of the tokamak and the plasma, these simulation tools need to include models of the magnetic diagnostics and the power supplies. Moreover, they usually run the same real-time control code at the tokamak, in order to validate also the implementation of the control algorithm.

### 1.6.6 Other Magnetic Control Problems

The poloidal field coil system is mainly used for the control of plasma current, position and shape. In addition to this, there are some specific control problems arising on tokamaks where it is possible to resort again to the use of the poloidal field coils; two such problems are strike-point (Section 3.2) sweeping and boundary flux control.

Strike point sweeping is the movement of the plasma strike points, in the lower region of the vessel, at a prescribed frequency, with the aim of avoiding excessive heat in that region. During sweeping, the plasma boundary should ideally be maintained fixed and therefore the movement should occur only in the strike point region. In [39] the control schemes that have been proposed for the JET tokamak to perform sweeping are described and some experimental results are presented.

Plasma boundary flux control is used on tokamaks with the aim of increasing the fraction of plasma current supplied by noninductive means; this is a crucial step for steady-state, high-performance operation in future devices. If the plasma flux is kept constant, then all of the plasma current is induced by the additional heating and current drive devices available on the tokamak. If the power which equips these devices is sufficient, then a steady-state discharge is, in theory, possible. The paper [40] describes the way the plasma flux control is implemented at JET.

## Plasma Modelling

---

## Plasma Modelling for Magnetic Control

The aim of this chapter is to derive a linearized mathematical model describing the interaction between the plasma ring and the voltages applied to the poloidal field coils. This model will be of fundamental importance in the design of the plasma magnetic control system. To start with, the equations of the ideal magnetohydrodynamics theory will be presented; these equations will be used to characterize the equilibrium configurations of a plasma in a tokamak machine, and to derive a nonlinear dynamical model. Then, it is shown how to obtain a finite dimensional linear time-invariant model. This model will be completed in the next chapter including the output equations describing the parameters used to characterize the plasma shape and position.

### 2.1 The Ideal Magnetohydrodynamics Theory

Magnetohydrodynamics (MHD) [10, 41, 42] describes the basic behaviour of a magnetically confined plasma. In this theory the plasma is considered as a single fluid, that is, no distinction is made among the various particles constituting the plasma. The plasma is completely described once the local mass density  $\rho$  and the fluid velocity  $\mathbf{v}$  vector are assigned.

The fundamental laws that link these quantities are the mass conservation law

$$\frac{\partial}{\partial t} \rho + \nabla \cdot (\rho \mathbf{v}) = 0, \quad (2.1)$$

and Newton's law applied to an infinitesimal plasma element

$$\rho \frac{d}{dt} \mathbf{v} = \mathbf{J} \times \mathbf{B} - \nabla p, \quad (2.2)$$

where  $\mathbf{J}$  is the current density field,  $\mathbf{B}$  is the magnetic induction field, and  $p$  is the kinetic pressure inside the plasma. The coupling between the plasma and the electromagnetic field is given by the Lorentz force term  $\mathbf{J} \times \mathbf{B}$  in Equation 2.2.



Moreover, the electromagnetic fields have to satisfy Maxwell's equations

$$\nabla \cdot \mathbf{B} = 0 \quad (2.3a)$$

$$\nabla \times \mathbf{H} = \mathbf{J} \quad (2.3b)$$

$$\nabla \times \mathbf{E} = -\frac{\partial}{\partial t} \mathbf{B}. \quad (2.3c)$$

Equation 2.3a is Gauss's law for the magnetic induction field, Equation 2.3b is Ampere's law, which gives the relationship between the current density and the magnetic field intensity  $\mathbf{H}$ , and Equation 2.3c is Faraday's law; in Faraday's law  $\mathbf{E}$  represents the electrical field. In Ampere's law the time derivative of the displacement electric field (usually denoted by  $\mathbf{D}$ ) is neglected; this corresponds to neglecting parasitic capacitive effects. This assumption is consistent with the time scale of the phenomena involved.

Finally the constitutive relations

$$\mathbf{B} = \mu_0 \mathbf{H} \quad (2.4a)$$

$$\eta \mathbf{J} = \mathbf{E} + \mathbf{v} \times \mathbf{B} \quad (2.4b)$$

complete the set of ideal magnetohydrodynamic equations. These equations are summarized in Table 2.1.

**Table 2.1.** The ideal magnetohydrodynamical equations

$\nabla \cdot \mathbf{B} = 0$	$\frac{\partial}{\partial t} \rho + \nabla \cdot (\rho \mathbf{v}) = 0$
$\nabla \times \mathbf{B} = \mu_0 \mathbf{J}$	$\rho \frac{d}{dt} \mathbf{v} = \mathbf{J} \times \mathbf{B} - \nabla p$
$\nabla \times \mathbf{E} = -\frac{\partial}{\partial t} \mathbf{B}$	$\mathbf{E} + \mathbf{v} \times \mathbf{B} = \eta \mathbf{J}$

## 2.2 Magnetohydrodynamics in Axisymmetric Toroidal Geometry: the Poloidal Flux Function

Since a tokamak is an axisymmetric toroidal machine, it is convenient to write the magnetohydrodynamics equations in a three-dimensional cylindrical coordinates system  $(r, \varphi, z)$ , where the axis  $r = 0$  is the rotational axis of the tokamak.

In what follows:

- $\mathbf{r}$  will denote a generic point with cylindrical coordinate  $(r, \varphi, z)$ , where  $r$  is the radial coordinate,  $\varphi$  is the toroidal angle, and  $z$  is the height;  $\mathbf{i}_r$ ,  $\mathbf{i}_\varphi$  and  $\mathbf{i}_z$  will denote the axis unit vectors;

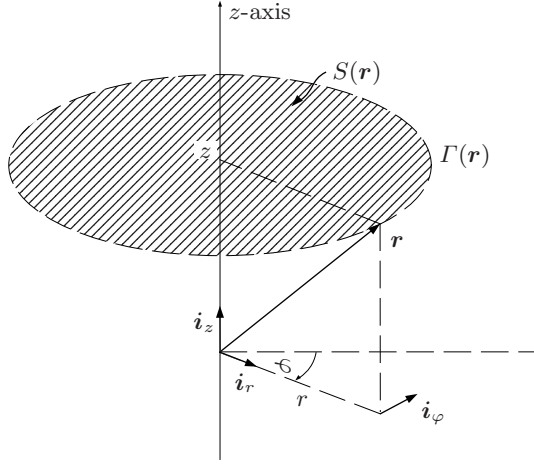


**Figure 2.1.** The cylindrical coordinate system

- $\Gamma(\mathbf{r})$  will denote the circumference given by the rotation of the point  $\mathbf{r}$  around the  $r = 0$  axis;
- $S(\mathbf{r})$  will denote a surface having  $\Gamma(\mathbf{r})$  as edge (see also Figure 2.1).

Given a generic vector  $\mathbf{A}$ , its components along the unit vectors will be denoted by  $A_r$ ,  $A_\varphi$ , and  $A_z$ , respectively, so as to have

$$\mathbf{A} = A_r \mathbf{i}_r + A_\varphi \mathbf{i}_\varphi + A_z \mathbf{i}_z.$$

In each point the direction parallel to the unit vector  $\mathbf{i}_\varphi$  is called toroidal, while the plane perpendicular to this direction is called poloidal; this plane is characterized by a constant toroidal angle  $\varphi$ .

Moreover, due to the toroidal axisymmetric geometry of a tokamak machine, it is possible to assume that all the quantities involved do not depend on the toroidal angle; as a consequence, again with reference to a generic vector  $\mathbf{A}$ , it is possible to assume

$$\frac{\partial}{\partial \varphi} \mathbf{A} = 0.$$

Making use of the axisymmetric assumption, Gauss's law (Equation 2.3a) in cylindrical coordinates can be written as

$$\frac{1}{r} \frac{\partial}{\partial r} r B_r + \frac{\partial}{\partial z} B_z = 0. \quad (2.5)$$

Now it is convenient to introduce the poloidal flux function

$$\psi(\mathbf{r}) = \frac{1}{2\pi} \int_{S(\mathbf{r})} \mathbf{B} \cdot d\mathbf{S}. \quad (2.6)$$

Since the surface integral in (2.6) does not depend on the particular surface  $S(\mathbf{r})$ , but only on its edge  $\Gamma(\mathbf{r})$ , choosing  $S(\mathbf{r})$  perpendicular at each point to  $\mathbf{i}_z$  (as in Figure 2.1), one obtains

$$\psi(\mathbf{r}) = \frac{1}{2\pi} \int_0^r \int_0^{2\pi} B_z(\rho, z) \rho \, d\rho \, d\varphi = \int_0^r \rho B_z(\rho, z) \, d\rho. \quad (2.7)$$

Differentiation of Equation 2.7 with respect to  $r$  gives

$$\frac{\partial}{\partial r} \psi = r B_z,$$

while differentiating the same equation with respect to  $z$ , and taking into account Equation 2.5, results in

$$\frac{\partial}{\partial z} \psi = -r B_r.$$

Hence the poloidal flux function and the magnetic inductance field are linked by the following equations

$$B_r = \frac{1}{r} \frac{\partial}{\partial z} \psi \quad (2.8a)$$

$$B_z = -\frac{1}{r} \frac{\partial}{\partial r} \psi. \quad (2.8b)$$

Equations 2.8, taking into account that  $\nabla \varphi = r^{-1} \mathbf{i}_\varphi$ , can be written in vectorial notation

$$\mathbf{B}_p = B_r \mathbf{i}_r + B_z \mathbf{i}_z = \nabla \psi \times \nabla \varphi, \quad (2.9)$$

where  $\mathbf{B}_p$  represents the projection of the magnetic induction field on the poloidal plane.

Note that the existence of a scalar function  $\psi$  satisfying Equations 2.8 is a consequence only of the divergenceless of the magnetic induction field. Now, applying the divergence operator to Ampere's law (2.3b), it is simple (taking into account that the divergence of a rotor is zero) to show that also the current density vector  $\mathbf{J}$  is divergenceless. Hence there will exist a scalar function  $f$  satisfying the relations

$$J_r = -\frac{1}{r} \frac{\partial}{\partial z} f \quad (2.10a)$$

$$J_z = \frac{1}{r} \frac{\partial}{\partial r} f. \quad (2.10b)$$

Ampere's law (2.3b), combined with the constitutive relation (2.4a) and the axisymmetric assumption, is written in cylindrical coordinates as

$$-\frac{\partial}{\partial z} B_\varphi = \mu_0 J_r \quad (2.11a)$$

$$\frac{\partial}{\partial z} B_r - \frac{\partial}{\partial r} B_z = \mu_0 J_\varphi \quad (2.11b)$$

$$\frac{1}{r} \frac{\partial}{\partial r} r B_\varphi = \mu_0 J_z. \quad (2.11c)$$

Combining Equations 2.10 with Equations 2.11a and 2.11c gives

$$B_\varphi = \mu_0 \frac{f}{r}.$$

Letting  $F(r, z) = \mu_0 f(r, z)$ , the toroidal component of the magnetic induction field can be written as

$$B_\varphi = F \nabla \varphi \cdot \mathbf{i}_\varphi. \quad (2.12)$$

Finally the magnetic induction field can be expressed through the two scalar functions  $\psi$  and  $F$  as

$$\mathbf{B} = \nabla \psi \times \nabla \varphi + F \nabla \varphi. \quad (2.13)$$

As already said, the first term on the right-hand side of Equation 2.13 gives the projection of the magnetic induction field on the poloidal plane (poloidal magnetic induction field), while the second term gives the toroidal component (toroidal magnetic inductance field). Substituting Equation 2.13 in Ampere's law (2.3b) gives

$$\begin{aligned} \mathbf{J} &= \mu_0^{-1} \nabla \times (\nabla \psi \times \nabla \varphi + F \nabla \varphi) \\ &= -\mu_0^{-1} \Delta^* \psi \nabla \varphi + \mu_0^{-1} \nabla F \times \nabla \varphi, \end{aligned} \quad (2.14)$$

where  $\Delta^*$  is the differential elliptic operator defined by the relation

$$\Delta^* \chi = r^2 \nabla \cdot (r^{-2} \nabla \chi) = r \frac{\partial}{\partial r} \left( \frac{1}{r} \frac{\partial}{\partial r} \chi \right) + \frac{\partial^2}{\partial z^2} \chi.$$

Projection of Equation 2.14 along the toroidal direction gives

$$\Delta^* \psi = -\mu_0 r J_\varphi, \quad (2.15)$$

where  $J_\varphi$  is the toroidal current density.

Another useful relation can be found between the toroidal component of the electrical field and the time derivative of the poloidal flux function. Starting from Faraday's law (2.3c) and applying the Kelvin–Stokes theorem, one obtains

$$\begin{aligned} \oint_{\Gamma(r)} \mathbf{E} \cdot d\mathbf{l} &= -\frac{\partial}{\partial t} \int_{S(r)} \mathbf{B} \cdot d\mathbf{S} \\ &= -2\pi \frac{\partial}{\partial t} \psi, \end{aligned}$$

from which it can be easily obtained that

$$E_\varphi = -\frac{1}{r} \frac{\partial}{\partial t} \psi. \quad (2.16)$$

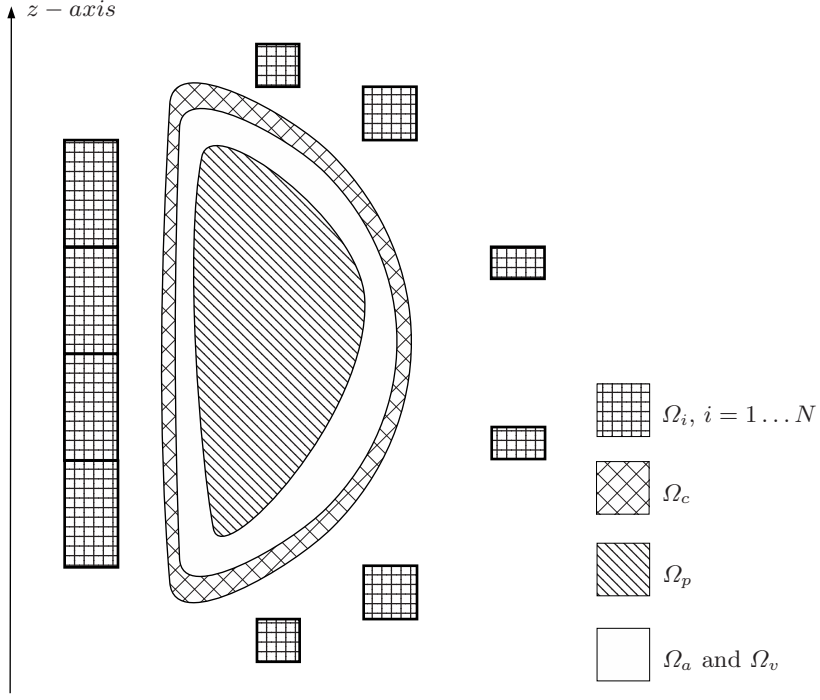


**Figure 2.2.** The poloidal cross-section of a tokamak machine can be partitioned into regions occupied by the plasma ( $\Omega_p$ ), by the conducting structure ( $\Omega_c$ ), by the poloidal field coils ( $\Omega_i, i = 1 \dots N$ ), by the air ( $\Omega_a$ ) and by the vacuum ( $\Omega_v$ ).

### 2.3 A Plasmaless Model

In this section an electromagnetic model of a tokamak in the absence of the plasma will be derived. This model will enable one to evaluate the poloidal flux function at each point in space, given the voltages applied to the poloidal field coils. With reference to Figure 2.2 the poloidal plane can be divided into two types of region: the air and vacuum region ( $\Omega_a \cup \Omega_v$ ), and the region  $\Omega_m = \Omega_c \cup \Omega_1 \cup \Omega_2 \cup \dots \cup \Omega_N$  occupied by conducting materials. The set  $\mathcal{L} = \Omega_p \cup \Omega_v$  is the vacuum vessel region, that is the space inside the tokamak that the plasma can occupy.

In  $\Omega_m$  Ohm's law takes the form

$$\mathbf{J} = \sigma(\mathbf{E} + \mathbf{E}_m), \quad (2.17)$$

where  $\sigma$  is the conductivity (the inverse of the resistivity  $\eta$ ) of the materials involved, and  $\mathbf{E}_m$  is the electromotive field supplying the electromotive force to the poloidal field coils ( $\mathbf{E}_m = 0$  in  $\Omega_c$ ).

Integrating Equation 2.17 along the circuit individuated by the closed line  $\Gamma(\mathbf{r})$  gives

$$\oint_{\Gamma(\mathbf{r})} \mathbf{J} \cdot d\mathbf{l} = \sigma \left( \oint_{\Gamma(\mathbf{r})} \mathbf{E} \cdot d\mathbf{l} + \oint_{\Gamma(\mathbf{r})} \mathbf{E}_m \cdot d\mathbf{l} \right),$$

from which, invoking again the axisymmetric assumption, and taking into account Equation 2.16, can be obtained

$$2\pi r J_\varphi = -2\pi\sigma \frac{\partial}{\partial t} \psi + \sigma V, \quad (2.18)$$

where

$$V = \oint_{\Gamma(\mathbf{r})} \mathbf{E}_m \cdot d\mathbf{l},$$

represents the electromotive force on the  $\Gamma(\mathbf{r})$  circuit. It is evident that the electromotive force is different from zero only in the regions where the active poloidal field coils are located; moreover, in each of these regions,  $V$  can be assumed to be constant, and so it is possible to write

$$V(\mathbf{r}, t) = \sum_{i=1}^N V_i(t) g_i(\mathbf{r}), \quad (2.19)$$

where  $g_i$  is the characteristic function of the  $\Omega_i$  set, that is

$$g_i(\mathbf{r}) = \begin{cases} 1, & \text{if } \mathbf{r} \in \Omega_i \\ 0, & \text{if } \mathbf{r} \notin \Omega_i. \end{cases}$$

Combining Equations 2.15 and 2.18, and considering that  $J_\varphi = 0$  in  $\mathcal{L}$  and  $\Omega_a$ , one obtains that the poloidal flux function in the absence of the plasma must satisfy the following partial differential equation

$$\Delta^* \psi = \begin{cases} 0, & \text{if } \mathbf{r} \in \Omega_v \cup \Omega_a \\ \mu_0 \sigma \frac{\partial}{\partial t} \psi, & \text{if } \mathbf{r} \in \Omega_c \\ \mu_0 \sigma \frac{\partial}{\partial t} \psi - \frac{\mu_0 \sigma}{2\pi} V_i, & \text{if } \mathbf{r} \in \Omega_i, \quad i = 1 \dots N. \end{cases} \quad (2.20)$$

To find a unique solution to this equation, initial and boundary conditions must be provided

$$\psi(r, z, t)|_{t=0} = \psi_0(r, z) \quad (2.21a)$$

$$\psi(r, z, t)|_{r=0} = 0 \quad (2.21b)$$

$$\lim_{r \rightarrow \infty} \psi(r, z, t) = 0. \quad (2.21c)$$

The initial condition (2.21a) provides the flux distribution at the starting time; if it is assumed that at this time there is no current distribution in the conducting region, then this initial distribution can be assumed to be zero everywhere. The boundary condition (2.21b) is a consequence of the poloidal flux definition, whereas (2.21c) is a regularity assumption of the magnetic induction field as  $\mathbf{r} \rightarrow \infty$ .

Once the time behaviour of the voltages  $V_i$  applied to the poloidal field coils is assigned, it is possible in principle to integrate the partial differential Equation 2.20 with the conditions (2.21) to evaluate the poloidal flux function at each point of the poloidal plane. The difficulties in finding an analytical solution to this problem justify the use of a numerical approach based on finite element and Galerkin methods. Following [43], let

$$J_\varphi(\mathbf{r}, t) = \sum_{h=1}^{n_c} I_h(t) q_h(\mathbf{r}), \quad (2.22)$$

in such a way as to approximate the toroidal current density with the sum of  $n_c$  base functions  $q_h$ , weighted by unknown coefficients  $I_h$ . Each base function  $q_h$  has a compact support  $D_h$  (i.e., it is zero outside  $D_h$ ), and satisfies the conditions

$$\nabla \cdot (q_h \mathbf{i}_\varphi) = 0 \quad (2.23a)$$

$$\frac{\partial}{\partial \varphi} q_h = 0 \quad (2.23b)$$

$$\int_{D_h} q_h dS = 1. \quad (2.23c)$$

In this way the region  $\Omega_m$  is discretized in a finite number of circuits, having  $D_h$  as cross-section on the poloidal plane. The subsets  $D_h$  satisfy the properties

$$\bigcup_{h=1}^{n_c} D_h = \Omega_m \quad (2.24)$$

$$D_h \cap D_k = \emptyset \text{ when } h \neq k \quad (2.25)$$

$$\exists k \in \{c, 1, \dots, N\} : D_h \cap \Omega_k \neq \emptyset \Rightarrow D_h \subseteq \Omega_k. \quad (2.26)$$

Therefore the subsets  $D_h$  completely cover the  $\Omega_m$  region, the intersection between two of these subsets is empty, and finally each domain  $D_h$  can have a no empty intersection with at most one of the regions  $\Omega_c, \Omega_1, \dots, \Omega_N$ .

In Section A.1 it is shown that a general solution of Equation 2.15 can be written as

$$\psi(\mathbf{r}, t) = \int_{\mathbb{R}^2} J_\varphi(\mathbf{r}', t) G_0(\mathbf{r}, \mathbf{r}') dS', \quad (2.27)$$

where  $G_0(\mathbf{r}, \mathbf{r}')$  is the free space Green's function defined in (A.4). Equation 2.27 enables one to write

$$\psi(\mathbf{r}, t) = \sum_{h=1}^{n_c} I_h(t) \tilde{q}_h(\mathbf{r}), \quad (2.28)$$

where

$$\tilde{q}_h(\mathbf{r}) = \int_{\Omega_m} q_h(\mathbf{r}') G_0(\mathbf{r}, \mathbf{r}') dS'.$$

Equation 2.18 can be written as

$$\frac{1}{\sigma} J_\varphi = -\frac{1}{r} \frac{\partial}{\partial t} \psi + \frac{1}{2\pi r} V. \quad (2.29)$$

Multiplying both sides of (2.29) by  $q_h$ , and integrating over the volume  $V_m$  obtained by rotating the domain  $\Omega_m$  around the  $z$ -axis, the following equality is obtained

$$\int_{V_m} \frac{1}{\sigma} J_\varphi q_h d\tau = - \int_{V_m} \frac{1}{r} q_h \frac{\partial}{\partial t} \psi d\tau + \frac{1}{2\pi} \int_{V_m} \frac{1}{r} V q_h d\tau. \quad (2.30)$$

Now

$$\begin{aligned} \int_{V_m} \frac{1}{\sigma} J_\varphi q_h d\tau &= \sum_{k=1}^{n_c} I_k \int_{V_m} \frac{q_k q_h}{\sigma} d\tau \\ &= \sum_{k=1}^{n_c} I_k \int_0^{2\pi} \int_{\Omega_m} \frac{q_k q_h}{\sigma} r d\varphi dS \\ &= \sum_{k=1}^{n_c} I_k 2\pi \int_{\Omega_m} r \frac{q_k q_h}{\sigma} dS \\ &= \sum_{k=1}^{n_c} R_{hk} I_k; \end{aligned}$$

similarly

$$\begin{aligned} \int_{V_m} \frac{1}{r} q_h \frac{\partial}{\partial t} \psi d\tau &= \sum_{k=1}^{n_c} \dot{I}_k \int_{V_m} \frac{\tilde{q}_k q_h}{r} d\tau \\ &= \sum_{k=1}^{n_c} \dot{I}_k 2\pi \int_{\Omega_m} \tilde{q}_k q_h dS \\ &= \sum_{k=1}^{n_c} L_{hk} \dot{I}_k, \end{aligned}$$

and finally



$$\begin{aligned}
\frac{1}{2\pi} \int_{V_m} \frac{1}{r} V q_h d\tau &= \frac{1}{2\pi} \sum_{l=1}^N V_l \int_{V_m} \frac{g_l q_h}{r} d\tau \\
&= \sum_{l=1}^N V_l \int_{\Omega_m} g_l q_h dS \\
&= \sum_{l=1}^N B_{hl} V_l,
\end{aligned}$$

where the dot over a time-varying function denotes its time derivative, and

$$R_{hk} = 2\pi \int_{\Omega_m} r \frac{q_k q_h}{\sigma} dS \quad (2.31a)$$

$$L_{hk} = 2\pi \int_{\Omega_m} \tilde{q}_k q_h dS \quad (2.31b)$$

$$B_{hl} = \int_{\Omega_m} g_l q_h dS, \quad (2.31c)$$

with  $h = 1, \dots, n_c$ ,  $k = 1, \dots, n_c$ , and  $l = 1, \dots, N$ . Equation 2.30 can be written in the form

$$\sum_{k=1}^{n_c} L_{hk} \dot{I}_k + \sum_{k=1}^{n_c} R_{hk} I_k = \sum_{l=1}^N B_{hl} V_l. \quad (2.32)$$

Note that

$$B_{hl} = \begin{cases} 1, & \text{if } D_h \subseteq \Omega_l \\ 0, & \text{if } D_h \not\subseteq \Omega_l \end{cases} \quad (2.33)$$

$$R_{hk} = 0 \text{ if } h \neq k. \quad (2.34)$$

Now defining the matrices  $L_c \in \mathbb{R}^{n_c \times n_c}$ ,  $R_c \in \mathbb{R}^{n_c \times n_c}$ , and  $B_c \in \mathbb{R}^{n_c \times N}$ , whose elements are the scalars  $L_{hk}$ ,  $R_{hk}$ , and  $B_{hl}$ , respectively, and the vectors  $\tilde{x} = (I_1 \ I_2 \ \dots \ I_{n_c})^T \in \mathbb{R}^{n_c}$ ,  $u = (V_1 \ V_2 \ \dots \ V_N)^T \in \mathbb{R}^N$ , the  $n_c$  equations (2.32) can be written in matrix form as

$$L_c \dot{\tilde{x}} + R_c \tilde{x} = B_c u. \quad (2.35)$$

As can be noted, Equation 2.35 is in the same form as a system consisting of  $n_c$  circuits with inductors, resistors, and voltage sources. The generic element  $L_{hk}$  of the  $L_c$  matrix corresponds to the mutual inductance between the circuit  $h$  and the circuit  $k$ , while the diagonal element  $L_{hh}$  corresponds to the self-inductance of the circuit  $h$ ; it is a basic property of circuit theory that the inductance matrix  $L$  is symmetric, diagonal dominant and invertible. Similarly  $R_{hh}$  corresponds to the resistance of the circuit  $h$ ; therefore the diagonal matrix  $R_c$  is called the resistance matrix. A voltage source is present only on

the circuits contained in one of the  $\Omega_k$  regions. To simplify the notation, it can be assumed that  $D_h = \Omega_h$  for  $h = 1, 2, \dots, N$ ; in such a way the first  $N$  subsets  $D_h$  are equal to the  $N$  regions  $\Omega_k$  containing the poloidal field coils, and these regions are discretized in only one circuit. If this is the case, the  $L_c$ ,  $R_c$  and  $B_c$  matrices, and the vector  $\tilde{x}$  can be decomposed as

$$L_c = \begin{pmatrix} L_a & L_{ab} \\ L_{ab}^T & L_b \end{pmatrix} \quad (2.36a)$$

$$R_c = \begin{pmatrix} R_a & 0 \\ 0 & R_b \end{pmatrix} \quad (2.36b)$$

$$B_c = \begin{pmatrix} I \\ 0 \end{pmatrix} \quad (2.36c)$$

$$\tilde{x} = \begin{pmatrix} x_a \\ x_e \end{pmatrix}, \quad (2.36d)$$

where the matrices  $L_{aa}$  and  $R_{aa}$  are of dimension  $n_c$ , and  $I$  denotes the identity matrix. In this way (2.35) can be divided into two equations: one related to the currents flowing in the poloidal field coils (the active circuits), and one related to the currents flowing in the other conducting structures (the passive circuits)

$$L_a \dot{x}_a + L_{ab} \dot{x}_e + R_a x_a = u \quad (2.37a)$$

$$L_{ab}^T \dot{x}_a + L_e \dot{x}_e + R_e x_e = 0. \quad (2.37b)$$

Equations 2.37 show that the active circuits currents can be controlled using the input voltages vector  $u$ ; the time variations of these currents are opposed by the *eddy currents* induced in the conducting structures. Note that once the vector  $\tilde{x}$  is assigned, which is equivalent to assigning the distribution of the toroidal current density, using Equation 2.28 it is possible to evaluate the poloidal flux function at each point of the poloidal plane.

## 2.4 The Plasma Equilibrium

In the previous section a model describing the electromagnetic behaviour of a tokamak machine in the absence of the plasma, has been derived. As Equation 2.35 shows, this model is linear; in the next sections of this chapter it will be shown that the presence of the plasma makes the model nonlinear, and that the added complexity can be overcome by resorting to a linearized model valid in the neighbourhood of an equilibrium point. The first step, therefore, aims at characterizing the plasma equilibrium configurations.

The balance between the plasma pressure and the magnetic confinement forces can be studied with the aid of the equations written in Sections 2.1 and 2.2. The basic condition for equilibrium is that the overall force acting on an infinitesimal plasma volume is zero; this is expressed by the equation

$$\nabla p = \mathbf{J} \times \mathbf{B}, \quad (2.38)$$

from which it can be obtained that

$$\mathbf{B} \cdot \nabla p = 0 \quad (2.39a)$$

$$\mathbf{J} \cdot \nabla p = 0. \quad (2.39b)$$

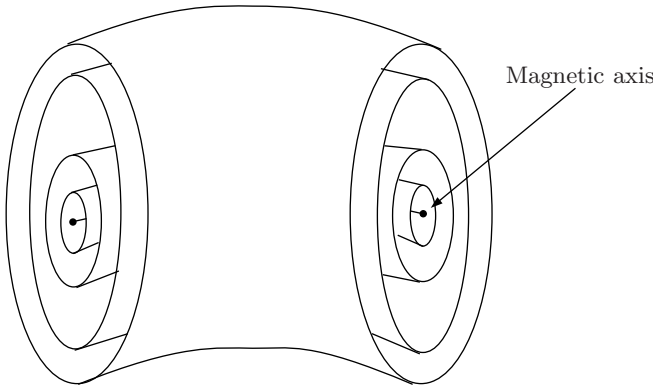


**Figure 2.3.** Isobaric surfaces in a plasma equilibrium configuration

Equations 2.39 show that the field lines of the magnetic induction and of the current density lie on isobaric surfaces (surfaces where the pressure is constant). For most plasma equilibria the pressure is maximum near the centre of the poloidal cross-section of the plasma, and the isobaric surfaces are toroidally nested as shown in Figure 2.3 (see [10] for a detailed explanation). As a consequence of the fact that the magnetic field lines lie on the isobaric surfaces, these surfaces are also called magnetic surfaces. The limiting magnetic surface, which approaches a single magnetic line where the pressure is maximum, is called the magnetic axis.

Now it follows from Equation 2.8 that

$$\mathbf{B} \cdot \nabla \psi = 0,$$

so the magnetic (or isobaric) surfaces also coincide with the constant poloidal flux surfaces. Hence on the poloidal plane the current density, the magnetic induction and the pressure are constant on each line level of the  $\psi$  function. As a consequence, it is possible to consider these quantities (and the others related to them) as dependent only on the poloidal flux

$$\begin{aligned}
\mathbf{B} &= \mathbf{B}(\psi) \\
\mathbf{J} &= \mathbf{J}(\psi) \\
p &= p(\psi).
\end{aligned}$$

Starting from the force equilibrium Equation 2.38, using the equalities (2.13) and (2.14), and taking into account that  $p$  and  $F$  are functions only of  $\psi$ , it is possible to obtain that

$$\nabla p = -\frac{1}{r} J_\varphi \nabla \psi - \frac{1}{\mu_0 r^2} F \nabla F. \quad (2.40)$$

Considering that

$$\nabla p = \frac{d}{d\psi} p \nabla \psi \quad (2.41)$$

$$\nabla F = \frac{d}{d\psi} F \nabla \psi, \quad (2.42)$$

then

$$J_\varphi = -r \frac{d}{d\psi} p - \frac{1}{\mu_0 r} F \frac{d}{d\psi} F. \quad (2.43)$$

Putting together Equations 2.15 and 2.43 the celebrated *Grad-Shafranov* equation is obtained

$$\Delta^* \psi = -\mu_0 r^2 \frac{d}{d\psi} p - F \frac{d}{d\psi} F. \quad (2.44)$$

The plasma equilibrium is then completely characterized by the following nonlinear partial differential problem

$$\Delta^* \psi = \begin{cases} 0, & \text{if } \mathbf{r} \in \Omega_v \cup \Omega_a \\ \mu_0 r J_\varphi, & \text{if } \mathbf{r} \in \Omega_m \\ -\mu_0 r^2 \frac{d}{d\psi} p - F \frac{d}{d\psi} F, & \text{if } \mathbf{r} \in \Omega_p. \end{cases} \quad (2.45)$$

$$\psi(r, z)|_{r=0} = 0 \quad (2.46a)$$

$$\lim_{r \rightarrow \infty} \psi(r, z) = 0. \quad (2.46b)$$

This problem can be solved when the current density external to the plasma region, and the functions  $p(\psi)$  and  $F(\psi)$  have been assigned. Note that this is a free boundary problem, the boundary  $\partial\Omega_p$  of  $\Omega_p$  being one of the unknowns to be determined.

Several numerical codes [44, 45, 46, 47] have been developed to solve this problem. The choice of the functions  $p(\psi)$  and  $F(\psi)$  determine the toroidal

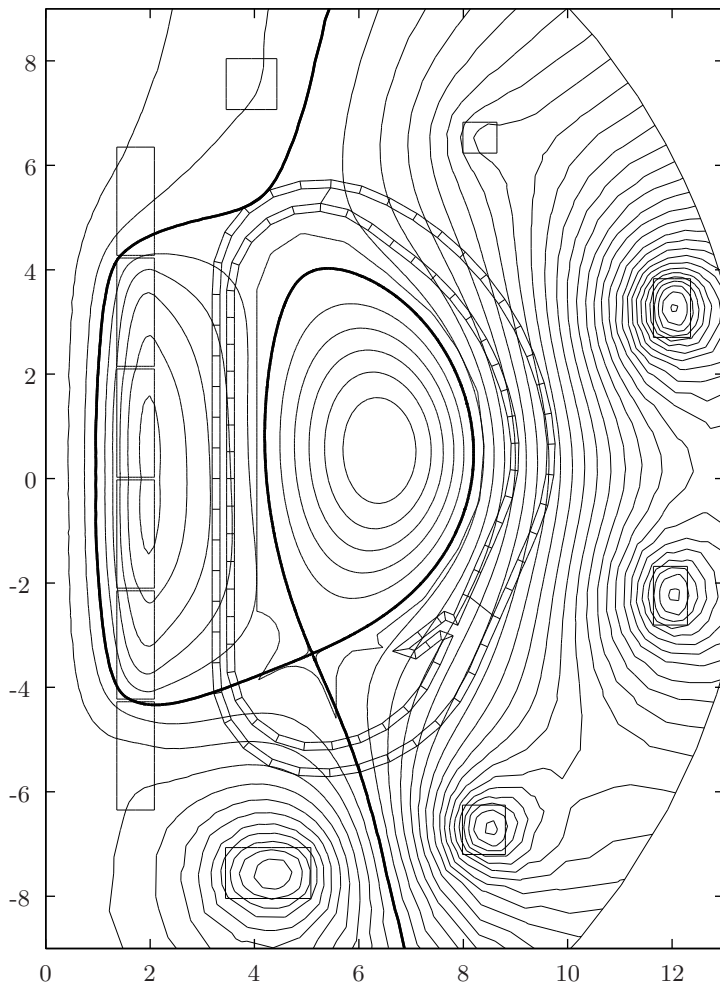


**Figure 2.4.** Constant level curves of the poloidal flux function for a plasma equilibrium as determined by the CREATE-L numerical code [48]. The thicker line corresponds to the value of the poloidal flux at the plasma boundary.

current density inside the plasma (see Equation 2.43). Although the problem of determining this current density could be, in principle, included in Equations 2.45 and 2.46 adding a certain number of equations related to the diffusion and to the transport of the plasma particles, it is simpler to adopt here an approach based on experimental evidence [49] and assign  $J_\varphi$  inside the plasma as a parameterized function. The parameters used to characterize the toroidal current density are the total plasma current  $I_p$ , the poloidal beta  $\beta_p$ , and the internal inductance  $l_i$ ; these quantities are defined as

$$I_p = \int_{\Omega_p} J_\varphi \, dS \quad (2.47a)$$

$$\beta_p = \frac{4}{\mu_0 r_c I_p^2} \int_{V_p} p \, d\tau \quad (2.47b)$$

$$l_i = \frac{4}{\mu_0 r_c I_p^2} \int_{V_p} \frac{\|\mathbf{B}_p\|^2}{2\mu_0} \, d\tau, \quad (2.47c)$$

where  $r_c$  is the horizontal coordinate of the plasma current centroid  $(r_c, z_c)$  defined as

$$r_c = \left( \frac{1}{I_p} \int_{\Omega_p} r^2 J_\varphi \, dS \right)^{\frac{1}{2}} \quad (2.48a)$$

$$z_c = \frac{1}{I_p} \int_{\Omega_p} z J_\varphi \, dS. \quad (2.48b)$$

The total plasma current is the current flowing through the poloidal plane in the plasma region. The poloidal beta is a measure of the efficiency of the plasma confinement: indeed, it is a measure of the ratio between the pressure energy and the magnetic energy in the plasma. The internal inductance is a dimensionless quantity and it is linked to the magnetic energy in the plasma region. The plasma current centroid is a sort of geometrical centre for the plasma region.

Coming back to the problem of characterizing the toroidal current density inside the plasma region, in [49] the following expression is proposed

$$J_\varphi = \lambda \left[ \beta_0 \frac{r}{r_0} + (1 - \beta_0) \frac{r_0}{r} \right] (1 - \tilde{\psi}^m)^n, \quad (2.49)$$

where

$$\tilde{\psi} = \frac{\psi - \psi_a}{\psi_b - \psi_a}$$

is the so-called normalized flux,  $\psi_b$  and  $\psi_a$  being the flux values at the plasma boundary and at the magnetic axis, respectively,  $r_0$  the horizontal coordinate of a characteristic point inside the vacuum vessel (typically the centre of the chamber), and  $\lambda$ ,  $\beta_0$ ,  $m$  and  $n$  parameters which are related to  $\beta_p$ ,  $l_i$  and  $I_p$ . Once these parameters are assigned, it is possible to solve the problem given by Equations 2.45 and 2.46, evaluate the poloidal flux function, and hence characterize the plasma equilibrium.

As seen in Section 2.3 the toroidal current density  $J_\varphi$  outside the plasma region is completely defined by the vector  $\tilde{x}$ , whose components represent the current flowing in each region  $D_h$ ; while inside the plasma the toroidal current density is completely defined by the two-dimensional vector  $w = (\beta_p \, l_i)^T$  and by  $I_p$ . Therefore at each point  $\mathbf{r}$  of the poloidal plane it is possible to write

$$\psi(\mathbf{r}) = \gamma_1(\mathbf{r}, \tilde{x}, w, I_p), \quad (2.50)$$

where the function  $\gamma_1$  is not given analytically, but can be computed numerically by a solver of the problem (2.45) and (2.46). A typical result obtained using the equilibrium solver of the CREATE-L code [48] is shown in Figure 2.4.

## 2.5 A Linearized Model for Plasma Behaviour

In this section a linearized model of the plasma will be derived. This model describes the plasma behaviour, in a neighbourhood of an equilibrium configuration, from an electromagnetic point of view. This model will be used for the plasma shape and position control system design in later chapters. The fundamental assumption made to derive this model is that the mass density of the plasma can be considered very small, so that the inertial term in Equation 2.2 becomes negligible. This assumption is certainly satisfied on the typical time scale considered in the shape and position control design problem. If this is the case, the plasma equilibrium Equation 2.38 is satisfied at each time instant. In other words the plasma evolves through a sequence of static equilibria. The only dynamic behaviour is in the time evolution of the currents flowing in the conducting structures, for which it is possible to obtain a finite-dimensional model using the approach of Section 2.3.

Since Equation 2.15 continues to hold, it is possible to use again the free space Green's function defined in (A.4) to express the poloidal flux function

$$\begin{aligned}\psi(\mathbf{r}, t) &= \int_{\mathbb{R}^2} J_\varphi(\mathbf{r}', t) G_0(\mathbf{r}, \mathbf{r}') dS' \\ &= \int_{\Omega_m} J_\varphi(\mathbf{r}', t) G_0(\mathbf{r}, \mathbf{r}') dS' + \int_{\Omega_p} J_\varphi(\mathbf{r}', t) G_0(\mathbf{r}, \mathbf{r}') dS' \\ &= \psi_m(\mathbf{r}, t) + \psi_p(\mathbf{r}, t).\end{aligned}\tag{2.51}$$

The first term in (2.51) gives the flux produced by the current flowing in the conducting structures, while the second term gives the flux produced by the current distribution in the plasma. Now

$$E_\varphi = -\frac{1}{r} \frac{\partial}{\partial t} \psi = -\frac{1}{r} \frac{\partial}{\partial t} \psi_m - \frac{1}{r} \frac{\partial}{\partial t} \psi_p,\tag{2.52}$$

therefore, starting again from Equation 2.30 and repeating the same mathematical derivations of Section 2.3, it is possible to arrive at the equation

$$\sum_{k=1}^{n_c} L_{hk} \dot{I}_k + \sum_{k=1}^{n_c} R_{hk} I_k + \dot{\Psi}_{p_h} = \sum_{l=1}^N B_{hl} V_l,\tag{2.53}$$

where  $L_{hk}$ ,  $R_{hk}$ ,  $B_{hl}$  have been introduced in Equations 2.31, and

$$\Psi_{p_h} = 2\pi \int_{\Omega_m} \psi_p q_h dS.\tag{2.54}$$

The term  $\dot{\Psi}_{p_h}$  in Equation 2.53 represents the electromotive force which appears on the circuit  $h$  as a consequence of the time variations of the current density inside the plasma. These variations are due to changes in the plasma current internal profile, or also to the movements of the plasma ring. Defining the vector  $\Psi_p = (\Psi_{p_1} \ \Psi_{p_2} \ \dots \ \Psi_{p_{n_c}})^T \in \mathbb{R}^{n_c}$ , and considering Equation 2.53 for each circuit, the following matrix equation is obtained

$$L_c \dot{\tilde{x}} + R_c \tilde{x} + \dot{\Psi}_p = B_c u. \quad (2.55)$$

Equation 2.55 defines the dynamic behaviour of the currents flowing in the conducting structures in the presence of the plasma. The  $\Psi_p$  vector depends only on the flux produced by the plasma on these structures; it can be calculated solving an equilibrium problem when the vectors  $\tilde{x}$  and  $w$ , and the plasma current  $I_p$  have been assigned. In other words it is possible to write

$$\Psi_p = \gamma_2(\tilde{x}, w, I_p), \quad (2.56)$$

where the vectorial function  $\gamma_2$  is computed using one of the numerical codes cited in Section 2.4.

Putting together Equations 2.55 and 2.56, the following finite-dimensional nonlinear differential equation is obtained

$$L_c \dot{\tilde{x}} + R_c \tilde{x} + \frac{d}{dt} \gamma_2(\tilde{x}, w, I_p) = B_c u. \quad (2.57)$$

Equation 2.57 can be linearized in the neighbourhood of an equilibrium point  $(\tilde{x}_0, w_0, I_{p_0})$ ; indeed letting

$$\begin{aligned} \tilde{x} &= \tilde{x}_0 + \delta \tilde{x} \\ w &= w_0 + \delta w \\ I_p &= I_{p_0} + \delta I_p \\ u &= u_0 + \delta u = R_c \tilde{x}_0 + \delta u, \end{aligned}$$

and using the standard linearization procedure, it is possible to write

$$\left( L_c + \left[ \frac{\partial}{\partial \tilde{x}} \gamma_2 \right]_0 \right) \delta \dot{\tilde{x}} + R_c \delta \tilde{x} + \left[ \frac{\partial}{\partial w} \gamma_2 \right]_0 \delta \dot{w} + \left[ \frac{\partial}{\partial I_p} \gamma_2 \right]_0 \delta \dot{I}_p = B_c \delta u, \quad (2.58)$$

where the subscript 0 denotes that the Jacobian matrices have to be evaluated at the considered equilibrium point. In Equation 2.58 the plasma current variation  $\delta I_p$  appears as an input parameter; in other words it cannot be determined by the equation itself, but it has to be assigned. Since the plasma current is one of the parameters that are controlled, this problem needs to be solved, since it is preferable to be able to express  $\delta I_p$  as an output of the model. Several methods can be used to overcome this problem; most of them are based on neglecting the plasma resistivity and assuming the conservation of some physical quantity: the plasma current itself, the poloidal flux averaged on the



plasma region, the poloidal flux at the magnetic axis, *etc.* These approaches give for the plasma current variation an equation of the type

$$L_p \delta \dot{I}_p + M_{pc} \delta \ddot{x} + M_{pw} \delta \dot{w} = 0. \quad (2.59)$$

Interestingly, Equation 2.59 shows that, from the point of view of the total current, the plasma can be seen as just another circuit which is added to the ones used to model the conducting structures of the machine; the absence in Equation 2.59 of a resistive term is a consequence of the assumption on plasma resistivity.

Now letting  $x = (\tilde{x} \ I_p)^T$ , and defining

$$L^* = \begin{pmatrix} L_c + \left[ \frac{\partial}{\partial \tilde{x}} \gamma_2 \right]_0 & \left[ \frac{\partial}{\partial I_p} \gamma_2 \right]_0 \\ M_{pc} & L_p \end{pmatrix} \quad (2.60)$$

$$R = \begin{pmatrix} R_c & 0 \\ 0 & 0 \end{pmatrix} \quad (2.61)$$

$$E = \begin{pmatrix} \left[ \frac{\partial}{\partial w} \gamma_2 \right]_0 \\ 0 \end{pmatrix} \quad (2.62)$$

$$B = \begin{pmatrix} B_c \\ 0 \end{pmatrix}, \quad (2.63)$$

one obtains the final linearized model

$$L^* \delta \dot{x} + R \delta x + E \delta \dot{w} = B \delta u, \quad (2.64)$$

where the  $L^*$  matrix is often called the *modified inductance matrix*. This model gives only the evolution of the currents in the conducting structures and of the total plasma current. These variables play the role of state variables of the plant to be controlled; Equation 2.64 has to be completed with the static equation relating the inputs (the  $u$  vector) and the state variables to the output variables to be controlled. This equation will be derived in Chapter 3.

The matrices in Equation 2.64 are calculated by using numerical codes, for instance those described in [48, 26]. The dimension of the state space vector  $x$  depends on the number of finite elements used to discretize the tokamak structure; typical values range from about 100 to 200 depending on the size of the machine.

---

## The Plasma Boundary and its Identification

As seen in the previous chapter, the magnetic confinement of the plasma in tokamak machines is obtained via the interaction of the plasma with an external electromagnetic field.

Unfortunately, when high elongation of the plasma column is required, in other words when the plasma vertical dimension is larger than the radial dimension, then the equilibrium configuration between the plasma column and the external field is unstable, *i.e.*, small perturbations from the equilibrium may cause large movements of the plasma. Hence the use of a feedback system for position and shape control becomes mandatory. To this end, measurement of the geometrical parameters is necessary to perform feedback control. Since some of these parameters are not directly measurable, they must be estimated, starting from the set of available data. This chapter focuses on this estimation problem. To start with, the plasma boundary is precisely defined; it will be shown that the plasma boundary is a closed curve lying on the poloidal plane, corresponding to a constant level curve of the poloidal flux function. In principle an infinite number of points are necessary to completely characterize this curve from a geometrical point of view; however it turns out that a finite number of parameters can be used to control the overall plasma boundary effectively; these plasma boundary descriptors are introduced in Section 3.2.

As already said, estimation of the plasma boundary descriptors has to be carried out using the available magnetic measurements. For this reason in Section 3.3 the magnetic sensors that are usually available in a modern tokamak are described.

Finally, a general algorithm that can be used to solve this estimation problem is discussed.

### 3.1 Plasma Boundary Definition

The plasma is a rarefied conductive gas placed in the vacuum chamber of the tokamak. Therefore in principle it is not possible to define in an unam-

biguous way its boundary, that is the boundary of the region  $\Omega_p$  occupied by the plasma. A practical definition, which is universally accepted (see, for example, [50, 51]), is based on the magnetic configuration when the plasma is in equilibrium. The plasma boundary is then defined as the outermost closed magnetic surface entirely contained in the vacuum vessel. This is justified by the fact that the plasma particles in their motion follow the magnetic field lines. As a consequence particles following a magnetic line which is inside this surface will remain in the plasma interior, while a particle following a magnetic field line external to this surface will collide with the mechanical structures surrounding the plasma.

As seen in Chapter 2, on the poloidal plane the magnetic lines are also constant level curves for the poloidal flux function. Therefore the plasma boundary must be one of these constant level lines. Recalling that  $\mathcal{L}$  denotes the vacuum vessel region, the plasma boundary has the property to be the largest closed line completely included in  $\mathcal{L}$ . The boundary  $\partial\mathcal{L}$  of the vacuum vessel region is a material wall of the tokamak often called the tokamak first wall. Two cases in practice can happen:

1.  $\partial\Omega_p$  and  $\partial\mathcal{L}$  have a point in common; this is the case of the so-called *limiter* plasmas (Figure 3.1);
2.  $\partial\Omega_p$  and  $\partial\mathcal{L}$  do not have any point in common, this is the case of the so called *divertor* or *diverted* plasmas (Figure 3.2).

In the latter case the plasma boundary is the *separatrix* between the closed and the opened level curves of the function  $\psi$ . From a topological point of view, the separatrix is characterized by the presence of one (or more) *X-point*. An X-point is a saddle point for the flux function, hence this point is characterized by the fact that the flux derivatives with respect to  $r$  and  $z$  are zero; this also implies that the magnetic induction field is zero, and for this reason this point is also called a *null point*. For divertor plasmas, the level curve defining the plasma boundary continues below the X-point along two segments, called *baffles*, whose extensions intersect the first wall. These intersection points define the two *strike points*  $S_1$  and  $S_2$  (Figure 3.2). The components of the tokamak mechanical structure where the strike points are located are the *divertors*. As will be shown later, accurate control of the strike points is required to prevent the plasma baffles from exiting the divertor zone.

Assuming that the total plasma current  $I_p$  is positive, the flux monotonically decreases from the centre of the plasma towards the edge (Figure 3.3). It continues to decrease outside the plasma region and usually it increases again only outside the  $\mathcal{L}$  region; due to the presence of a saddle point, an exception to this behaviour is in the zone individuated by the X-point and the two strike points. If the total plasma current is negative, the flux function increases from the centre of the plasma (where the flux has a minimum) towards the plasma edge.

In all cases, the value  $\psi^B$  of the flux function at the plasma boundary can be determined by comparing the values of the flux along the first wall

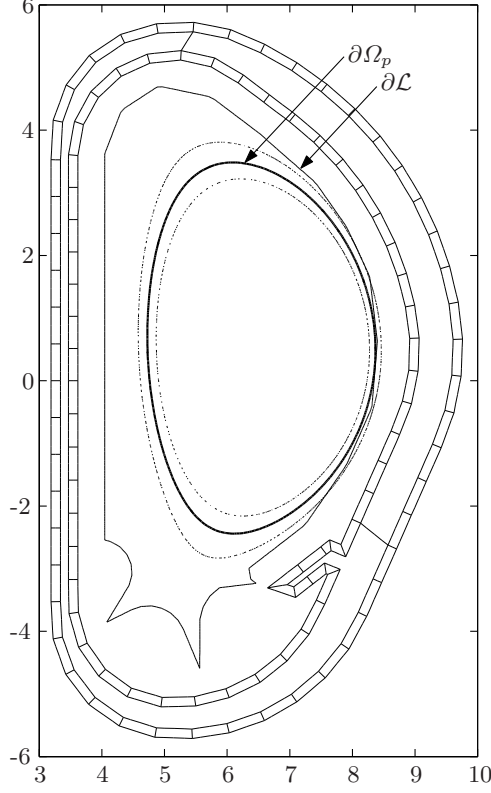


**Figure 3.1.** A limiter plasma. In the figure three closed level curves of the poloidal flux function are drawn. The middle thicker curve touches the first wall of the tokamak, therefore it represents the plasma boundary; the level curves immediately outside the plasma region cross the tokamak first wall.

and among the X-points. Denoting by  $\partial\tilde{\mathcal{L}}$  the part of the first wall where the plasma is allowed to touch, and with  $X_0$  the set of the X-points inside  $\mathcal{L}$ , one obtains

$$\psi^B = \begin{cases} \max_{\mathbf{r} \in \partial\tilde{\mathcal{L}} \cup X_0} \psi(\mathbf{r}), & \text{if } I_p > 0 \\ \min_{\mathbf{r} \in \partial\tilde{\mathcal{L}} \cup X_0} \psi(\mathbf{r}), & \text{if } I_p < 0. \end{cases} \quad (3.1)$$

Therefore, to determine the plasma boundary, it is sufficient to know the poloidal flux function only in the vacuum region  $\Omega_v$  (Figure 2.2).

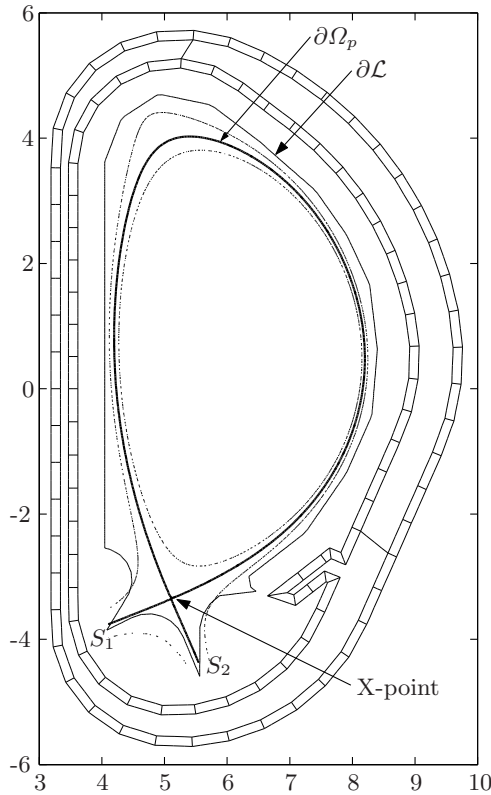


**Figure 3.2.** A divertor plasma. In the figure three level curves of the poloidal flux function are drawn. The middle thicker curve represents the plasma boundary; the level curves immediately outside the plasma region are opened, while the ones inside are closed. The plasma boundary in this case is the last closed curve which is inside the vacuum vessel region. From a topological point of view, the plasma boundary is characterized by the presence of an X-point, a point where the poloidal flux function has a saddle, or equivalently, the magnetic field is null.

### 3.2 The Plasma Boundary Descriptors

As a result of the discussion in Section 3.1 it should be clear that the plasma boundary is assigned once the poloidal flux function is known. As a matter of fact, the boundary is the closed curve on the poloidal plane satisfying the equation

$$\psi(\mathbf{r}) = \psi^B, \quad \mathbf{r} \in \mathcal{L}, \quad (3.2)$$

where  $\psi^B$  is defined in Equation 3.1.

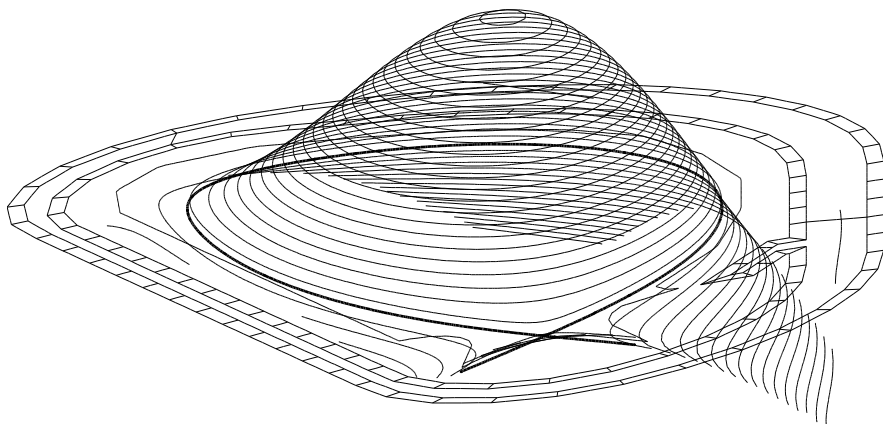


**Figure 3.3.** The poloidal flux function behaviour inside the plasma accessible region. Assuming a positive value for the total plasma current the flux monotonically decreases from the centre of the plasma towards the edge. The boundary flux value, determining the plasma boundary, is obtained comparing the flux value at the X-point with the maximum value of the flux along the first wall. In the figure the plasma boundary is represented by a thicker line.

Once the plasma boundary has been assigned, it is useful to define a certain finite number of parameters characterizing its shape and position in a concise way. The number and the type of these parameters depends on the particular characteristics of the shape that is required.

A first parameter used to give a rough evaluation of the plasma position is the plasma current centroid

$$r_c = \sqrt{\frac{1}{I_p} \int_{\Omega_p} r^2 J_\varphi \, dS} \quad (3.3a)$$

$$z_c = \frac{1}{I_p} \int_{\Omega_p} z J_\varphi \, dS. \quad (3.3b)$$

The plasma current centroid is the centre of the plasma current distribution; in particular  $z_c$  is used to characterize the plasma vertical position, whereas  $r_c$  is used to characterize the radial position.

Although the first tokamaks allowed only for plasmas having a circular cross-section, modern advanced machines usually operate with plasmas which have a vertically elongated D-shaped cross-section; this is important to assure better performance of the machine (later on, it will be shown that this makes the problem of controlling the plasma shape more complicated). Two parameters used to characterize how the plasma area is distributed on the poloidal plane are the elongation  $\kappa$  and the triangularity  $\delta$ .

With the aid of Figure 3.4, the following quantities can be defined:

$$R_{max} = \max_{(r,z) \in \partial\Omega_p} r \quad (\text{outer radius}) \quad (3.4a)$$

$$R_{min} = \min_{(r,z) \in \partial\Omega_p} r \quad (\text{inner radius}) \quad (3.4b)$$

$$Z_{top} = \max_{(r,z) \in \partial\Omega_p} z \quad (\text{maximum height}) \quad (3.4c)$$

$$Z_{bot} = \min_{(r,z) \in \partial\Omega_p} z \quad (\text{minimum height}) \quad (3.4d)$$

$$R = \frac{R_{max} + R_{min}}{2} \quad (\text{major radius}) \quad (3.4e)$$

$$a = \frac{R_{max} - R_{min}}{2} \quad (\text{minor radius}). \quad (3.4f)$$

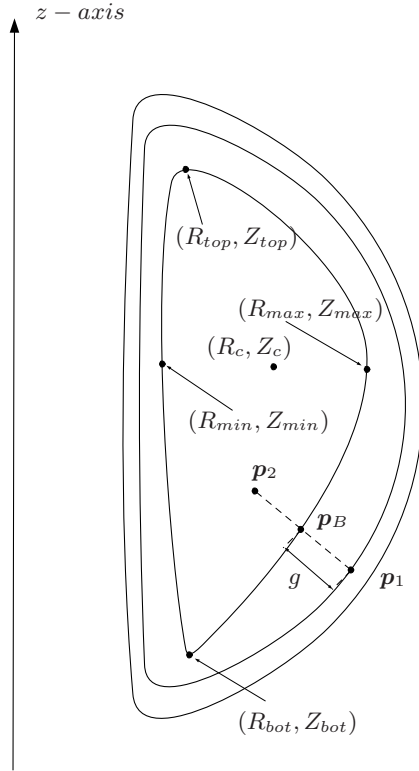


**Figure 3.4.** Geometrical descriptors of the plasma shape. The upper, the inner, the lower, the outer point, and a sample gap are shown; these parameters are used to define the plasma shape in a concise way.

From a practical point of view elongation and triangularity can be calculated as

$$\kappa = \frac{Z_{max} - Z_{min}}{R_{max} - R_{min}} \quad (3.5a)$$

$$\delta = \frac{2R - R_{top} - R_{bot}}{R_{max} - R_{min}}. \quad (3.5b)$$

Note that for a vertically elongated plasma,  $\kappa > 1$ .

The geometrical descriptors introduced in Equations 3.3, 3.4, and 3.5 globally characterize the position and the shape of the plasma. Taking into account the requirements of the plasma shape and position control system, it is often convenient to introduce other parameters characterizing local properties of the plasma boundary. Among these parameters there are the so called *gaps*. The gaps are the distances between selected points of the first wall and the plasma boundary, measured along given directions. Considering Figure 3.4 each gap  $g$  is determined by the intersection  $\mathbf{p}_B$  of the plasma boundary flux line with the segment connecting two point  $\mathbf{p}_1$  and  $\mathbf{p}_2$ . Therefore the gap  $g$  satisfies the implicit algebraic equation

$$\psi \left( \mathbf{p}_1 + \frac{\mathbf{p}_2 - \mathbf{p}_1}{\|\mathbf{p}_2 - \mathbf{p}_1\|} g \right) = \psi^B. \quad (3.6)$$

Other parameters of interest for control purposes are, for divertor plasmas, the position  $(r_x, z_x)$  of the X-point and the position of the two strike points  $S_1$  and  $S_2$  (Figure 3.2).

For the design of the plasma shape and position control system, it is important to know how the selected geometrical parameters change when the state and input variables of the linearized model (2.64) change. These geometrical descriptors can be evaluated once the poloidal flux is assigned. In Chapter 2 it has been shown that at each point the poloidal flux is a function of the vector  $x$ , representing the current flowing in the poloidal field coils and in the conducting structures of the tokamak, and of the vector  $w$ , representing the current distribution internal to the plasma. Therefore denoting with  $y$  the vector of these geometrical descriptors, it is possible to write

$$y = h(x, w). \quad (3.7)$$

Again the function  $h$  is not analytically known, but it is computed by equilibrium numerical codes as discussed in Chapter 2. In particular Equation 3.7 can be linearized in a neighbourhood of an equilibrium configuration giving rise to the linear equation

$$\delta y = C \delta x + F \delta w, \quad (3.8)$$

with  $C$  and  $F$  suitable matrices. For example, starting from Equation 3.6 it is simple to obtain for a gap



$$\delta g = \frac{\left( \left[ \frac{\partial}{\partial x} \psi^B \right]_0 - \left[ \frac{\partial}{\partial x} \psi \right]_0 \right) \delta x + \left( \left[ \frac{\partial}{\partial w} \psi^B \right]_0 - \left[ \frac{\partial}{\partial w} \psi \right]_0 \right) \delta w}{\left[ \frac{\partial}{\partial g} \psi \right]_0},$$

where as usual the subscript “0” refers to the value corresponding to equilibrium, and

$$\frac{\partial}{\partial g} \psi = \frac{\partial}{\partial \mathbf{r}} \psi \frac{\mathbf{p}_2 - \mathbf{p}_1}{\|\mathbf{p}_2 - \mathbf{p}_1\|}$$

is the derivative of the  $\psi$  function in the direction  $(\mathbf{p}_2 - \mathbf{p}_1)$ .

### 3.3 Tokamak Magnetic Diagnostics for Plasma Shape Identification

As seen in the previous section the plasma shape is characterized by a finite number of geometrical descriptors. As will be shown later on, these geometrical descriptors are the controlled variables of the plasma shape control loop. Unfortunately these parameters cannot be measured directly, and so they have to be estimated starting from the available measurements. At present in all existing tokamaks the geometrical descriptors are estimated starting from *magnetic measurements*.

Conceptually the magnetic sensors are very simple [52, 53]; usually they consist of an open coil whose voltage across the two terminals is measured by means of a differential amplifier. According to Lenz’s law (a direct consequence of Faraday’s law (2.3c)) this voltage is proportional to the time derivative of the total magnetic flux linked with the coil. Therefore by integrating this voltage, it is possible to obtain information about the magnetic field.

The most basic magnetic measurement device is the *flux loop*; this is a single open loop of wire, making a complete toroidal turn, and crossing the poloidal plane at a point  $\mathbf{r}$ . With reference to part (a) of Figure 3.5, the voltage  $V_l$  measured between the flux loop terminals can be written as

$$\begin{aligned} V_l &= -\frac{\partial}{\partial t} \int_{S(\mathbf{r})} \mathbf{B} \cdot d\mathbf{S} \\ &= -2\pi \frac{\partial}{\partial t} \psi(\mathbf{r}, t), \end{aligned}$$

or

$$\psi(\mathbf{r}, t) = -\frac{1}{2\pi} \int_{t_0}^t V_l(\sigma) d\sigma + \psi(\mathbf{r}, t_0). \quad (3.9)$$

Therefore a flux loop, cascaded with an integrator circuit, gives a measurement of the poloidal flux function at the point  $\mathbf{r}$ . Obviously this type of sensor has an offset term (the flux at the time the integration starts) that has to be taken into account.

*Saddle loops* are constructed by connecting two sectors of flux loops (see part (b) of Figure 3.5). In this way, again by integration of the voltage measured across the terminals, a value proportional to the poloidal flux difference between the points  $\mathbf{r}_1$  and  $\mathbf{r}_2$  can be obtained

$$V_s = -2\pi \frac{\partial}{\partial t} [\psi(\mathbf{r}_1, t) - \psi(\mathbf{r}_2, t)] ,$$

or

$$\psi(\mathbf{r}_1, t) - \psi(\mathbf{r}_2, t) = -\frac{1}{2\pi} \int_{t_0}^t V_s(\sigma) d\sigma + \psi(\mathbf{r}_1, t_0) - \psi(\mathbf{r}_2, t_0) . \quad (3.10)$$

A measure of the magnetic field can be obtained by using a so called *pick-up* coil. A pick-up coil consists of multiple windings of wire of small radius (see part (c) of Figure 3.5) located at a point  $\mathbf{r}$  of the poloidal plane; the flux linked with this solenoid is approximately equal to the component of the magnetic field parallel to the sensor axis, multiplied by the number  $N$  of turns and by the section  $A$  of the solenoid

$$V_b = -NA \frac{\partial}{\partial t} B_\theta(\mathbf{r}, t) ,$$

or

$$B_\theta(\mathbf{r}, t) = -\frac{1}{NA} \int_{t_0}^t V_b(\sigma) d\sigma + B_\theta(\mathbf{r}, t_0) , \quad (3.11)$$

where  $\theta$  is the angle the pick-up coil forms with the radial axis. Note that due to Equations 2.8 the pick-up coils also provide a measure of the spatial derivative of the flux function in the direction perpendicular to the sensor axis. Indeed putting together Equations 2.8 and Equation 3.11 gives

$$\begin{aligned} & \frac{\partial}{\partial r} \psi(\mathbf{r}, t) \cos\left(\theta + \frac{\pi}{2}\right) + \frac{\partial}{\partial z} \psi(\mathbf{r}, t) \sin\left(\theta + \frac{\pi}{2}\right) = \\ & -\frac{r}{NA} \int_{t_0}^t V_s(\sigma) d\sigma + \frac{\partial}{\partial r} \psi(\mathbf{r}, t_0) \cos\left(\theta + \frac{\pi}{2}\right) + \frac{\partial}{\partial z} \psi(\mathbf{r}, t_0) \sin\left(\theta + \frac{\pi}{2}\right) . \end{aligned} \quad (3.12)$$

The total plasma current, like the other currents flowing in the toroidal directions, can be measured by a *Rogowski* coil (see part (d) of Figure 3.5). A Rogowski coil is a multiple turn solenoid; for a uniformly wound wire, the flux linked with this solenoid is proportional to the line integral of the magnetic field along the solenoid axis (which is the one depicted in the figure), and hence by Ampere's law, to the net toroidal current  $I_T$  flowing in the region inside the coil. If  $d$  denotes the solenoid diameter, and  $M$  the number of turns per unit length, it is possible to show that

$$V_r(t) = -M \frac{\pi d^2}{4} \mu_0 \frac{d}{dt} I_T(t) ,$$

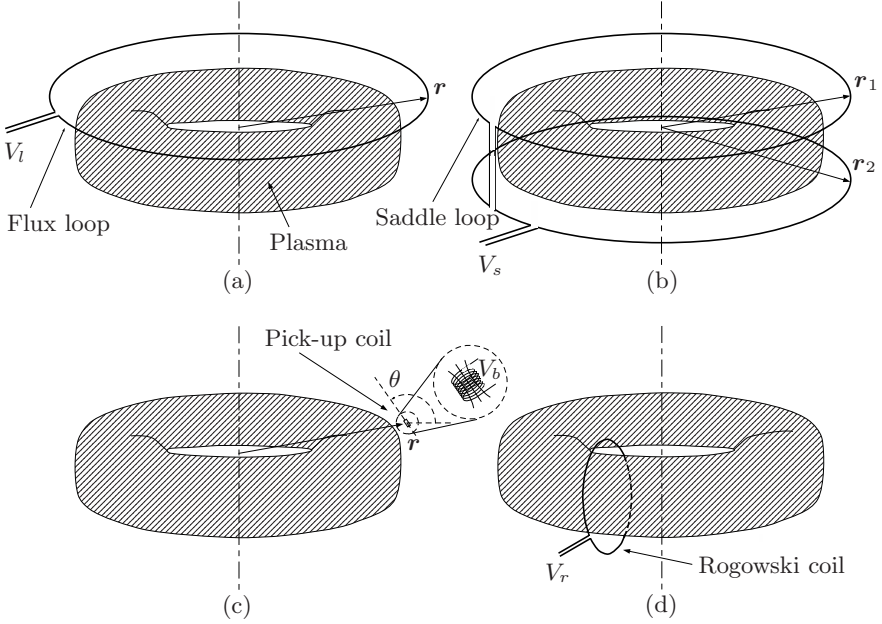


**Figure 3.5.** Typical magnetic sensors in a tokamak. All of these sensors operate on the principle that a flux change induces a voltage in a coil. This voltage is time integrated to determine the flux linked with the coil.

or

$$I_T(t) = -\frac{4}{Md^2\pi\mu_0} \int_{t_0}^t V_r(\sigma) d\sigma + I_T(t_0). \quad (3.13)$$

It is interesting to note that if the wire is not uniformly wound, it is possible to evaluate the line integral of the magnetic field weighted by a function varying along the coil; this fact in principle can be used to evaluate higher order moments of the plasma current distribution [54].

To simplify future discussions in this chapter, it is assumed that the diagnostic system, that is the whole set of magnetic sensors in the tokamak, is composed of  $m_l$  flux loops and  $m_b$  pick-up coils; saddle coils are not considered to simplify the notation, but their presence could easily be taken into account. Each flux loop is assumed to be located at the point  $\mathbf{r}_{l,i} = (r_{l,i}, z_{l,i})$  of the poloidal plane for  $i = 1, 2, \dots, m_l$ , while the pick-up coils are assumed to be placed at the points  $\mathbf{r}_{b,i} = (r_{b,i}, z_{b,i})$  for  $i = 1, 2, \dots, m_b$ . All these measurement devices will be assumed located on a closed contour  $\Gamma_m$  surrounding the plasma (Figure 3.6), with the pick-up coils oriented in the direction tangent to  $\Gamma_m$ ; in this way they provide a measure of the spatial derivative  $\partial\psi/\partial n$  of the poloidal flux function normal to  $\Gamma_m$ .

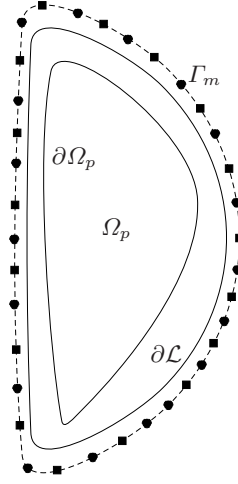


**Figure 3.6.** Definition of the plasma shape identification problem. The plasma shape is the boundary of the plasma region  $\Omega_p$ , and the problem is to determine this curve starting from the magnetic data available on the contour  $\Gamma_m$  surrounding the plasma accessible region  $\mathcal{L}$ . On  $\Gamma_m$  the bold circles represent flux loops measuring the poloidal flux, while the bold squares represent pick-up coil measuring the magnetic field in a given direction.

### 3.4 Plasma Shape Identification

Plasma shape estimation (the word identification is often used in the tokamak engineering literature) is based on the magnetic sensors which are available in the machine under consideration. As specified in the previous section, it is assumed that these sensors are placed along the closed contour  $\Gamma_m$  encircling the plasma (the measurement contour; Figure 3.6).

An important parameter for a plasma identification algorithm is its computational efficiency. Indeed, the geometrical descriptors have to be evaluated in a time which has to be smaller than the typical sampling frequency of the plasma shape controller (in the order of some microseconds). For this reason this section focuses on a fast identification algorithm which can easily be implemented in a real time system.

Since the knowledge of the function  $\psi$  in  $\Omega_v$  is sufficient to determine its last closed level line entirely contained in the vacuum vessel, the plasma shape identification is usually based on the following three steps:

1. determine an approximation to the poloidal flux function  $\psi$  in  $\Omega_v$  on the basis of the measurements;
2. determine the value of the poloidal flux function at the plasma boundary;

3. determine the set of the required plasma shape geometrical descriptors.

The last two points can easily be tackled once the first one has been executed. Indeed, once the flux function has been determined, it can be evaluated on a grid covering the plasma accessible area, and then simple search algorithms can be used to determine first the  $\psi$  value at the plasma boundary, and then the geometrical descriptors. Therefore in the remaining part of this section we will focus on the first problem.

In the region  $\Omega_v$  the function  $\psi$  satisfies the elliptic partial differential equation

$$\Delta^* \psi = 0, \quad (3.14)$$

which is called the homogeneous Grad–Shafranov equation.

The magnetic data from the sensors pose additional constraints on the poloidal flux function. Indeed, assuming that at a certain time instant each flux loop measures a value equal to  $f_{l,i}$  ( $i = 1, 2, \dots, m_l$ ), while each pick-up coil measures a value  $f_{b,i}$  ( $i = 1, 2, \dots, m_b$ ), then the poloidal flux function must satisfy the following boundary type conditions

$$\psi(\mathbf{r}_{l,i}) = f_{l,i} \quad i = 1, 2, \dots, m_l \quad (3.15a)$$

$$\frac{\partial}{\partial n} \psi(\mathbf{r}_{b,i}) = f_{b,i} \quad i = 1, 2, \dots, m_b. \quad (3.15b)$$

Note that, as can be seen comparing Equations 3.15 with Equations 3.9 and 3.12, the scalars  $f_{l,i}$  and  $f_{b,i}$  are corrected in such a way to contain all the scaling factors and the offsets related to a particular sensor.

Now the problem of determining the plasma boundary is equivalent to finding a function  $\psi$  solving Equation 3.14 in  $\Omega_v$  and simultaneously satisfying the conditions given by Equations 3.15. This problem does not have a unique solution, and so, as discussed in Section A.3, it is an *ill-posed* problem; therefore its solution requires the use of a regularization procedure.

The harmonic expansion method is a well known method to cope with ill-posed problems [55]. The first step consists in determining a complete basis  $\{\psi_k\}_{k \in \mathbb{N}}$  in the space  $\Psi$  of solutions to Equation 3.14 in  $\Omega_v$ . Now each possible solution  $\psi$  can be written as a generalized Fourier series

$$\psi = \sum_{k=1}^{\infty} c_k \psi_k, \quad (3.16)$$

where the scalars  $c_k$  are the Fourier coefficients, and each function  $\psi_k$ , called an eigenfunction, satisfies Equation 3.14. Following the arguments discussed in Section A.3, this series is truncated to the first  $m < m_l + m_b$  terms, in such a way to restrict the space of the possible solutions to a finite-dimensional subspace  $\tilde{\Psi} \subset \Psi$  of dimension  $m$ ; each candidate solution in  $\tilde{\Psi}$  can be written as

$$\tilde{\psi} = \sum_{k=1}^m c_k \psi_k. \quad (3.17)$$

Now letting

$$f = (f_{l,1} \ f_{l,2} \ \cdots \ f_{l,m_l} \ f_{b,1} \ f_{b,2} \ \cdots \ f_{b,m_b})^T \in \mathbb{R}^{m_l+m_b} \quad (3.18)$$

$$c = (c_1 \ c_2 \ \cdots \ c_m)^T \in \mathbb{R}^m, \quad (3.19)$$

and

$$A = \begin{pmatrix} \psi_1(\mathbf{r}_{l,1}) & \psi_2(\mathbf{r}_{l,1}) & \cdots & \psi_m(\mathbf{r}_{l,1}) \\ \psi_1(\mathbf{r}_{l,2}) & \psi_2(\mathbf{r}_{l,2}) & \cdots & \psi_m(\mathbf{r}_{l,2}) \\ \vdots & \vdots & \ddots & \vdots \\ \psi_1(\mathbf{r}_{l,m_l}) & \psi_2(\mathbf{r}_{l,m_l}) & \cdots & \psi_m(\mathbf{r}_{l,m_l}) \\ \frac{\partial}{\partial n} \psi_1(\mathbf{r}_{b,1}) & \frac{\partial}{\partial n} \psi_2(\mathbf{r}_{b,1}) & \cdots & \frac{\partial}{\partial n} \psi_m(\mathbf{r}_{b,1}) \\ \frac{\partial}{\partial n} \psi_1(\mathbf{r}_{b,2}) & \frac{\partial}{\partial n} \psi_2(\mathbf{r}_{b,2}) & \cdots & \frac{\partial}{\partial n} \psi_m(\mathbf{r}_{b,2}) \\ \vdots & \vdots & \ddots & \vdots \\ \frac{\partial}{\partial n} \psi_1(\mathbf{r}_{b,m_b}) & \frac{\partial}{\partial n} \psi_2(\mathbf{r}_{b,m_b}) & \cdots & \frac{\partial}{\partial n} \psi_m(\mathbf{r}_{b,m_b}) \end{pmatrix} \in \mathbb{R}^{(m_l+m_b) \times m}, \quad (3.20)$$

conditions (3.15) can be written in the algebraic form

$$Ac = f. \quad (3.21)$$

Assuming that the matrix  $A$  is left invertible (this is equivalent to assuming that the available measurements are independent), it follows that a unique solution inside the subspace  $\tilde{\Psi}$  can be found if the vector  $f$  is in the range of the matrix  $A$ . As a matter of fact, this is extremely improbable for two reasons: (i) it is not guaranteed that the true solution lies in  $\tilde{\Psi}$ ; (ii) the measurements are corrupted by unavoidable noise. In any case the solution of Equation 3.21 is obtained by choosing the vector  $c$  as

$$c^* = (A^T A)^{-1} A^T f = A^\dagger f, \quad (3.22)$$

that is, as the solution of the optimization problem

$$\min_{c \in \mathbb{R}^m} (Ac - f)^T (Ac - f). \quad (3.23)$$

As discussed in Section A.3 it is possible that the matrix  $A$  turns out to be ill conditioned, making evaluation of the pseudo-inversion in (3.22) unreliable; in this case it is possible to add to the objective function in (3.23) a so-called stabilizing functional [55].

### 3.5 An Algorithm for Plasma Shape Identification

In this section we outline a possible implementation of an algorithm for plasma shape identification based on the use of the toroidal harmonics and the Green's

functions as eigenfunctions in the Fourier expansion (3.16). For this algorithm numerical results will be provided showing the typical degree of accuracy that it is possible to obtain in real applications of these methods.

### 3.5.1 Choice of the Eigenfunctions for the Fourier Expansion

As seen in the previous section, in order to identify the plasma boundary, the poloidal flux is approximated by a truncated Fourier expansion whose coefficients are determined in such a way to fit the available magnetic measurements. The quality of this approximation is essentially linked to the choice of the eigenfunctions which appear in Equations 3.17; to obtain a good reconstruction of the poloidal flux function it is important to choose a basis in such a way that the eigenfunctions have some physical justification. From this point of view a good choice appears to be the use of the toroidal harmonics (Section A.2); indeed, each toroidal harmonic represents the flux produced by a given current multipole, hence in this case the actual toroidal current distribution is substituted with a certain number of current multipoles.

To make use of all the available information, it is convenient to exploit the linearity of the problem and to express the flux as the sum of two terms: the first corresponding to the flux produced by current sources inside the measurement contour; the second corresponding to the flux produced by current flowing externally to the measurement contour

$$\psi(\mathbf{r}) = \psi_{int}(\mathbf{r}) + \psi_{ext}(\mathbf{r}). \quad (3.24)$$

Assuming that the only current distribution inside the measurement contour is the one due to the plasma (the implication of this assumption will be discussed later), the term  $\psi_{int}$  is the flux  $\psi_p$  produced by the plasma current distribution, while  $\psi_{ext}$  represents the flux produced by the currents flowing in poloidal field coils and by the eddy currents flowing in the passive circuits.

The two functions in (3.24) can be separately approximated by truncated series

$$\psi_{int}(\mathbf{r}) = \sum_{k=0}^{N_{c,int}-1} a_{c,k} \psi_{int,k}^c(\mathbf{r}, \mathbf{r}_0) + \sum_{k=0}^{N_{s,int}-1} a_{s,k} \psi_{int,k}^s(\mathbf{r}, \mathbf{r}_0) \quad (3.25a)$$

$$\begin{aligned} \psi_{ext}(\mathbf{r}) = & \sum_{k=0}^{N_{c,ext}-1} b_{c,k} \psi_{ext,k}^c(\mathbf{r}, \mathbf{r}_0) + \sum_{k=0}^{N_{s,ext}-1} b_{s,k} \psi_{ext,k}^s(\mathbf{r}, \mathbf{r}_0) \\ & + \sum_{k=1}^{N_c} i_k G_0(\mathbf{r}, \mathbf{r}_{f,k}). \end{aligned} \quad (3.25b)$$

The functions  $\psi_{int,k}^c$ ,  $\psi_{int,k}^s$ ,  $\psi_{ext,k}^c$ , and  $\psi_{ext,k}^s$  are the toroidal harmonics defined in Section A.2, while  $G_0$  is the free space Green's function defined in Section A.1. The Green's functions summation in Equation 3.25b is inserted

to consider separately the contributions due to the currents flowing in the poloidal field coils. Indeed these currents are usually measured, and so it makes sense to place a toroidal current filament in the centre of each of the  $N_c$  poloidal field coils, and to let the coefficients  $i_k$  equal the measured currents. In this way a very good approximation of this contribution is obtained in the region  $\Omega_v$ : indeed, filamentary currents give a good approximation of a more complicate current distribution if the total current is the same, and if the region where the flux is evaluated is sufficiently far from the region where the current distribution and the filaments are located. Note that to simplify the notation in (3.25b), the presence of a single filament for each poloidal field coil has been considered; actually this can be a rough approximation if a coil is large or too close to the  $\Omega_v$  region, in this case instead of considering just one filament, it is possible to consider a number  $N$  of filaments and to assign a current of  $i_k/N$  to each of them.

For Equation 3.25b, apart from the term containing the contribution of the currents flowing in the poloidal field coils, which is assumed to be known, there is another term which is comprised of the sum of external toroidal harmonics; this term is equivalent, from a physical point of view, to a multipole current distribution centred in  $(0, z_0)$ , where  $z_0$  is the height of the point  $\mathbf{r}_0$ . This distribution is used to approximate the flux provided by other current sources not included in the first term; for example, it can be used to take into account some currents which are not measured, such as eddy currents in mechanical structures located outside the measurement contour, or to correct the error introduced by the representation of the poloidal field coils as filaments.

Summarizing, in the flux expansion given in Equations 3.25 the coefficients  $i_k$  of the Green's functions are directly measured; therefore the only unknown variables to be determined on the basis of the available measurements are the coefficients of toroidal harmonics  $a_{c,k}$ ,  $a_{s,k}$ ,  $b_{c,k}$ , and  $b_{s,k}$ . In the sequel, in accordance with the notation adopted in Section 3.4,  $c \in \mathbb{R}^m$ , where  $m = N_{c,int} + N_{s,int} + N_{c,ext} + N_{s,ext}$  is the total number of toroidal harmonics considered, will denote the vector of these unknown coefficients.

### 3.5.2 Choice of the Singular Point for the Toroidal Harmonics

As already said, the choice of using the toroidal harmonics in Equation 3.25a is equivalent, from a physical point of view, to substituting the continuous plasma current distribution with a multipole current distribution centred at the point  $\mathbf{r}_0$ . From a theoretical point of view, as long as  $\mathbf{r}_0$  is chosen inside the plasma region  $\Omega_p$ , and the number of eigenfunctions is sufficiently large, the flux distribution obtained by Equation 3.25a should not be dependent on the particular choice of  $\mathbf{r}_0$ . Actually, because of the limited number of measurements available, and in order to reduce the computational burden of the shape identification algorithms, the number of eigenfunctions cannot be chosen too large; as matter of fact this implies that an accurate choice of  $\mathbf{r}_0$  is necessary.



Before discussing the way  $\mathbf{r}_0$  can be chosen, it is necessary to introduce some notation. Let  $e(\mathbf{r}, \mathbf{r}_0) \in \mathbb{R}^m$  be the vector having as components the chosen toroidal harmonics evaluated in  $\mathbf{r}$ ,  $g(\mathbf{r})$  the vector of the free space Green's functions considered in Equation 3.25b, and  $i_f \in \mathbb{R}^{N_c}$  the vector of the coefficients of these Green's functions. Equation 3.24 can be written in vectorial form as

$$\psi(\mathbf{r}) = e^T(\mathbf{r}, \mathbf{r}_0)c + g_0^T(\mathbf{r})i_f. \quad (3.26)$$

Moreover let

$$\Psi(\mathbf{r}_0) = \begin{pmatrix} e^T(\mathbf{r}_{l,1}, \mathbf{r}_0) \\ e^T(\mathbf{r}_{l,2}, \mathbf{r}_0) \\ \vdots \\ e^T(\mathbf{r}_{l,m_l}, \mathbf{r}_0) \\ \frac{\partial}{\partial n} e^T(\mathbf{r}_{b,1}, \mathbf{r}_0) \\ \frac{\partial}{\partial n} e^T(\mathbf{r}_{b,2}, \mathbf{r}_0) \\ \vdots \\ \frac{\partial}{\partial n} e^T(\mathbf{r}_{b,m_b}, \mathbf{r}_0) \end{pmatrix} \in \mathbb{R}^{(m_l+m_b) \times N_t} \quad (3.27)$$

$$G = \begin{pmatrix} g^T(\mathbf{r}_{l,1}) \\ g^T(\mathbf{r}_{l,2}) \\ \vdots \\ g^T(\mathbf{r}_{l,N_f}) \\ \frac{\partial}{\partial n} g^T(\mathbf{r}_{b,1}) \\ \frac{\partial}{\partial n} g^T(\mathbf{r}_{b,2}) \\ \vdots \\ \frac{\partial}{\partial n} g^T(\mathbf{r}_{b,m_b}) \end{pmatrix} \in \mathbb{R}^{(m_l+m_b) \times N_f} \quad (3.28)$$

$$f_p = f - Gi_f. \quad (3.29)$$

The matrices  $\Psi$  and  $G$  describe the effects of the toroidal harmonics and the filaments, respectively, at the measurement points. The vector  $f_p$  represents the measurement vector where the contribution given by the poloidal field coil has been subtracted.

In principle  $\mathbf{r}_0$  could be chosen to best fit the available measurements; this can be obtained by solving the optimization problem

$$\min_{\mathbf{r}_0 \in \mathcal{L}} \left[ \min_{c \in \mathbb{R}^{N_t}} (\Psi(\mathbf{r}_0)c - f_p)^T (\Psi(\mathbf{r}_0)c - f_p) \right] = \min_{\mathbf{r}_0 \in \mathcal{L}} (\Psi(\mathbf{r}_0)\Psi(\mathbf{r}_0)^\dagger f_p - f_p)^T (\Psi(\mathbf{r}_0)\Psi(\mathbf{r}_0)^\dagger f_p - f_p). \quad (3.30)$$

Unfortunately it is not possible to solve this problem analytically, while numerical approaches are very demanding from a computational point of view, since they require evaluation of the matrix  $\Psi$  and of its pseudo-inverse at each evaluation of the objective function (3.30) (see [56]).

Alternatively a more efficient method giving a suboptimal solution, and leading to a substantial reduction of the computational burden can be used [57]. This method is based on the fact that the optimal solution of problem (3.30) is typically very close to the plasma current centroid, whose position is defined by Equations 2.48.

Therefore as a near-optimal solution to problem (3.30), it has been proposed to choose the position of the plasma current centroid, which can be obtained starting from the magnetic measurements. For example in [58] the authors evaluate the current centroid by substituting the plasma with a small number  $\mu$  of filaments. These filaments are used to approximate the effect of the plasma current distribution on the magnetic measurements; hence each of them is assumed to carry a certain amount of current. Denoting with  $M_{fp}$  the matrix whose  $ij$ -element gives the contribution to the measurement  $i$  of a unitary current in the filament  $j$ , the first step consists in determining the vector  $i_{p,f}$  of the elementary currents best fitting the measurements

$$i_{p,f} = M_{fp}^\dagger f_p.$$

Once the vector  $i_{p,f}$  has been evaluated, then the position of the centroid (and of the singular point of the toroidal harmonics) can be evaluated as

$$r_0 = \sqrt{\frac{\sum_{k=1}^{\mu} i_{p,f_k} r_{p,f_k}^2}{\sum_{k=1}^{\mu} i_{p,f_k}}} \quad (3.31)$$

$$z_0 = \frac{\sum_{k=1}^{\mu} i_{p,f_k} z_{p,f_k}}{\sum_{k=1}^{\mu} i_{p,f_k}}, \quad (3.32)$$

where  $(r_{p,f_k}, z_{p,f_k})$  and  $i_{p,f_k}$  are the position and the current of the filament  $k$ ,  $k = 1, 2, \dots, \mu$ , respectively.

The idea of substituting the plasma with a set of filaments, and of evaluating the currents in these filaments by fitting the measurements, has also been

used to directly identify the plasma boundary (see, for example, [59, 60]); the technique is similar to the one described here with the difference that the toroidal harmonics in Equation 3.25 are substituted by Green's functions.

### 3.5.3 Numerical Results

The plasma shape identification algorithm previously described is used here for the identification of the plasma separatrix in ITER equilibrium conditions (Chapter 7). In particular the algorithm is tested reconstructing the plasma shape at the Start of Flat-Top (SOF) equilibrium. For this reconstruction it is assumed that the currents flowing in all the poloidal field coils and in the central solenoid coils are known, moreover the algorithm uses the data from 48 pick-up coils and 21 flux loops. The position of these magnetic sensors is shown in Figure 3.7. The magnetic flux produced by the poloidal field coils, and by the central solenoid coils is approximated using 12 current filament located at the centre of each coil (Figure 3.7). Eleven toroidal harmonics are used to approximate the remaining part of the flux function, these are

1. the 0th order, internal,  $\psi_{\text{int},0}^c$ ;
2. the 0th order, external,  $\psi_{\text{ext},0}^c$ ;
3. the 1st order, internal, symmetrical,  $\psi_{\text{int},1}^c$ ;
4. the 1st order, internal, anti-symmetrical,  $\psi_{\text{int},1}^s$ ;
5. the 2nd order, internal, symmetrical,  $\psi_{\text{int},2}^c$ ;
6. the 2nd order, internal, anti-symmetrical,  $\psi_{\text{int},2}^s$ ;
7. the 2nd order, external, anti-symmetrical,  $\psi_{\text{ext},2}^s$ ;
8. the 3rd order, internal, symmetrical,  $\psi_{\text{int},3}^c$ ;
9. the 4th order, internal, symmetrical,  $\psi_{\text{int},4}^c$ ;
10. the 5th order, internal, symmetrical,  $\psi_{\text{int},5}^c$ ;
11. the 5th order, external, symmetrical,  $\psi_{\text{ext},5}^c$ .

Figure 3.7 compares the identified and the actual plasma separatrix, the error in the reconstruction is in the order of some centimetres on the overall shape, but it is less than 1 cm in the gaps used to characterize the plasma shape (and for which the algorithm has been optimized). The performance of plasma shape identification algorithms obviously decrease in real situations in the presence of the unavoidable noise on the measurements; nevertheless this type of algorithm has been shown to be sufficiently robust also when measurement noise is considered.

## 3.6 Taking into Account the Eddy Currents

One of the weaknesses of the methodology described in the previous section is that it does not take into account the eddy currents flowing in the passive structures; in particular those which flow in the conducting structure that are inside the measurement contour. These currents generate a magnetic field

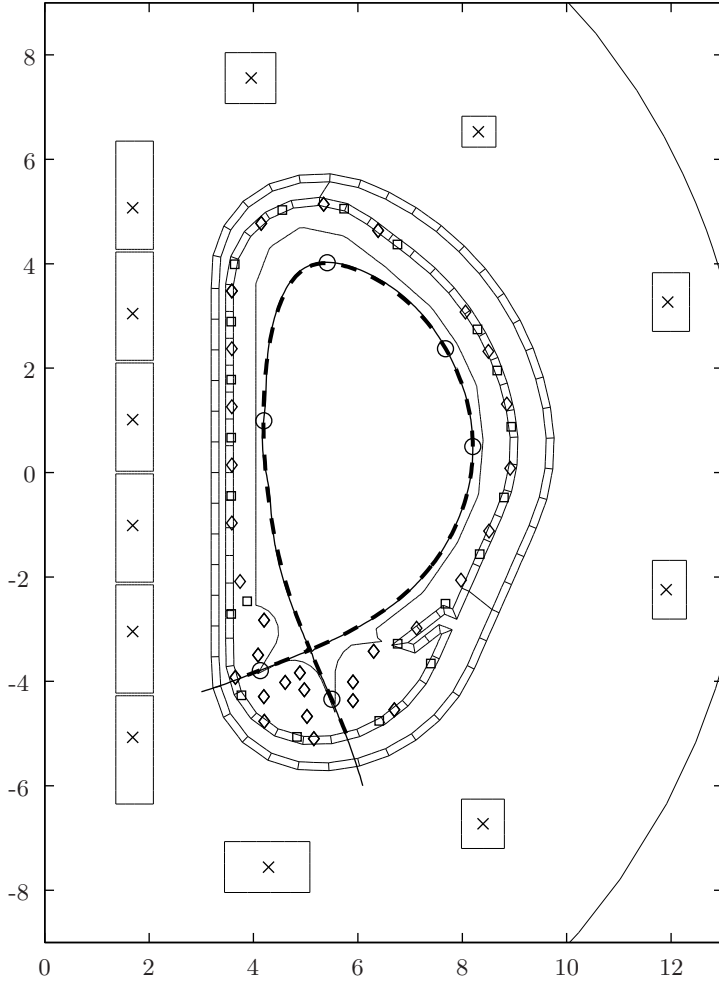


**Figure 3.7.** An application of the plasma shape algorithm to the ITER tokamak. The thicker dotted line represent the actual plasma shape, while the solid line is the identified one. The crosses represent the position of the filaments used to model the poloidal field coils, while the diamonds and squares represent the position of the magnetic field and poloidal flux sensors, respectively; finally the circles represent the position on the actual shape of the identified gaps.

which affects the measurements and hence affects the plasma shape identification procedure. This is particularly true during the transients when these currents can be non-negligible.

The eddy currents are not directly measurable; if they were known, it could be possible to subtract their contribution to the measurements; in this way the identification procedure would not be affected.

In this section we briefly review a method to deal with these currents, which is based on the use of a dynamic observer [61]. The observer is designed based on the finite-dimensional linear model presented in Section 2.5. This model describes the dynamics of the currents in the conducting structures and has the form (2.55)

$$L_c \dot{\tilde{x}} + R_c \tilde{x} + \dot{\Psi}_p = B_c u, \quad (3.33)$$

where  $\tilde{x}$  is the state vector having as components the active coil and eddy currents,  $u$  is the vector of the voltages applied to the active coils, and  $\Psi_p$  is a vector representing the flux produced by the plasma.

Concerning the measurements, they are the same as used in the previous sections to identify the plasma shape. Since they are linear combinations of  $\tilde{x}$  and  $\Psi_p$ , it is possible to write

$$f = C\tilde{x} + D\Psi_p + Wn, \quad (3.34)$$

where the term  $Wn$  represents the measurement noise.

Starting from Equations 3.33 and 3.34, it is possible to design an observer for the state variable  $\tilde{x}$ . Since the vectors  $\dot{\Psi}_p$ ,  $\Psi_p$ , and  $n$  are unknown, they represent disturbance inputs, whose action must be rejected by a suitable choice of the observer gain. The effectiveness of this approach has been tested against experimental data of the ASDEX-UP tokamak [58, 62] by designing an observer based on the  $H_2/H_\infty$  theory [63, 64].

## Part II

---

### Plasma Control

---

## Plasma Magnetic Control Problem

In the previous chapters we have shown how it is possible to derive a FDLTI (finite-dimension linear time-invariant) model able to describe the interactions between the plasma and the surrounding structures, in terms of specified inputs and outputs, under certain simplifying assumptions.

In this part of the book, we will focus mainly on the problem of controlling the plasma current, position and shape by means of the magnetic field produced by the poloidal field coils. Our problem will be to find a set of coil currents which generate a magnetic field which enables tracking a desired behaviour in terms of plasma position and shape.

As already discussed in Chapter 1, tokamaks are pulsed machines; a plasma discharge can be roughly divided into four different phases (Figure 1.6).

1. *Breakdown*. During this phase, the plasma is formed: the hydrogen gas in the vacuum vessel is ionized. The conditions for breakdown are in general difficult to achieve; usually some empirical “recipes”, depending on the plasma required, are used.
2. *Ramp-up*. During this phase, the plasma current, which is initially zero, reaches its desired steady-state value. Usually during this phase the plasma current follows a linear or piecewise linear ramp. Also the other quantities which characterize the plasma reach their desired values. The current ramp-up cannot be too fast, which would be energetically convenient, otherwise disruptive instabilities arise [65].
3. *Flat-top*. During this phase, all the quantities which characterize the plasma should remain as constant as possible. This is the most important, and longest phase, during which the production of energy should occur. Therefore the control requirements are very stringent.
4. *Ramp-down*. The plasma current and all other quantities are driven to zero. The plasma is extinguished.

Our interest will be the flat-top phase. During this phase the plasma behaviour can be approximated with a linear time-invariant model (Chapter 2). To use in the best possible way the parts of the chamber with high magnetic

toroidal field, tokamaks have an elongated poloidal section. In this way, using the same volume, the plasma is as close as possible to the coils which induce the field. On the other hand, elongation of the plasma cross-section causes the plasma vertical position to be unstable. Therefore the use of feedback for position control is mandatory.

Different kinds of instabilities can arise in a plasma: local, global, tridimensional, axisymmetric [66]. The one we analyse here, the global axisymmetric, is the most dangerous. The feedback action is performed by varying the current in the poloidal field coils. These currents are the sum of some preprogrammed currents and a feedback part. The preprogrammed currents are calculated based on the plasma geometrical shape which is to be achieved. Feedback control in this phase is very critical since, as we will see, the plasma current and shape (the plasma-to-wall distance) need to be continuously adjusted and disturbances that can occur must be rejected within a prescribed time.

The other phases of the discharge are less critical for the feedback control system. In particular:

- no feedback action is required during breakdown;
- during the ramp-up phase the plasma is limited and with an almost circular cross-section. No instability is present; it is therefore sufficient to control in feedback two parameters: the plasma current magnitude and the radial position of the plasma in the vessel;
- during ramp-down the plasma gradually reduces its volume until it extinguishes. This termination phase is carried out using simple feedback algorithms, which are mainly aimed at controlling the plasma current magnitude.

## 4.1 Model for Controller Design

The model of the plant that we will use for the magnetic control problem is given by the following equations (Section 2.5)

$$L^* \delta \dot{x} + R \delta x + E \delta \dot{w} = B \delta u \quad (4.1a)$$

$$\delta y = C \delta x + F \delta w. \quad (4.1b)$$

In Equations 4.1:

- $x$  is the vector of the currents in the active and passive circuits and of the plasma current; the active currents are the current flowing in the poloidal field coils;
- $w$  is the vector containing the two parameters  $l_i$  and  $\beta_p$ , which are related to the plasma current; in this model they act as disturbances, since they cannot be manipulated;
- $u$  are the inputs to the model, that is the voltages applied to the various poloidal field circuits;



- $y$  denotes the outputs, which depend on the specific tokamak, in particular on its diagnostic system.

We recall that by  $\delta$  we indicate variations in the quantities with respect to the nominal values, since the model (4.1) is obtained through linearization.

Separating the active currents (denoted by  $x_a$ ) from the passive (*eddy*) currents (denoted by  $x_e$ ) and from the plasma current (denoted by  $I_p$ ), Equations 4.1a can be rewritten as

$$\begin{pmatrix} L_a^* & L_{ae}^* & L_{ap}^* \\ L_{ea}^* & L_e^* & L_{ep}^* \\ L_{pa}^* & L_{pe}^* & L_p^* \end{pmatrix} \begin{pmatrix} \delta \dot{x}_a \\ \delta \dot{x}_e \\ \delta \dot{I}_p \end{pmatrix} + \begin{pmatrix} R_a & 0 & 0 \\ 0 & R_e & 0 \\ 0 & 0 & R_p \end{pmatrix} \begin{pmatrix} \delta x_a \\ \delta x_e \\ \delta I_p \end{pmatrix} + \begin{pmatrix} E_a \\ E_e \\ E_p \end{pmatrix} \delta \dot{w} = \begin{pmatrix} I \\ 0 \\ 0 \end{pmatrix} \delta u \quad (4.2a)$$

$$\delta y = C \begin{pmatrix} \delta x_a \\ \delta x_e \\ \delta I_p \end{pmatrix} + F \delta w. \quad (4.2b)$$

Usually, in the design of the plasma shape and current controller, the eddy currents are neglected. Under this assumption, Equation 4.2a reduces to

$$\begin{pmatrix} L_a^* & L_{ap}^* \\ L_{pa}^* & L_p^* \end{pmatrix} \begin{pmatrix} \delta \dot{x}_a \\ \delta \dot{I}_p \end{pmatrix} + \begin{pmatrix} R_a & 0 \\ 0 & R_p \end{pmatrix} \begin{pmatrix} \delta x_a \\ \delta I_p \end{pmatrix} + \begin{pmatrix} E_a \\ E_p \end{pmatrix} \delta \dot{w} = \begin{pmatrix} I \\ 0 \end{pmatrix} \delta u. \quad (4.3)$$

The ratio  $L_p^*/R_p$ , which is the time constant of the circuit representing the plasma ring, is typically large compared with the duration of a discharge, due to the fact that the plasma resistance is almost negligible. On the other hand, it is very difficult to estimate the plasma resistance since it depends on the conditions of the experiment; moreover, typically it also changes during a single experiment, since it is related to the plasma temperature, which is affected by the additional heating devices. As a consequence, the choice that is typically made is to let  $R_p = 0$ . Neglecting  $R_p$ , the final equation in (4.3) becomes

$$L_{pa}^* \delta \dot{x}_a + L_p^* \delta \dot{I}_p + E_p \delta \dot{w} = 0. \quad (4.4)$$

Moreover, in the controller design procedure, the vector  $\delta w$  is ignored since it acts as a disturbance. As a consequence, Equation 4.4 reduces to

$$L_{pa}^* \delta \dot{x}_a + L_p^* \delta \dot{I}_p = 0. \quad (4.5)$$

Making use of Equation 4.5, the plasma current  $I_p$  can be expressed as a linear combination of the active current and hence eliminated from the state equation. In this way the plasma model for the controller design becomes

$$\left( L_a^* - \frac{L_{ap}^* L_{pa}^*}{L_p^*} \right) \delta \dot{x}_a + R_a \delta x_a = \delta u \quad (4.6a)$$

$$\begin{pmatrix} \delta y \\ \delta I_p \end{pmatrix} = \begin{pmatrix} C \\ -L_{pa}^*/L_p^* \end{pmatrix} \delta x_a. \quad (4.6b)$$

The model (4.6) can easily be put in the standard state-space form

$$\delta \dot{x}_a = - \left( L_a^* - \frac{L_{ap}^* L_{pa}^*}{L_p^*} \right)^{-1} R_a \delta x_a + \left( L_a^* - \frac{L_{ap}^* L_{pa}^*}{L_p^*} \right)^{-1} \delta u \quad (4.7a)$$

$$\begin{pmatrix} \delta y \\ \delta I_p \end{pmatrix} = \begin{pmatrix} C \\ -L_{pa}^*/L_p^* \end{pmatrix} \delta x_a. \quad (4.7b)$$

#### 4.1.1 Simulation Model

The model (4.7) is used only for the purposes of controller design. After the design, the controller performance needs to be assessed using a more detailed plant model. Typically the simulation model includes:

- the model (4.1) which describes the interactions between the plasma and the surrounding structures. To eliminate the presence of the disturbance time derivative  $\delta \dot{w}$  in (4.1a), the following change of variables can be adopted

$$\delta \xi = L^* \delta x + E \delta w.$$

In this way, the model (4.1) can be rewritten in the standard state-space form

$$\delta \dot{\xi} = \tilde{A} \delta \xi + \tilde{B} \delta u + \tilde{W} \delta w \quad (4.8a)$$

$$\delta y = \tilde{C} \delta \xi + \tilde{F} \delta w, \quad (4.8b)$$

where

$$\tilde{A} = -RL^{*-1}$$

$$\tilde{B} = B$$

$$\tilde{W} = -RL^{*-1}E$$

$$\tilde{C} = C$$

$$\tilde{F} = F - CL^{*-1}E$$

- a model of the power supplies; the models used for this task are typically first-order filters plus a pure time delay;
- a model for the diagnostic system; this system is typically approximated by means of a first-order filter.

## 4.2 Requirements for the Controller Design

The basic control problem consists in controlling the overall plasma shape during the flat-top phase of a discharge. Indeed during this phase, to make the best use of the available volume and to ensure good passive stabilization

in large, highly elongated tokamaks, the plasma must be maintained as close as possible to nearby components such as the first wall, limiter, and baffles. The approach which is typically pursued is the so-called gap control approach.

In the next section we present a method for a suitable choice of the gaps to be controlled. Next, we discuss the typical requirements and constraints that need to be taken into account for the controller design.

#### 4.2.1 Gap Control Approach

To obtain better performance during the flat-top phase, a finite number of distances (the gaps defined in Section 3.2) between the first wall and the plasma boundary are used as controlled shape geometrical descriptors. These gaps have to be chosen to provide a synthetic characterization of the plasma shape.

What we want to have is the best possible control of the overall plasma shape. The main problem becomes then how to choose the “optimal” location of the gaps. In this section we describe a procedure that can be adopted for tackling this problem.

To begin with (see also Chapter 3), let us define the first wall contour  $\partial\mathcal{L}$  as a closed line in the poloidal plane  $(r, z)$  that encloses the plasma poloidal cross-section  $\Omega_p$ . The plasma boundary is the curve  $\partial\Omega_p$ , and it can be described by the function  $d(\cdot)$  which, at each point  $\mathbf{r}$  of the first wall contour  $\partial\mathcal{L}$ , gives the distance  $d(\mathbf{r})$  measured along the normal to  $\partial\mathcal{L}$ , between  $\partial\Omega_p$  and  $\partial\mathcal{L}$ . At each point  $\mathbf{r}$ ,  $d(\mathbf{r})$  defines a gap. Then we consider a set of points along  $\partial\mathcal{L}$  denoted by  $S_c$  (controlled points); these points define the gaps to be controlled. Our aim here is to define the criteria to choose the points in  $S_c$  and their number  $n_c$ .

Let us define the function  $\delta g(\mathbf{r}) = d(\mathbf{r}) - d_0(\mathbf{r})$ , where  $d_0(\mathbf{r})$  gives the distance between  $\partial\Omega_p$  and  $\partial\mathcal{L}$  for the nominal equilibrium configuration. To have a quantitative measure of the boundary displacement, we use two different indicators. The first one is the root mean square  $\bar{g}$  of the function  $\delta g$ , it is defined as

$$\bar{g}^2 = \frac{\oint_{\partial\mathcal{L}} \delta g^2 dl}{\oint_{\partial\mathcal{L}} dl}.$$

The other indicator we consider is the maximum plasma boundary displacement along  $\partial\mathcal{L}$

$$g_m = \max_{\mathbf{r} \in \partial\mathcal{L}} |\delta g(\mathbf{r})|.$$

Our choice of the set  $S_c$  is made under the following assumptions:

- a disturbance  $\delta w$  is applied to the plasma; this disturbance is chosen to be representative of a worst case perturbation to the plasma in the normal operations. We assume that this worst case disturbance is schematized as

an instantaneous drop of both  $\beta_p$  and  $l_i$ ; the amplitude of these drops depends both on the tokamak under consideration and on the plasma configuration;

- a feedback controller stabilizes the plasma and performs an integral action guaranteeing zero steady-state errors on the plasma current and on the controlled gaps.

The problem is that of finding a suitable set of controlled gaps that keeps the steady-state control current  $\delta x_a(t \rightarrow +\infty)$  “small” while providing “good” overall control of the plasma shape. To achieve this objective and to characterize what small and good mean, we perform a steady-state analysis. From Equation 4.2a, it is simple to see that at steady-state the eddy currents vanish. As a consequence at steady-state, we have

$$\delta g(\mathbf{r}) = C_g(\mathbf{r}) \delta x_a + F_g(\mathbf{r}) \delta w \quad (4.9a)$$

$$\delta g_c = C_c \delta x_a + F_c \delta w = 0, \quad (4.9b)$$

where  $g_c$  is the vector of the displacements evaluated in the controlled points of  $S_c$ , and  $C_c$  and  $F_c$  are suitable matrices. Note that Equation 4.9 can be satisfied only if the number of active coils is greater than or equal to the number of controlled variables; hence an upper limit on  $n_c$  is given. In order to obtain better accuracy in the control of the plasma shape, it is desirable to increase  $n_c$  as much as possible; unfortunately increasing  $n_c$  leads to a large number of constraints for the active coil currents to satisfy in Equation 4.9b and hence, in general, to larger values of these currents.

To find a reasonable trade-off, for each possible realization of the set  $S_c$ , it is possible to introduce the following steady-state performance indicators

$$\hat{x}_a = \arg \min_{x_a} \bar{g}, \quad \text{subject to } g_c = 0$$

$$\tilde{x}_a = \arg \min_{x_a} x_a^T x_a, \quad \text{subject to } g_c = 0$$

$$\hat{g}_2 = \bar{g}|_{x_a=\hat{x}_a}$$

$$\hat{g}_m = g_m|_{x_a=\hat{x}_a}$$

$$\tilde{g}_2 = \bar{g}|_{x_a=\tilde{x}_a}$$

$$\tilde{g}_m = g_m|_{x_a=\tilde{x}_a}.$$

Hence  $\hat{x}_a$  gives the steady-state currents which guarantee minimum variation (in the least square sense) of the plasma shape,  $\tilde{x}_a$  gives the minimum norm steady-state currents, the other parameters give a measure of the plasma shape variation corresponding to the two previous set of currents.

Since it is reasonable that the feedback control system operates to assure a trade-off between accuracy and control effort, the set  $S_c$  can be chosen by solving the optimization problem

$$\min_{S_c \subseteq \partial \mathcal{L}} \frac{1}{2}(\hat{g}_2 + \tilde{g}_2), \quad \text{subject to}$$

$$\frac{1}{2}(\|\tilde{x}_a\|_2 + \|\hat{x}_a\|_2) \leq I_{\max}, \quad \frac{1}{2}(\hat{g}_m + \tilde{g}_m) \leq D_{\max} \quad (4.10)$$

where the two constraints are included to limit the steady-state active currents, and the maximum plasma boundary offset. Since  $S_c$  is a discrete set with a bounded number of elements, this optimization problem can be easily solved by first discretizing the set  $\partial \mathcal{L}$ , and then evaluating the objective function for all possible realization of  $S_c$ . The algorithm for the choice of the controlled gaps described in this section has been applied, for instance, to the ITER tokamak in [67].

Once the gaps have been chosen, then the problem becomes how to evaluate them starting from the available measurements; indeed we recall that the gaps are not directly accessible. This inverse problem is discussed in detail in Chapter 3. From the control system design point of view it is important to take into account the presence of the plasma shape identification algorithm mainly because it introduces a computational delay in the control loop. A typical way of schematizing this delay is by introducing a first-order linear filter at the output of the plasma models used for the design and for the simulation.

In the proposed approach, the maximum number of controlled gaps is limited by the number of PF coils. The number of PF coils is typically ten or less; as a consequence using this method we can choose only a few gaps.

Recently it has been observed that when only a few gaps are controlled, even with accurate control of these gaps, the plasma shape undergoes unacceptable variations in the presence of disturbances; this is especially true when high elongated plasmas are considered. If this happens, then we need to increase the number of controlled gaps. The case when we have more controlled gaps than control inputs is discussed in Chapter 9, where a possible solution for the JET tokamak is presented.

#### 4.2.2 Typical Requirements and Constraints

The driving constraint for the control design is the robust stabilization of the plasma. Moreover, the controller must be able to control the reference gaps in the presence of some specified disturbances with prescribed performance.

A list of possible disturbances has been compiled based on empirical considerations from existing tokamaks. In the presence of such perturbations, the controller should be able to recover the original plasma shape in a prescribed time interval with a maximum gap displacement at steady-state of a few centimetres. Both the value of the desired settling time and the value of the maximum acceptable gap displacement strongly depend on the machine considered; the desired settling times can range from 0.1 s (see the case of the shape control in TCV in Chapter 8) to 15 s (this is the case of ITER, treated in Chapter 7). Moreover during the transients the plasma should avoid touching the first wall and the divertor septum.

The control of the plasma shape cannot resort to unlimited *ideal* resources. The main limitations are typically the currents available for control purposes. Indeed, certain values of the currents in the active circuits are needed to achieve a given plasma configuration. In order to lower the costs, the coils are designed to keep the maximum tolerable values of currents and voltages as low as possible. For this reason, typically the ranges of values for the control currents are rather limited. Analogously, also the voltages in the circuits cannot typically have large variations. Moreover in some cases, due to the schematics of the power supplies, the currents and/or the voltages in the circuits cannot change their sign, and this of course poses further limitations.

In large tokamaks, where significant amounts of power are needed, another limitation is set by the maximum (*peak*) power that can be used by the feedback control system and by the maximum time derivative of the power. These power limits are highly significant especially during the transient phases when the control system is required to counteract disturbances that modify the plasma shape; as a consequence, the maximum control system bandwidth cannot exceed a certain value.

### 4.3 Plasma Vertical Stabilization Problem

For elongated plasmas, *e.g.*, plasma with elongation (Section 3.2) larger than 1, one of the most important features of the model (4.7) is the presence of an unstable mode. The free evolution along this unstable mode gives rise to a vertical movement of the plasma ring; for this reason it is usually said that the plasma is *vertically unstable*. The observation of this instability by physicists justified the necessity for at least one feedback loop in any tokamak operating with elongated plasmas. The first vertical controllers were designed by non-specialists; moreover only very simplified models were available. Therefore, typically, SISO (single-input–single-output) PID were used, where the controller gains were tuned experimentally. This procedure requires, as can be imagined, a lot of experimental time to optimize the gains.

Typically the plasma magnetic control problem on almost all existing machines, even with the use of MIMO (multiple-input–multiple-output) “sophisticated” controllers, is carried out in two steps.

1. First the plasma is vertically stabilized; the controller is designed on the basis of the model (4.7) once the proper inputs and outputs are selected. Often the model reduces to a SISO model, having as input the voltage to apply to the circuit used for vertical stabilization, and as output the time derivative of the vertical position of the plasma current centroid  $z_c$  (Equation 2.48b). The technique that is used for the design is the one that is considered the most effective for the specific tokamak; in particular, critical points for the design are the maximum voltages, currents and power available to the vertical controller.

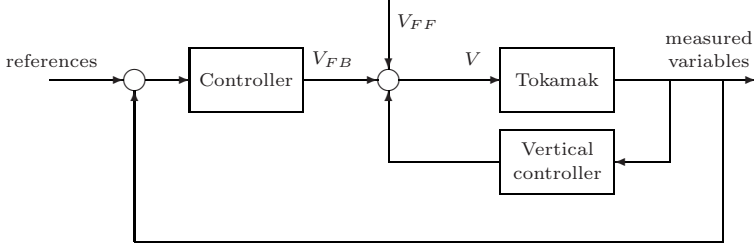


**Figure 4.1.** Simplified scheme of a plasma magnetic control feedback scheme

2. later, the current and shape controller is designed on the basis of the *stable* system obtained considering the presence of the vertical stabilization controller.

This double loop approach is theoretically justified by the fact that vertical stabilization and the shape controllers typically act on different time scales: it is therefore possible to separate the two problems and treat them one at a time.

The design of two vertical stabilization controllers carried out for ITER and at TCV will be presented in Chapter 6.

## 4.4 Control of the Currents in the Active Coils

Figures 4.1 and 4.2 show two possible feedback schemes for a plasma position, current and shape controller.

The first scheme, shown in Figure 4.1 is in a certain sense a very abstract scheme: it is supposed that the actual inputs to the plant are the voltages applied to the power supplies of the various coils, and that the controller gives the feedback part of the voltages ( $V_{FB}$ ), which are then added to the preprogrammed voltages ( $V_{FF}$ ) and applied to the plant.

More often, the feedback controller is divided into two parts. The first controller (the *shape controller*) evaluates the current adjustments ( $I_{FB}$ ) that are needed to control the plasma shape; these currents are summed with the preprogrammed currents ( $I_{FF}$ ). Finally, the total currents are passed to a current controller that, based on the current errors, evaluates the voltages to be applied to the plant.

As shown in Figure 4.2, in some cases control of the plasma shape is carried out using the coil currents as control inputs, rather than the coil voltages. Since the inputs to the tokamak coils are in any case the voltages to be applied to the power supplies, usually a feedback system is designed to calculate the voltages needed starting from the current requests. The design of this feedback system is usually done on the basis of a plasmaless model, in

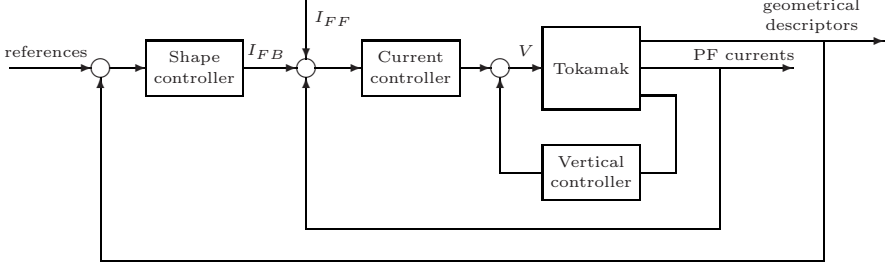


**Figure 4.2.** Schematic representation of a plasma control feedback scheme in which the current control is used

such a way that in dry discharges (*i.e.*, discharges with no plasma) the current references are tracked with a certain accuracy.

When the plasma is present, assuming that it has been vertically stabilized with a suitable separate loop, it acts as a disturbance to this feedback system.

The equations used to design the current controller are based on the plasmaless model presented in Section 2.3, where the presence of the passive structure is neglected (Equation 2.37)

$$L_a \dot{x}_a + R_a x_a = u. \quad (4.11)$$

Since the number of state variables in Equation 4.11 is equal to the number of control inputs (it is assumed that each coil is equipped with an independent power supply), a sufficiently high gain should allow the achievement of good tracking performance and good disturbance rejection. A good and simple control strategy is

$$u = -R_a x_a + L_a \Lambda (r_{x_a} - x_a), \quad (4.12)$$

where  $r_{x_a}$  is the vector of current requests and  $\Lambda$  is a diagonal matrix which specifies the closed-loop behaviour. Indeed, by substituting Equation 4.12 in Equation 4.11 we obtain

$$\dot{x}_a = -\Lambda x_a + \Lambda r_{x_a}.$$

The matrix  $\Lambda$  is chosen taking into account the maximum available voltage on each coil.

Once the current control loop is closed, the current requests can be seen as the new control inputs for the other external controllers. To design this external controller a current driven model is needed. To start with, let us consider the circuit equations describing the eddy and plasma currents

$$\begin{pmatrix} L_e^* & L_{ep}^* \\ L_{pe}^* & L_p^* \end{pmatrix} \begin{pmatrix} \delta \dot{x}_e \\ \delta \dot{I}_p \end{pmatrix} + \begin{pmatrix} L_{ea}^* \\ L_{pa}^* \end{pmatrix} \delta \dot{x}_a + \begin{pmatrix} R_e & 0 \\ 0 & R_p \end{pmatrix} \begin{pmatrix} \delta x_e \\ \delta I_p \end{pmatrix} = 0. \quad (4.13)$$

In Equations 4.13, since they are design equations, we neglect the disturbance terms.



Now let

$$\begin{pmatrix} \delta\psi_e \\ \delta\psi_p \end{pmatrix} = \begin{pmatrix} L_e^* & L_{ep}^* \\ L_{pe}^* & L_p^* \end{pmatrix} \begin{pmatrix} \delta x_e \\ \delta I_p \end{pmatrix} + \begin{pmatrix} L_{ea}^* \\ L_{pa}^* \end{pmatrix} \delta x_a, \quad (4.14)$$

from which

$$\begin{pmatrix} \delta x_e \\ \delta I_p \end{pmatrix} = \begin{pmatrix} L_e^* & L_{ep}^* \\ L_{pe}^* & L_p^* \end{pmatrix}^{-1} \left( \begin{pmatrix} \delta\psi_e \\ \delta\psi_p \end{pmatrix} - \begin{pmatrix} L_{ea}^* \\ L_{pa}^* \end{pmatrix} \delta x_a \right). \quad (4.15)$$

Finally, from Equations 4.13 and 4.15, we obtain a state-space model having  $\delta x_a$  as input

$$\begin{aligned} \begin{pmatrix} \delta\dot{\psi}_e \\ \delta\dot{\psi}_p \end{pmatrix} &= - \begin{pmatrix} R_e & 0 \\ 0 & R_p \end{pmatrix} \begin{pmatrix} L_e^* & L_{ep}^* \\ L_{pe}^* & L_p^* \end{pmatrix}^{-1} \begin{pmatrix} \delta\psi_e \\ \delta\psi_p \end{pmatrix} \\ &\quad + \begin{pmatrix} R_e & 0 \\ 0 & R_p \end{pmatrix} \begin{pmatrix} L_e^* & L_{ep}^* \\ L_{pe}^* & L_p^* \end{pmatrix}^{-1} \begin{pmatrix} L_{ea}^* \\ L_{pa}^* \end{pmatrix} \delta x_a. \end{aligned}$$

In a similar way it is possible to obtain an output equation in which the outputs are linear combinations of the new state variables  $\delta\psi_e$  and  $\delta\psi_p$ , and of the input  $\delta x_a$ .

## 4.5 Possible Different Solutions

In later chapters we will present the feedback control systems designed for four different machines:

1. FTU in Italy;
2. TCV in Switzerland;
3. JET tokamak in UK;
4. ITER, a world project tokamak that is going to be built in the next decade in France.

The control systems designed for FTU, JET and TCV have been implemented on the machines and the performance of the control systems have been in very good agreement with the expected simulated results. The design procedure we have adopted in these cases has been the following.

- Once a model in the form (4.6) is available, use this model to reproduce past experiments. This step can be typically carried out in two ways
  - by means of open-loop simulations of the plant, using registered data and comparing the simulation and the experimental results; these simulations are quite critical due to the plasma vertical instability, and to the uncertainties on the values of some plasma parameters. This approach typically leads to large differences between expected results and experimental results and for this reason this way of validating the model is usually not pursued;

- by means of a closed-loop comparison between simulation results and experimental results. Of course, in order to carry out this comparison, it is necessary to develop a model also of the feedback controllers that have been adopted during the discharges analysed. In this case the comparison is much more significant and good agreement between simulated results and experimental results gives good confidence in the plasma model.
- Design of a feedback controller for the plasma position, current and shape control. For this task the technique to adopt strongly depends on the problem being tackled. In general, all we can say is that the problem must be dealt with using MIMO techniques because of the significant coupling among the various input–output variables. But there is no general rule to follow. The best technique to use depends on
  - the number and type of controlled variables. Among the controlled variables, for elongated plasmas, there is always the time derivative of the vertical position of the plasma current centroid. Moreover, in almost all tokamaks, the magnitude of the plasma current is routinely controlled in feedback. For shape control, as already discussed, the number of controlled variables depends on the machine, on the sensors with which it is equipped and on the plasma shape reconstruction code that is available;
  - the requirements on the controlled variables. Typically these requirements are expressed in terms of maximum variations of the controlled variables that can be tolerated; moreover, the time needed to recover from a specified disturbance is usually specified;
  - the number of control variables. The construction of many of the various tokamaks around the world has not taken into account a detailed analysis of control performance that was to be achieved. This is mainly due to the fact that many requirements have arisen *after* construction of the tokamaks, when there is almost no possibility of modifying the machine. Therefore all we can do is exploit the available degrees of freedom to achieve the best possible performance;
  - the *physical* limitations on the plant actuators. These limitations are expressed in terms of maximum allowable voltages, currents, peak power and power time derivative.
- Once the controller is designed, before it is used for experiments, massive simulations are carried out, sometimes using different plant models, to check its robustness in the presence of possible *worst-case* disturbances.

The solutions we discuss in the following chapters are:

- *FTU*. The plasmas typically obtained in this tokamak have a circular cross-section; as a consequence no vertical instability is present. The control task is then reduced to the control of the magnitude of the plasma current and of the radial position. Due to the simplicity of these tasks, the adopted

feedback control structure consists of two SISO feedback loops designed separately (Chapter 5). This controller has been experimentally validated.

- *TCV*. For the TCV tokamak, the design is split into two parts. First, the vertical stabilization controller is designed using a SISO approach (Section 6.2); then the current and shape controller is designed, fitting the problem in the  $H_\infty$  framework (Chapter 8). The resulting controller has been experimentally validated.
- *JET*. Regarding the JET tokamak, in this book we will present only the design of the current and shape controller (Chapter 9). This design has been carried out using an optimal output regulation approach. This new controller for JET has been given the name eXtreme Shape Controller (XSC); it has been fully commissioned and is now used during experiments where accurate control of the plasma shape is needed.
- *ITER*. For the ITER tokamak, a two-time-scale approach is used: first the plasma is vertically stabilized by means of a static, proportional controller (Section 6.1); then a low-order controller is designed using a singular perturbation decomposition approach (Chapter 7). In this case, since the ITER tokamak is under construction, assessment of the results has been carried out only via simulation.

---

## Plasma Position and Current Control at FTU

In this chapter we present the design of a plasma radial position and current controller for the FTU tokamak. This design is based on a detailed simulation model of the tokamak; exploiting this model-based approach, no experimental tuning of the controller gains has been necessary.

The main parameters of the FTU tokamak are shown in Table 5.1.

In the description of the various controllers for plasma position, current and shape control, we present this design as a first example, since in this case the problem is made much easier by the fact that the plasma cross-section is circular. Therefore the plasma is not vertically unstable. Moreover, in this case no specification for the plasma shape was given: the plasma is *controlled* once the current magnitude and the radial position (in particular the outer radius of the plasma) are regulated. These two problems can be tackled separately and so we end up with two single-input–single-output feedback loops, one for each controlled variable. One peculiarity of this design is the fact that the plasma model is not, as usually happens, voltage driven, it is current driven. Therefore we need to use the model in the form presented in Section 4.4.

First of all we present the structure of the overall design model, consisting of various sub-systems; then we derive the mathematical models of the sub-systems on the basis of physical–geometrical relationships. This mathematical model has then been analysed and fine tuned using experimental data. The resulting plasma circuits power supply open-loop model has then been used to design new feedback controllers for the radial position and for the plasma current.

The simulated results and the results obtained experimentally have shown excellent agreement [68], validating the model-based design procedure. The new controller has been implemented on the plant and experimentally proven for two different plasmas: one with nominal plasma current of 500 kA, and one with nominal plasma current of 360 kA.

The chapter is organized as follows. First the structure of the overall simulation model is presented, together with the mathematical models of the various sub-systems. Then we focus on the design of the new feedback controllers.

Our effort is concentrated on demonstrating that the FTU simulation model we built up is a reliable tool for the design of new controllers; moreover, we improved the performance previously obtained on the plant. The experimental result of shots #19675 and #19842 show that the predicted performances were actually delivered during FTU operation [68].

**Table 5.1.** Main FTU parameters

Plasma major radius [m]	0.935
Plasma minor radius [m]	0.31
Plasma Current [MA]	up to 1.6
Toroidal Field flat-top duration [s]	1.5
Toroidal Field Energy [MJ]	160
Poloidal Field Energy [MJ]	200

## 5.1 The FTU Simulation Model

The closed loop simulation scheme (Figure 5.1) for FTU is made up of the following blocks:

- the plasma linearized model, which, on the basis of variations of the currents flowing in the four active coils available in FTU (coils T, V, H and F; Figure 5.2), and of the variations of the plasma parameters  $l_i$  and  $\beta_p$ , evaluates the variations of the magnetic fields and fluxes in the probe locations and the variation of the plasma current;
- the linearized reconstruction algorithm, which estimates the variable which is actually used in feedback by the radial controller (the radial flux imbalance,  $\Delta\psi_h$ ) on the basis of the total currents in the active coils and of the total field and flux measurements. Given the actual  $R_{max}$ , and the desired  $\tilde{R}_{max}$ , outer radii (Section 3.2), the radial flux imbalance is defined as

$$\Delta\psi_h = \psi(\tilde{R}_{max}, 0) - \psi(R_{max}, 0); \quad (5.1)$$

- the feedback radial and current controllers, which correct the currents in the F and T coils, respectively, in order to track the desired references; the F circuit is used for radial position control whereas the T circuit is used to control the plasma current;
- the model of the F and T converters, which try to guarantee that the currents flowing in these active coils are as close as possible to the values

requested by the feedback radial and current controllers plus the preprogrammed values.

In the following sections we give descriptions of the various blocks.

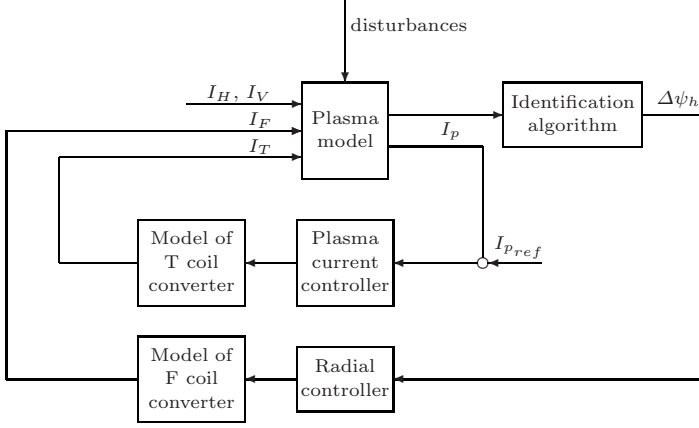


**Figure 5.1.** FTU feedback simulation scheme

### 5.1.1 Plasma Model

The plasma model that has been used in this analysis is the CREATE-L linearized model [48]. In this case, however, the model is current driven and not voltage driven (see Section 4.4). Proceeding as in Section 4.4, it is possible to obtain a model with state equation

$$\begin{aligned} \begin{pmatrix} \delta\dot{\psi}_e \\ \delta\dot{\psi}_p \end{pmatrix} = & - \begin{pmatrix} R_e & 0 \\ 0 & R_p \end{pmatrix} \begin{pmatrix} L_e^* & L_{ep}^* \\ L_{pe}^* & L_p^* \end{pmatrix}^{-1} \begin{pmatrix} \delta\psi_e \\ \delta\psi_p \end{pmatrix} \\ & + \begin{pmatrix} R_e & 0 \\ 0 & R_p \end{pmatrix} \begin{pmatrix} L_e^* & L_{ep}^* \\ L_{pe}^* & L_p^* \end{pmatrix}^{-1} \begin{pmatrix} L_{ea}^* \\ L_{pa}^* \end{pmatrix} \delta x_a + \begin{pmatrix} E_e \\ E_p \end{pmatrix} \delta w, \end{aligned} \quad (5.2)$$

and output equation

$$\begin{aligned} \delta y = & (C_a \ C_e \ C_p) \begin{pmatrix} \delta x_a \\ \delta x_e \\ \delta I_p \end{pmatrix} + F \delta w \\ = & (C_e \ C_p) \begin{pmatrix} L_e^* & L_{ep}^* \\ L_{pe}^* & L_p^* \end{pmatrix}^{-1} \begin{pmatrix} \delta\psi_e \\ \delta\psi_p \end{pmatrix} \\ & + \left( C_a - \begin{pmatrix} L_e^* & L_{ep}^* \\ L_{pe}^* & L_p^* \end{pmatrix}^{-1} \begin{pmatrix} L_{ea}^* \\ L_{pa}^* \end{pmatrix} \right) \delta x_a + F \delta w \end{aligned} \quad (5.3)$$

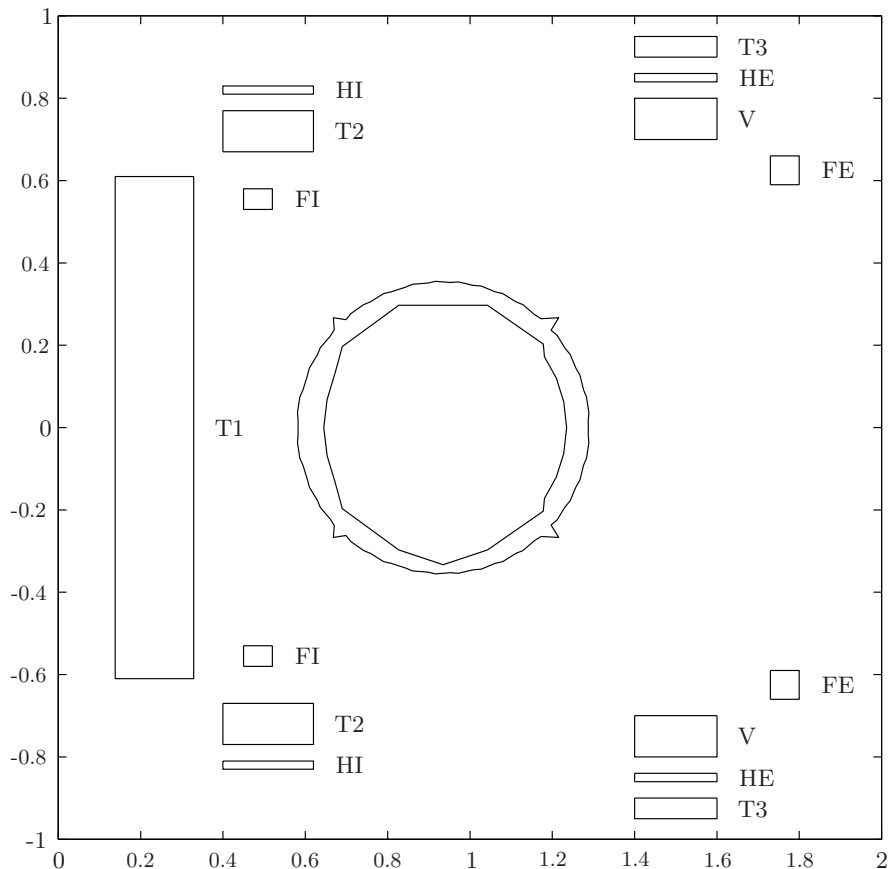


**Figure 5.2.** Schematic view of the FTU cross-section, where the poloidal field coils and the almost circular vacuum chamber are shown

where

- $\delta x_a$  is the vector of deviations of currents in the active coils; since the model is current driven, the vector  $\delta x_a$  represents the *input* to the model;
- $\delta \psi_e$  and  $\delta \psi_p$  are suitable state variables introduced (Equation 4.14) to derive the current driven model;
- $\delta I_p$  is the plasma current deviation;
- $\delta w$  is the vector of the plasma parameters  $\beta_p$  and  $l_i$  deviations, assumed to be known disturbances;
- $\delta y$  is the vector of the magnetic measurements deviations (magnetic fields and fluxes).

One of the problems encountered in the simulations has been the estimation of the plasma resistance  $R_p$ , which is usually neglected in the CREATE-L model.

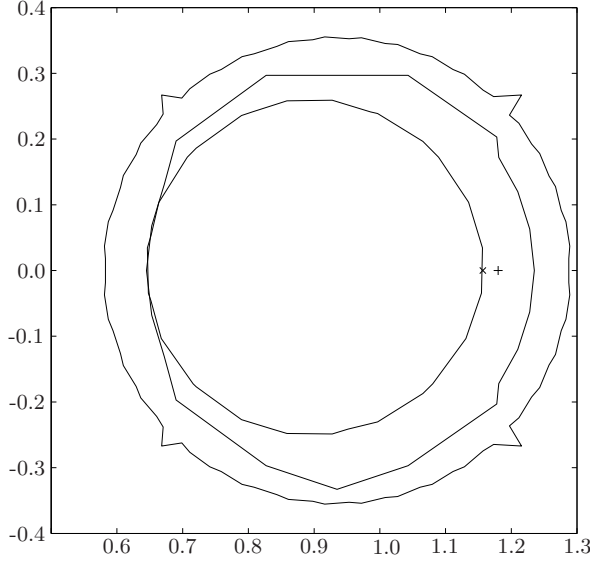


**Figure 5.3.** Definition of the poloidal flux imbalance. The figure shows a typical circular FTU plasma inside the vacuum vessel; the actual outer radius is indicated by a “x” symbol, while the desired outer radius is indicated by a “+”. The radial flux imbalance is defined as  $\Delta\psi_h = \psi(\tilde{R}_{max}, 0) - \psi(R_{max}, 0)$ . Since the plasma is circular, no vertical instability is present.

This resistance has been introduced in Equation 5.2, tuning its value by means of an open-loop optimization, using the experimental data. Moreover, also the elements of the vessel resistance matrix  $R_e$  were finely tuned on the basis of experimental data, in order to improve the agreement between the simulation results and the experimental data.

In Figure 5.4, with reference to shot #19389, the experimental data for the plasma current is compared with the reconstruction of the plasma current obtained using the experimental data for the currents and the plasma parameters  $\beta_p$  and  $l_i$ .

### 5.1.2 Plasma Shape Identification Block

The variable which is controlled in feedback by the radial controller, that is the radial flux imbalance  $\Delta\psi_h$ , is not directly available as a measure. Therefore identification of the plasma shape is needed in order to estimate  $\Delta\psi_h$ . The algorithm for the identification makes use of the total values of the currents flowing in the four active circuits, and of the total fluxes and magnetic field measurements.

In Figure 5.5, with reference to shot #19389, the experimental data for  $\Delta\psi_h$  is compared with the reconstruction of  $\Delta\psi_h$  obtained using the experi-



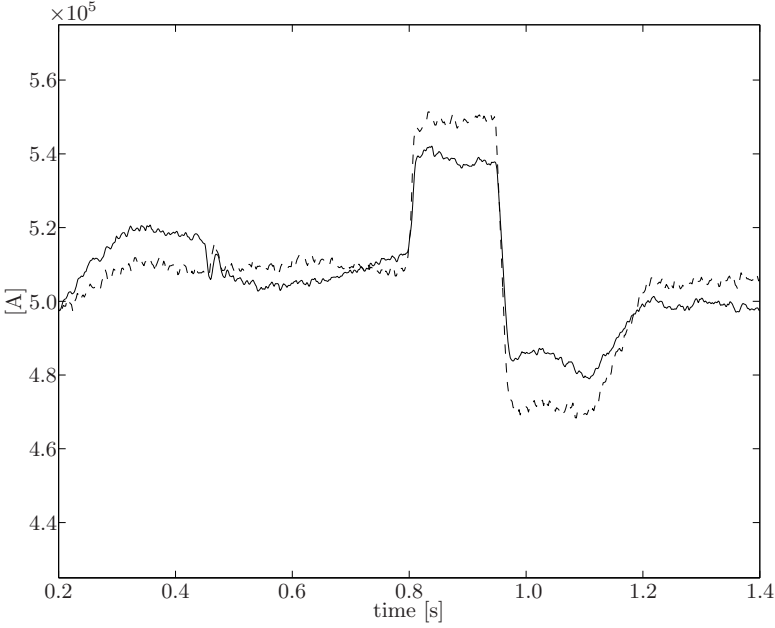


**Figure 5.4.** Shot #19389: plasma current as estimated by the CREATE-L model compared with the experimental data (dashed)

mental data for the currents and the magnetic measurements: the two traces show good agreement.

### 5.1.3 The Radial and Plasma Current Controllers

The radial and plasma current feedback controller have the same structure: they are PID discrete-time controllers. Denoting by  $U(z)$  the generic controller output and by  $E(z)$  its generic input, the transfer function of the two controllers is

$$U(z) = K \left( K_p + K_i \frac{T}{2} \frac{z+1}{z-1} + K_d \frac{z-1}{(T+\tau_d)z-\tau_d} \right) \frac{1}{z} E(z). \quad (5.4)$$

where:

- $K_p$  is the proportional gain;
- $K_i$  is the integral gain. The integral action is approximated using the trapezoidal method;
- $K_d$  is the derivative gain;
- $K$  is a scaling factor;
- $T$  is the controller sampling period;
- $\tau_d$  is a time constant used to approximate the derivative action.

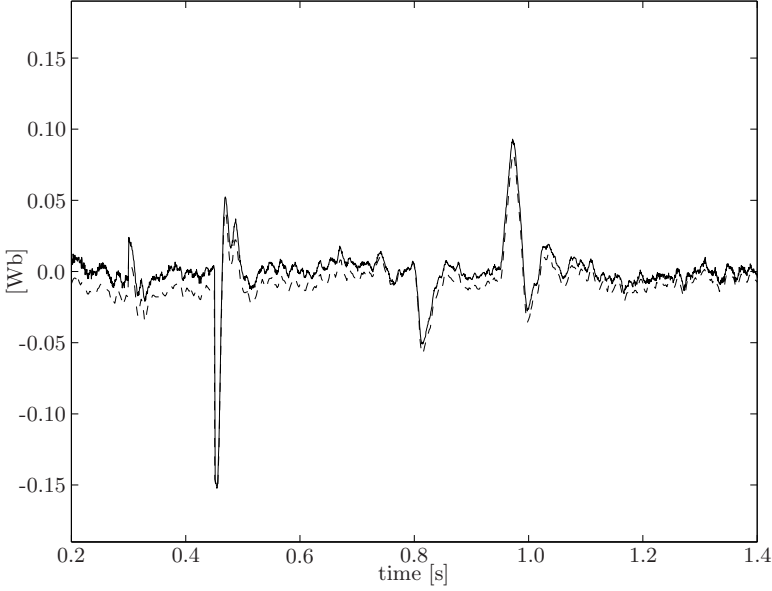


**Figure 5.5.** Shot #19389:  $\Delta\psi_h$  as estimated by the identification algorithm compared with the experimental data (dashed)

For the input–output variables, the input to the radial controller is the radial flux imbalance  $\Delta\psi_h$  whose reference value is identically zero (indeed if  $\Delta\psi_h = 0$ , then  $R_{max} = \hat{R}_{max}$ ; see Equation 5.1), and its output is the requested correction to the F current needed to drive the controlled variable to zero. The input to the plasma controller is the error on the plasma current and its output is the requested correction to the T current needed to drive the plasma current to its reference value.

#### 5.1.4 The F and T Circuit Converter Models

From the point of view of the analysis of the closed-loop behaviour, the converters of the F and T circuits cannot be neglected since they introduce a significant time delay, which affects the behaviour and introduces a limitation on the attainable performance.

In this analysis, the behaviour of the two converters was approximated using second-order filters with time delay. The parameter of these filters have been tuned by means of an optimization carried out on the basis of the experimental data. The resulting filter approximating the converter of the F circuit is

$$G_F(s) = K_F \frac{(1 + s\tau_F)e^{-T_F s}}{1 + 2\frac{\zeta_F}{\omega_{n_F}} + \frac{s^2}{\omega_{n_F}^2}}. \quad (5.5)$$

On the other hand, the filter which best approximated the behaviour of the power supply for the T circuit has the following structure

$$G_T(s) = K_T \frac{e^{-T_T s}}{1 + 2\frac{\zeta_T}{\omega_{n_T}} + \frac{s^2}{\omega_{n_T}^2}}. \quad (5.6)$$

## 5.2 Choice of the Controller Gains

One of the aims of this study is to demonstrate that the simulation scheme described in Section 5.1 is a suitable tool for the design of new feedback controllers and to verify this experimentally. In this study, we restrict our attention to the redesign of the two PID controllers for the radial position and plasma current control, since we cannot change the structure (5.4) of the controllers. We changed the gains of the two PIDs without changing the structure of the controller. The design of these controllers was divided into the following steps:

1. from the full-order model (5.2)–(5.3), a reduced-order linear model was extracted with two inputs (the F and T currents) and two outputs (the radial flux imbalance  $\Delta\psi_h$  and the plasma current);
2. a continuous time approximation of the filter used in Equation 5.4 to approximate the derivative action was derived;
3. a Padé approximation of the two models (5.5) and (5.6) was considered;
4. the gains of the two feedback controllers were tuned one at a time, making use of the Nichols chart.

The assessment of the controller behaviour was carried out using the full-order model. We repeated in simulation shot #19389 (where the nominal plasma current is about 500 kA) with the new controller gains. The simulation results are shown in Figures 5.6 and 5.7.

In the choice of gains, our attempt was mainly focused on

- a) reducing the oscillations of the two controlled variables when their references are varied;
- b) reducing the settling time in the plasma current response.

The same controller was later used in simulations with a plasma with nominal plasma current of 360 kA. Also for this plasma, the new controllers showed an improvement in the closed-loop performance, especially in the promptness of the response of the plasma current.

The new controllers for the F and T circuits were then implemented on FTU. The experimental results [68] are in good agreement with the simulated results, proving the validity of the model-based approach in this *easy* design of two separate SISO PID controllers.

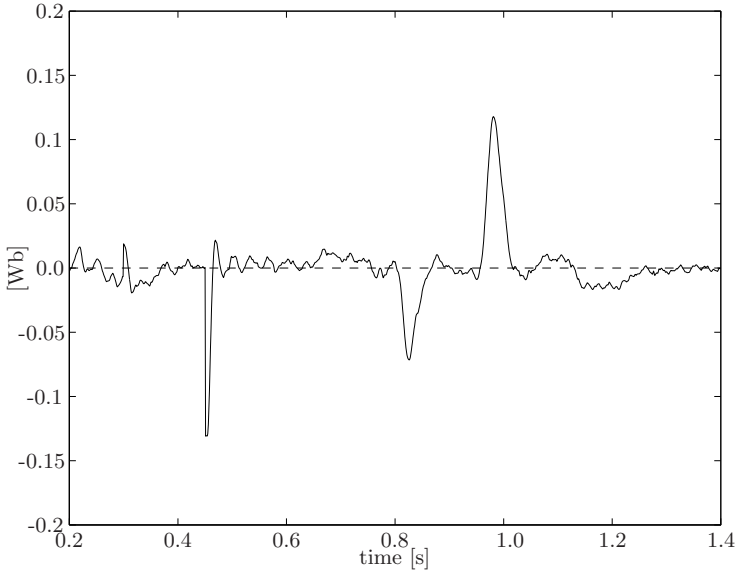


**Figure 5.6.** Closed-loop simulation results with the new controller:  $\Delta\psi_h$  (reference dashed)

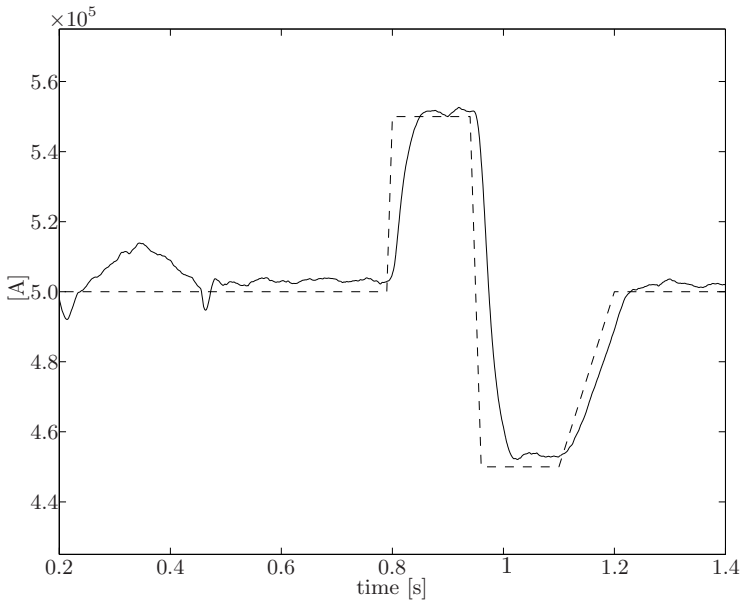


**Figure 5.7.** Closed-loop simulation results with the new controller: plasma current (reference dashed)

---

## Plasma Vertical Stabilization

In this chapter we present two examples of the design of vertical controllers for two different tokamaks: the experimental reactor ITER, which is currently under construction, and the tokamak operating in Switzerland, the TCV.

In both cases, the design of the vertical controller is carried out as a first, separate step of the overall plasma position, current and shape controller design. As already discussed in Section 4.3, this separation is possible because the vertical controller operates on a time scale that is much faster than the time scale on which the current and shape controller is required to react.

### 6.1 Vertical Stabilization Problem in the ITER Tokamak

The configuration of the ITER tokamak enables the design of a low-order controller based on the fact that the vertical position control and the plasma current and shape control can be performed on different time scales: indeed while the time constant of the unstable mode is about 100 ms, the settling time in the response to the reference signals can vary between 20 and 30 s. This time scale separation will be exploited in order to obtain a reduced-order model for the design of the current and shape control via a singular perturbation decomposition.

In the section we discuss how the vertical stabilization is carried out; the shape controller is then presented in Chapter 7.

Let us recall the linearized Equations 4.2

$$\begin{aligned}
& \begin{pmatrix} L_a^* & L_{ae}^* & L_{ap}^* \\ L_{ea}^* & L_e^* & L_{ep}^* \\ L_{pa}^* & L_{pe}^* & L_p^* \end{pmatrix} \begin{pmatrix} \delta \dot{x}_a \\ \delta \dot{x}_e \\ \delta \dot{I}_p \end{pmatrix} + \begin{pmatrix} R_a & 0 & 0 \\ 0 & R_e & 0 \\ 0 & 0 & R_p \end{pmatrix} \begin{pmatrix} \delta x_a \\ \delta x_e \\ \delta I_p \end{pmatrix} \\
& + \begin{pmatrix} E_a \\ E_e \\ E_p \end{pmatrix} \delta \dot{w} = B \begin{pmatrix} \delta u_a \\ 0 \\ 0 \end{pmatrix}, \\
& \delta y = C \begin{pmatrix} \delta x_a \\ \delta x_e \\ \delta I_p \end{pmatrix} + F \delta w.
\end{aligned}$$

Similarly to what was done in Section 4.1, the plasma current  $I_p$  can be eliminated from the state variables and, for the controller design, we can neglect the disturbances  $w$ . In this way, for the vertical stabilization controller design, we are reduced to the following linearized equations

$$\begin{pmatrix} \tilde{L}_a^* & \tilde{L}_{ae}^* \\ \tilde{L}_{ea}^* & \tilde{L}_e^* \end{pmatrix} \begin{pmatrix} \delta \dot{x}_a \\ \delta \dot{x}_e \end{pmatrix} + \begin{pmatrix} R_a & 0 \\ 0 & R_e \end{pmatrix} \begin{pmatrix} \delta x_a \\ \delta x_e \end{pmatrix} = \tilde{B} \begin{pmatrix} \delta u_a \\ 0 \end{pmatrix}, \quad (6.1a)$$

$$\delta z_c = (c_{az}^T \ c_{ez}^T) \begin{pmatrix} \delta x_a \\ \delta x_e \end{pmatrix}, \quad (6.1b)$$

where  $z_c$  is the centroid vertical position (Equation 2.48b).

First of all, let us split the external voltages  $u$  applied to the PF coils into two vectors, one ( $u_z$ ) used to control the vertical position and another ( $u_y$ ) devoted to the current and shape control

$$u_a = u_z + u_y. \quad (6.2)$$

The coils used for vertical stabilization in the ITER tokamak are PF2, PF3, PF4 and PF5 (Figure 6.1). As a matter of fact, there is just one vertical stabilization (VS) circuit that distributes a single voltage  $u_{VS}$  among the coils used for vertical stabilization. Therefore the  $u_z$  vector can be written as

$$u_z = \gamma u_{VS}, \quad (6.3)$$

where  $\gamma$  is the vector which selects the rows corresponding to the coils which are used for this purpose.

In the ITER tokamak, the active coils are superconductive, and hence the  $R_a$  matrix which appears in Equation 6.1a is equal to zero. This fact simplifies the plasma vertical stabilization which, in this case, can be accomplished just by means of proportional feedback control of the time derivative of the centroid vertical position  $\dot{z}_c$ . We chose to feed back the time derivative of the centroid vertical position  $\dot{z}_c$  rather than the centroid vertical position  $z_c$  itself, since  $\dot{z}_c$  is the measure that more often is available on tokamaks.

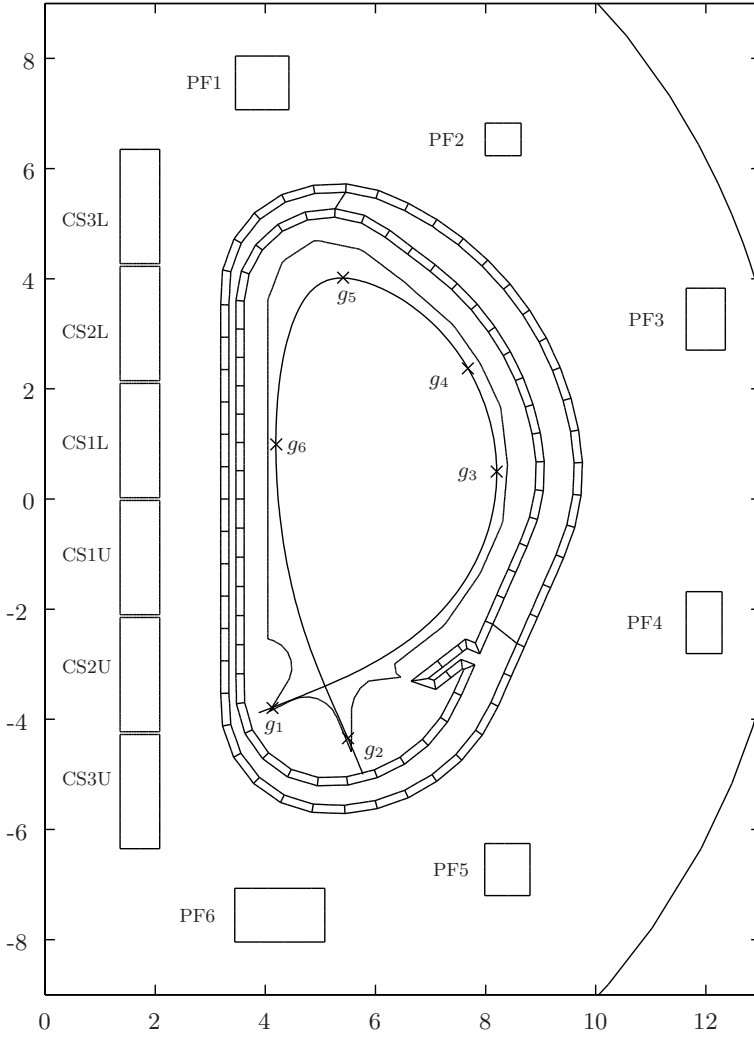


**Figure 6.1.** ITER cross-section, with the controlled gaps and poloidal field (PF) and central solenoid (CS) coils

Using Equations 6.2 and 6.3, under the assumption that  $R_a = 0$ , Equation 6.1a can be rewritten as

$$\begin{pmatrix} \delta \dot{x}_a \\ \delta \dot{x}_e \end{pmatrix} = \begin{pmatrix} 0 & A_{12} \\ 0 & A_{22} \end{pmatrix} \begin{pmatrix} \delta x_a \\ \delta x_e \end{pmatrix} + \begin{pmatrix} b_1 \\ b_2 \end{pmatrix} \delta u_{VS}. \quad (6.4)$$

On the other hand, since the desired output is  $\dot{z}_c$ , Equations 6.1b and 6.4 give

$$\begin{aligned}\delta\dot{z}_c &= (c_{az}^T \ c_{ez}^T) \begin{pmatrix} \delta\dot{x}_a \\ \delta\dot{x}_e \end{pmatrix} \\ &= (c_{az}^T \ c_{ez}^T) \begin{pmatrix} 0 & A_{12} \\ 0 & A_{22} \end{pmatrix} \begin{pmatrix} \delta x_a \\ \delta x_e \end{pmatrix} + (c_{az}^T \ c_{ez}^T) \begin{pmatrix} b_1 \\ b_2 \end{pmatrix} \delta u_{VS} \\ &= (0 \ c_2^T) \begin{pmatrix} \delta x_a \\ \delta x_e \end{pmatrix} + d \delta u_{VS}.\end{aligned}$$

Therefore, the model for vertical stabilization is the following single-input-single-output model

$$\begin{pmatrix} \delta\dot{x}_a \\ \delta\dot{x}_e \end{pmatrix} = \begin{pmatrix} 0 & A_{12} \\ 0 & A_{22} \end{pmatrix} \begin{pmatrix} \delta x_a \\ \delta x_e \end{pmatrix} + \begin{pmatrix} b_1 \\ b_2 \end{pmatrix} \delta u_{VS} \quad (6.5a)$$

$$\delta\dot{z}_c = (0 \ c_2^T) \begin{pmatrix} \delta x_a \\ \delta x_e \end{pmatrix} + d \delta u_{VS}. \quad (6.5b)$$

The transfer matrix associated with the state-space representation (6.5) is given by

$$W(s) = (0 \ c_2^T) \begin{pmatrix} sI & -A_{12} \\ 0 & sI - A_{22} \end{pmatrix}^{-1} \begin{pmatrix} b_1 \\ b_2 \end{pmatrix} + d \quad (6.6)$$

$$= c_2^T (sI - A_{22})^{-1} b_2 + d. \quad (6.7)$$

As can be seen, some simplifications occur when calculating the transfer function (6.7). The modes that are not observable from the chosen output, that is, the time derivative of the centroid vertical position  $\dot{z}_c$ , are the modes relative to the superconducting coils. All the eigenvalues that are cancelled are placed in the origin. Each of these eigenvalues has an associated Jordan block of order one; this guarantees that the associated modes are not unstable.

System (6.7) can be stabilized using as vertical controller a derivative gain

$$u_{VS} = -k_D \dot{z}_c. \quad (6.8)$$

The gain  $k_D$  has been selected with the aim of maximizing the phase margin. Taking into account the delays due to the power supply and to the diagnostic system, a phase margin of about 30 degrees at a cross-over frequency of 10 rad/s was obtained. In Figure 6.2 we show the Nyquist plot of the function obtained connecting system (6.5) in series with the controller (6.8). The closed-loop system is stabilized since we have one counterclockwise encirclement of  $-1$  and one open-loop unstable pole. Because of the presence of the unobservable modes in the origin, this controller is able to stop the plasma vertical motions but it does not recover the displacements. Anyway, this is not a concern since what we want to control accurately is not the plasma centroid



vertical position but rather the distance of the plasma boundary from the first wall, that is the gaps shown in Figure 6.1. This control is carried out by the shape controller, which will be presented in Chapter 7. Moreover, once the boundary shape is controlled, the movements of the plasma centroid are recovered.

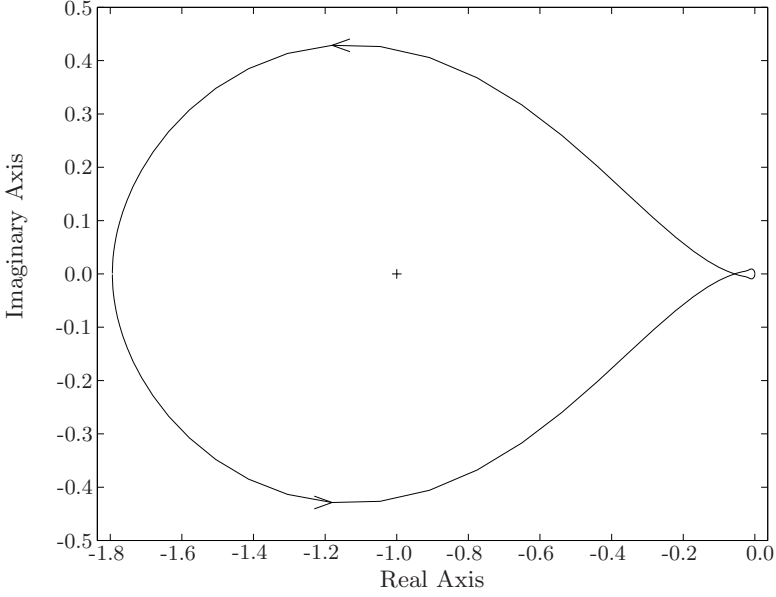


**Figure 6.2.** Nyquist plot of the open-loop SISO transfer function considered for vertical stabilization of the ITER tokamak

Finally, putting together Equations 6.3 and 6.8, the vertical controller is given by

$$u_z = -k_D \gamma \dot{z}_c = K_z \dot{z}_c. \quad (6.9)$$

## 6.2 Vertical Stabilization Problem for the TCV Tokamak

The second design example we will present concerns the TCV tokamak (Figure 6.3). A description of this tokamak can be found in Chapter 8. Hereafter we will focus only on the vertical stabilization problem.

The TCV elongated plasma we want to control are vertically unstable; robust stabilization of the plasma vertical position in this case is not a trivial task. Indeed a vertical shift of the plasma in the vessel of just a few centimetres

can modify the phase responses of the transfer functions between the voltages in the coils near the plasma and the vertical position by up to  $180^\circ$ .

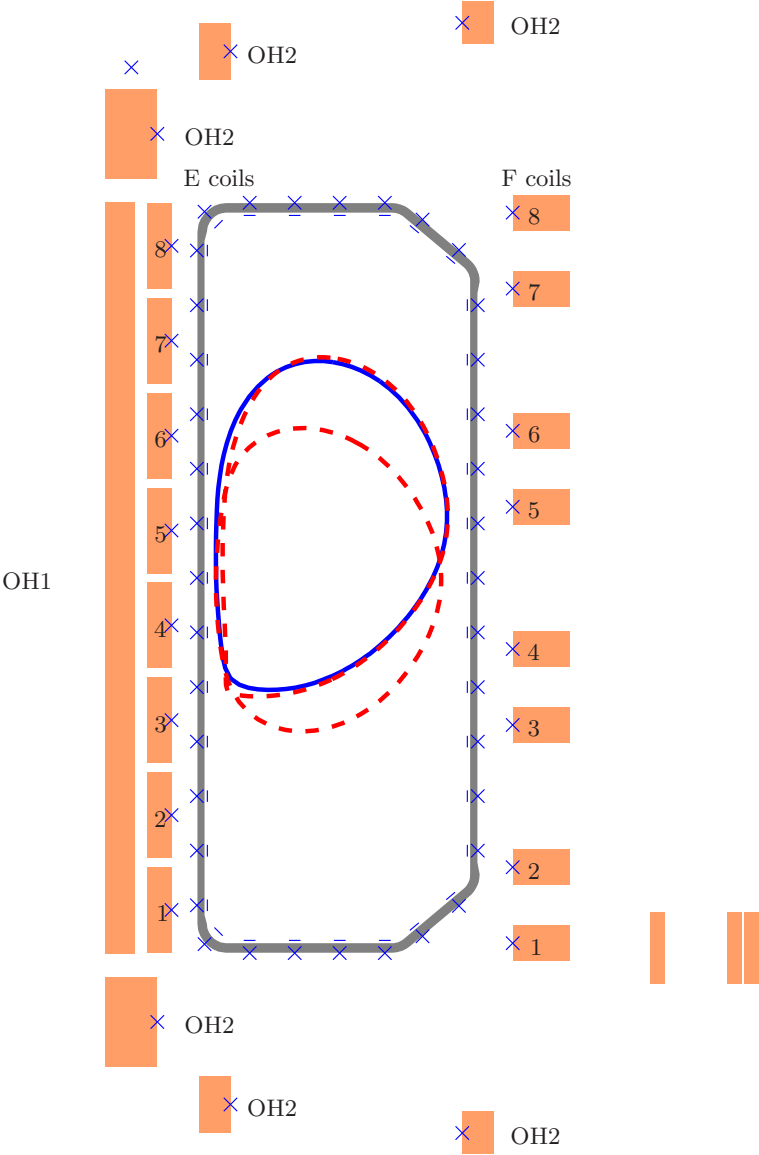


**Figure 6.3.** Separatrix contour shape of the plasma to be controlled (solid line). Other separatrices (dashed lines) show the degree to which the controller had to be robust against uncertainties in the plasma vertical position and shape.

As an example, in Figure 6.4 we show the Bode phase response of the plasma vertical position to a voltage stimulation in the E5 coil for two different plasmas:

- a limited centred plasma (the one shown dotted in the bottom in Figure 6.3);
- an up-down asymmetric plasma shifted about 11 cm above the midplane (the one shown solid in Figure 6.3).

The E5 coil is very close to the plasma in both cases, but because of the vertical shift, the response is of opposite sign.

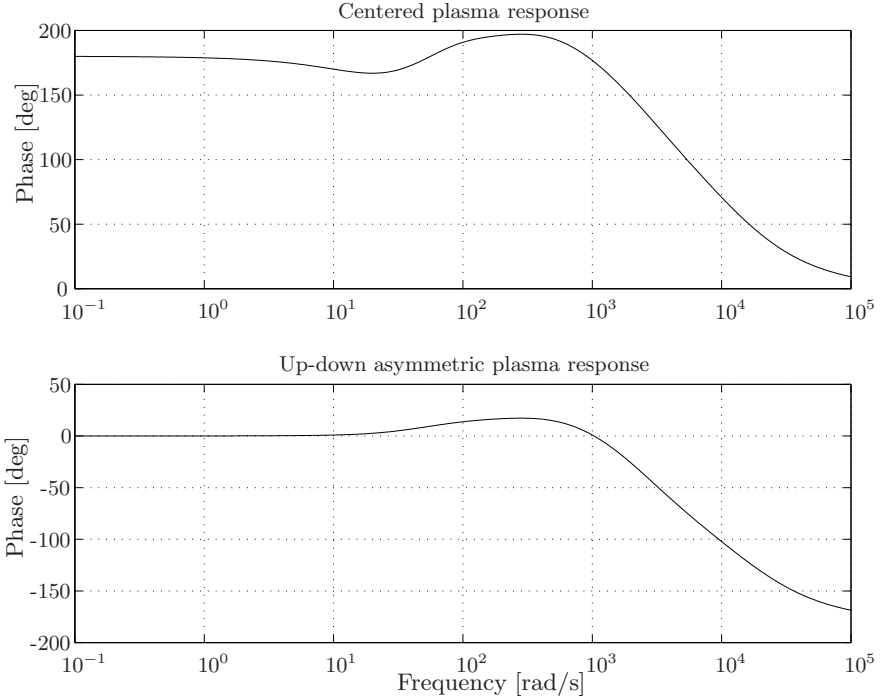


**Figure 6.4.** Phase response of the vertical centroid position to a voltage stimulation in the E5 coil for a centred plasma and for an up-down asymmetric plasma

During the experiments carried out at TCV, the reference tracked on the vertical position required a shift of 5 cm, but during a transient the vertical movement can exceed 10 cm. Therefore the behaviour of the coils near the plasma is very critical since it could even lead to closed-loop instability.

This strongly nonlinear behaviour of the plant makes it difficult to design a MIMO controller in just one step. Indeed, because of the conservativeness of almost all the MIMO controller design techniques with respect to structured

uncertainties, it is hard to find a controller that both stabilizes all the linearized models in the considered working envelope and guarantees the desired performance. Requiring a controller to be robustly stable for a wide variety of models while at the same time demanding an optimal performance is almost incompatible. In other words, we are looking for *robust performance*<sup>1</sup> for too wide a class of plants.

For these reasons, we choose to split the controller design into two steps. In the first step we stabilize the vertical position using only some of the poloidal field coils, namely those not too near the plasma. Afterwards, on the basis of the stabilized plant, we will design a second controller able to guarantee decoupling among the controlled parameters with acceptable dynamics, using the remaining coils. The current and shape controller for TCV will be presented in Chapter 8.

In the next section we present a SISO controller for control of the vertical position; this uses a simple PID controller.

The control of the other parameters, plasma current and shape, calls for a MIMO approach because of the strong output coupling between the controlled parameters. For this second step, we choose the  $H_\infty$  framework (Chapter 8).

### 6.2.1 Design of the Vertical Position Controller

The first step in the design of the vertical position controller is to derive a simplified vertical model from the full linear model. The nominal plasma we considered is not centred but is shifted about 11 cm above the midplane (Figure 6.3); for this reason the coils we chose as candidates for the vertical stabilization are not symmetric with respect to the midplane. Only eight coils were used: E3, E4, E6, E7; F3, F4, F6, F7. As discussed before, the E5 and F5 coils were not employed because their closeness to the plasma centre makes the sign of the gain (with respect to the vertical position) uncertain. As a consequence of this, if these two coils were also used, the closed-loop system could exhibit poor stability margins.

The eight coils chosen were grouped together to obtain a SISO system with an equivalent coil as input and  $zI_p$  as output. The coils were weighted differently, according to their resistances and to their position (above or below the plasma centroid).

Starting from the model of the plasma in the form (Equations 6.1)

$$\begin{pmatrix} \tilde{L}_a^* & \tilde{L}_{ae}^* \\ \tilde{L}_{ea}^* & \tilde{L}_e^* \end{pmatrix} \begin{pmatrix} \delta \dot{x}_a \\ \delta \dot{x}_e \end{pmatrix} + \begin{pmatrix} R_a & 0 \\ 0 & R_e \end{pmatrix} \begin{pmatrix} \delta x_a \\ \delta x_e \end{pmatrix} = \tilde{B} \begin{pmatrix} \delta u_a \\ 0 \end{pmatrix}, \quad (6.10a)$$

$$\delta z I_p = (c_{az}^T \ c_{ez}^T) \begin{pmatrix} \delta x_a \\ \delta x_e \end{pmatrix}, \quad (6.10b)$$

---

<sup>1</sup> Throughout this book we will make use of what has become the usual terminology in robust control theory. Reference books are [69], [70] and [71].

we selected the eight columns of the  $\tilde{B}$  matrix corresponding to the candidate coils to use, and the output to control. The output which is controlled is the height of the plasma current centroid with respect to the middle of the vacuum vessel, multiplied by the instantaneous plasma current. The way this vertical current moment  $zI_p$  is evaluated is discussed in Section 8.1.1 (Equation 8.2).

Then, in order to obtain the desired SISO system, we postmultiplied the  $\tilde{B}$  matrix by the vector

$$\left( 1 \ 1 \ -1 \ -1 \ \frac{R_F}{R_E} \ \frac{R_F}{R_E} \ -\frac{R_F}{R_E} \ -\frac{R_F}{R_E} \right)^T$$

where  $R_F$  and  $R_E$  represent the resistance of the E and F coils, respectively.

Denoting by  $u_{eq}$  the voltage applied to the equivalent circuit used for the vertical stabilization, system (6.10) was then written in the state-space form

$$\begin{pmatrix} \delta \dot{x}_a \\ \delta \dot{x}_e \end{pmatrix} = A \begin{pmatrix} \delta x_a \\ \delta x_e \end{pmatrix} + b \delta u_{eq} \quad (6.11a)$$

$$\delta \dot{z}_c = c^T \begin{pmatrix} \delta x_a \\ \delta x_e \end{pmatrix} + d \delta u_{eq}. \quad (6.11b)$$

A balanced realization of the stable part of system (6.11) was obtained, and balanced model reduction [72] was used to reduce it to sixth order.

The robust stabilization problem was made more challenging by the non-minimum phase zeros of the plant and by the high variability of the plasma growth rate. In fact, the growth rate of the unstable mode for the considered plasmas varies up to  $300 \text{ s}^{-1}$ , according to the position of the plasma in the vessel and to the field curvature of the equilibrium considered.

Based on the reduced-order model, a PID controller was designed using a standard frequency domain design method, trying to guarantee at the same time:

- good tracking of the reference pulse with an acceptable overshoot;
- satisfactory stability margins; in particular the gain and phase margins were chosen sufficiently high to guarantee stabilization of a number of models suitably chosen in the assumed working envelope;
- limited controller gains at high frequency, thus avoiding voltage spikes on the actuator coils that exceeded the voltage limits.

In Figure 6.5 the Nichols diagrams of three different open-loop transfer functions are shown, namely the cascade of the designed PID controller and the vertical model of three different plasma equilibria in the assumed working envelope. In particular, we chose the nominal plasma configuration, that is a limited plasma shifted about 11 cm above the midplane, a diverted plasma with the same vertical shift, and a limited centred plasma, which was much more unstable than the nominal one.

In our simulations we considered quantization of the error signal on  $zI_p$ . This error caused very nervous behaviour of the commanded voltages, with

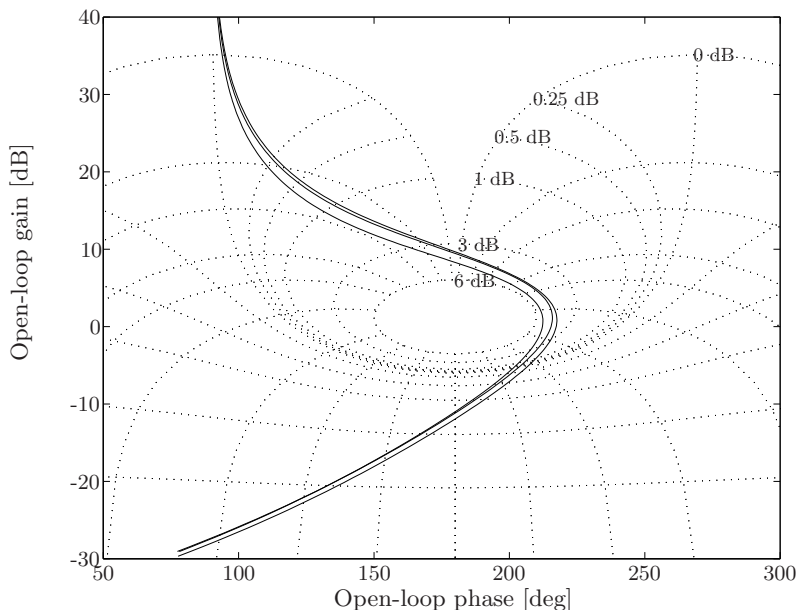


**Figure 6.5.** Nichols plots of the open-loop gains obtained considering three different plasmas and the PID designed controller. The controlled variable is the vertical position. The leftmost curve corresponds to a more unstable modelled discharge.

several spikes. To overcome this problem we chose to filter this error signal using the digital moving average filter

$$W(z) = \frac{z^3 + z^2 + z + 1}{4z^3}. \quad (6.12)$$

In this way the error signal is averaged over the last four samples, thus reducing the effect of the quantization error. The delay introduced by the filter (6.12) did not significantly deteriorate the closed-loop performance.

---

## Plasma Shape Control for ITER

In this chapter we show that the configuration of the ITER tokamak enables the design of a low-order controller based on the fact that the vertical position control and the plasma current and shape control can be performed on different time scales. This time-scale separation is exploited in order to obtain a reduced-order model for the design of the current and shape control via a singular perturbation decomposition. An important feature of our approach is that, with respect to other reduction procedures (such as Hankel norm approximation, balanced truncation, etc.), the singular perturbation decomposition allows us to retain the physical meaning of the state variable. The designed current and shape controller is a multivariable PI; it is able to guarantee a prescribed input–output behaviour to the closed-loop system.

The main parameters of the ITER tokamak are shown in Table 7.1.

**Table 7.1.** Main ITER parameters

Total Fusion Power [MW]	500
$Q$ - Fusion Power/Auxiliary Heating Power	10
Average (1 MeV) neutron wall loading [MW/m <sup>2</sup> ]	0.57
Plasma major radius [m]	6.2
Plasma minor radius [m]	2.0
Plasma Current [MA]	15
Toroidal Field at 6.2 m radius [T]	5.3
Plasma Volume [m <sup>3</sup> ]	837
Installed auxiliary heating/current drive power [MW]	73

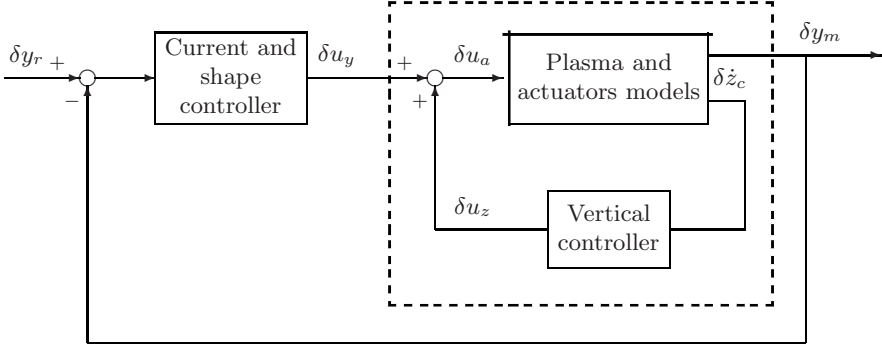


**Figure 7.1.** Feedback scheme for the ITER controller

## 7.1 Singular Perturbation Decomposition for the ITER Tokamak

After the vertical controller design (Section 6.1), we are left with the model boxed in the dashed frame in Figure 7.1.

This model presents as inputs the voltages  $\delta u_y$  applied to the active coils, that is the poloidal field (PF) coils and central solenoid (CS) coils shown in Figure 6.1. It is worth to notice that some of these coils, in particular PF2, PF3, PF4 and PF5, are used also by the vertical stabilization controller. More often, the vertical stabilization control is performed using dedicated circuits, which make use of a *fast* amplifier.

The outputs  $\delta y_m$  that we assume we have at our disposal are

- the six gaps shown in Figure 6.1;
- the plasma current;
- the active currents in the PF and CS coils.

As a matter of fact, on operating tokamaks, the feedback loop on the active current *deviations* is never used; instead what is often used is a feedback loop on the *total* currents (see for instance the design of the controller for JET in Chapter 9).

Let us now write the equations of the model we are going to use for the design of the current and shape controller. In the sequel we will omit the symbol  $\delta$  which, we recall, denotes deviations of the variables with respect to the nominal values. Making use of Equations 6.2, 6.9 and 6.1b, we have

$$u_a = u_z + u_y = -k_D \gamma \dot{z}_p + u_y = -k_D \gamma c_{1z}^T \dot{x}_a - k_D c_{2z}^T \dot{x}_e + u_y .$$

Therefore our original first equation in (6.1a) becomes

$$\tilde{L}_a \dot{x}_a + \tilde{L}_{ae} \dot{x}_e + R_a x_a = u_y ,$$

where



$$\begin{aligned}\tilde{L}_a &= L_{ae}^* + k_D \gamma c_{az}^T \\ \tilde{L}_{ae} &= L_{ae}^* + k_D \gamma c_{ez}^T,\end{aligned}$$

whereas the equation in (6.1a) regarding the passive circuits remains unchanged. Moreover we need to add an equation to describe the variations of the geometric descriptors chosen in this case, that is, the gaps shown in Figure 6.1. Therefore the system to consider for the current and shape control is

$$\tilde{L}_a \dot{x}_a + \tilde{L}_{ae} \dot{x}_e + R_a x_a = u_y \quad (7.1a)$$

$$L_{ea}^* \dot{x}_a + L_e^* \dot{x}_e + R_e x_e = 0 \quad (7.1b)$$

$$y = C_a x_1 + C_e x_2. \quad (7.1c)$$

This system presents about 200 states. In the following we show that in order to get a reduced-order system, we can apply the singular perturbation approach described in detail in [73].

First of all let us adopt the following change of variables

$$\begin{aligned}\psi_1 &= \tilde{L}_a x_a + \tilde{L}_{ae} x_e \\ \psi_2 &= L_{ea}^* x_a + L_e^* x_e.\end{aligned}$$

Therefore, our original variables  $x_a$  and  $x_e$  are given by

$$\begin{aligned}x_a &= E_{11} \psi_1 + E_{12} \psi_2 \\ x_e &= E_{21} \psi_1 + E_{22} \psi_2,\end{aligned}$$

with

$$\begin{aligned}E_{11} &= \Delta_1 \\ E_{12} &= -\Delta_1 \tilde{L}_{ae} L_e^{*-1} \\ E_{21} &= -L_e^{*-1} L_{ea}^* \Delta_1 \\ E_{22} &= L_e^{*-1} + L_e^{*-1} L_{ea}^* \Delta_1 \tilde{L}_{ae} L_e^{*-1},\end{aligned}$$

where

$$\Delta_1 = (\tilde{L}_a - \tilde{L}_{ae} L_e^{*-1} L_{ea}^*)^{-1}.$$

In this way Equations 7.1a and 7.1b become

$$\begin{aligned}\dot{\psi}_1 + R_a E_{11} \psi_1 + R_a E_{12} \psi_2 &= u_y \\ \dot{\psi}_2 + R_e E_{21} \psi_1 + R_e E_{22} \psi_2 &= 0,\end{aligned}$$

which can also be written as

$$\dot{\psi}_1 + R_a \Delta_1 \psi_1 - R_a \Delta_1 \tilde{L}_{ae} L_e^{*-1} \psi_2 = u_y \quad (7.2a)$$

$$\dot{\psi}_2 - R_e L_e^{*-1} L_{ea}^* \Delta_1 \psi_1 + R_e L_e^{*-1} (I + L_{ea}^* \Delta_1 \tilde{L}_{ae} L_e^{*-1}) \psi_2 = 0. \quad (7.2b)$$

The key point in this approach is that for the ITER tokamak we are considering, the time constants of the passive structures are small with respect to the other time constants of the system. Therefore we can write

$$R_e L_e^{*-1} = \frac{1}{\epsilon} \Gamma ,$$

where  $\epsilon$  is a small number. In our case, letting  $\|\Gamma\| = 1$ , we have  $\epsilon = 2 \times 10^{-3}$ . Therefore Equations 7.2 become

$$\dot{\psi}_1 = -R_a \Delta_1 \psi_1 + R_a \Delta_1 \tilde{L}_{ae} L_e^{*-1} \psi_2 + u_y \quad (7.3a)$$

$$\epsilon \dot{\psi}_2 = \Gamma L_{ea}^* \Delta_1 \psi_1 - \Gamma (I + L_{ea}^* \Delta_1 \tilde{L}_{ae} L_e^{*-1}) \psi_2 , \quad (7.3b)$$

which are in the standard singular perturbation form [73].

Now, using the procedure justified in [73], we approximate system (7.3) dividing it into a slow part, denoted by the subscript  $S$ , and a fast part, denoted by the subscript  $F$ . First of all, setting  $\epsilon = 0$ , and thus considering only the slow part, we have

$$\dot{\psi}_{1S} = -R_a \Delta_1 \psi_{1S} + R_a \Delta_1 \tilde{L}_{ae} L_e^{*-1} \psi_{2S} + u_y \quad (7.4a)$$

$$0 = L_{ea}^* \Delta_1 \psi_{1S} - (I + L_{ea}^* \Delta_1 \tilde{L}_{ae} L_e^{*-1}) \psi_{2S} . \quad (7.4b)$$

Solving Equation 7.4b for  $\psi_{2S}$ , assuming that  $(I + L_{ea}^* \Delta_1 \tilde{L}_{ae} L_e^{*-1})$  is not singular, we obtain

$$\psi_{2S} = (I + L_{ea}^* \Delta_1 \tilde{L}_{ae} L_e^{*-1})^{-1} L_{ea}^* \Delta_1 \psi_{1S} . \quad (7.5)$$

Substituting Equation 7.5 into Equation 7.4a results in the following slow model equation

$$\dot{\psi}_{1S} = -R_a \tilde{L}_a^{-1} \psi_{1S} + u_y . \quad (7.6)$$

For derivation of the fast sub-system, it is assumed that the slow variables are constant during fast transients, that is

$$\dot{\psi}_{2S} = 0 , \quad \psi_1 = \psi_{1S} , \quad (7.7)$$

and that the only fast variations are the deviations of  $\psi_2$  from  $\psi_{2S}$ . Letting

$$\psi_{2F} = \psi_2 - \psi_{2S}$$

and making use of Equations 7.3b and 7.7, we have

$$\dot{\psi}_{2F} = \dot{\psi}_2 = \frac{1}{\epsilon} \Gamma \left[ L_{ea}^* \Delta_1 \psi_{1S} - (I + L_{ea}^* \Delta_1 \tilde{L}_{ae} L_e^{*-1}) (\psi_{2S} + \psi_{2F}) \right] .$$

Now, using Equation 7.4b, we have the following fast model equation

$$\frac{d}{d\tau} \psi_{2F} = -\Gamma (I + L_{ea}^* \Delta_1 \tilde{L}_{ae} L_e^{*-1}) \psi_{2F} , \quad (7.8)$$

where  $\tau = t/\epsilon$ .

The *boundary layer* system (7.8) is uncontrollable but, since the original plant had already been stabilized, it turned out to be asymptotically stable with our choice of  $k_D$  in Equation 6.8.

Similarly, it can be shown that the outputs can be decomposed as

$$\begin{aligned} y(t) &= \tilde{C}_a \psi_{1S}(t) + \tilde{C}_e \psi_{2F}(t/\epsilon) + O(\epsilon) \\ &= y_S(t) + y_F(t/\epsilon) + O(\epsilon), \end{aligned}$$

where

$$\begin{aligned} \tilde{C}_a &= C_a \tilde{L}_a^{-1} \\ \tilde{C}_e &= C_a E_{12} + C_e E_{22}. \end{aligned}$$

### 7.1.1 Current and Shape Controller

We recall that the measurements  $y_m$  that are available to the current and shape controller are the gaps and the plasma current (the vector  $y$ ) and the active currents (the vector  $x_a$ ). Starting from system

$$\dot{\psi}_1 = -R_1 \Delta_1 \psi_1 + R_a \Delta_1 \tilde{L}_{ae} L_e^{*-1} \psi_2 + u_y \quad (7.9a)$$

$$\epsilon \dot{\psi}_2 = \Gamma L_{ea}^* \Delta_1 \psi_1 - \Gamma (I + L_{ea}^* \Delta_1 \tilde{L}_{ae} L_e^{*-1}) \psi_2 \quad (7.9b)$$

$$y_m = \begin{pmatrix} y \\ x_1 \end{pmatrix} = \begin{pmatrix} C_a E_{11} + C_e E_{21} & C_a E_{12} + C_e E_{22} \\ E_{11} & E_{12} \end{pmatrix} \begin{pmatrix} \psi_1 \\ \psi_2 \end{pmatrix}, \quad (7.9c)$$

neglecting high-frequency (*fast*) dynamics leads us to the following reduced-order system

$$\dot{\psi}_{1S} = u_y \quad (7.10a)$$

$$y_m = \begin{pmatrix} y \\ x_a \end{pmatrix} = \begin{pmatrix} \tilde{C}_a \\ \tilde{L}_a^{-1} \end{pmatrix} \psi_{1S}. \quad (7.10b)$$

In writing Equation 7.10a, we have also exploited the fact that in the ITER tokamak, the active coils are superconductive, and hence the  $R_a$  matrix which appeared in (7.6) is equal to zero.

For the design of the current and shape controller, we make use of the results in Section 3.7 of [73] (see in particular Theorem 7.1).

**Theorem 7.1 ([73]).** *If the boundary layer system (7.8) is asymptotically stable and uncontrollable, then there exists an  $\bar{\epsilon} > 0$  such that an output-feedback controller that stabilizes the reduced-order system (7.10), stabilizes the actual, full-order system (7.9) for all  $\epsilon \in ]0, \bar{\epsilon}]$ .*

In our case, the required assumptions on the fast part (7.8) were verified, since it is asymptotically stable and uncontrollable.

As control law for the current and shape feedback loop, we chose a multi-variable PI in the form

$$u_y = K_x x_a + K_P y + K_I \int_0^t (y - y_r) d\sigma, \quad (7.11)$$

where  $y_r$  indicates the references. With this control law, we accomplish our target of designing a low-order controller: indeed this control law has the same order as the system controlled outputs  $y$ .

Using Equation 7.11, the reduced-order closed-loop equations become

$$\begin{aligned} \dot{\psi}_{1S} &= (K_x \tilde{L}_a^{-1} + K_P \tilde{C}_a) \psi_{1S} + K_I \eta \\ \dot{\eta} &= \tilde{C}_a \psi_{1S} - y_r \\ y_m &= \begin{pmatrix} \tilde{C}_a \\ \tilde{L}_a^{-1} \end{pmatrix} \psi_{1S}. \end{aligned}$$

Now let  $K_x$  and  $K_P$  satisfy the equation

$$K_x \tilde{L}_a^{-1} + K_P \tilde{C}_a = -\alpha I, \quad (7.12)$$

where  $\alpha$  is a positive number. In this way, the controlled variable  $y$  is given by

$$\begin{aligned} \dot{y} &= -\alpha y + \tilde{C}_a K_I \eta \\ \dot{\eta} &= y - y_r. \end{aligned}$$

The integral gain  $K_I$  was chosen to satisfy

$$\tilde{C}_a K_I = -\beta I, \quad (7.13)$$

$\beta$  being a positive number, and such that the matrix

$$\begin{pmatrix} -\alpha I & K_I \\ \tilde{C}_a & 0 \end{pmatrix}$$

has all its eigenvalues in the open left-half plane. In this way the closed-loop reduced-order system is asymptotically stable and the transfer matrix between the references  $y_r$  and the actual outputs  $y$  is in the form

$$Y(s) = \begin{pmatrix} W(s) & 0 & \cdots & 0 \\ 0 & W(s) & \cdots & 0 \\ \vdots & & \ddots & \vdots \\ 0 & 0 & \cdots & W(s) \end{pmatrix} Y_r(s), \quad (7.14)$$

with

$$W(s) = \frac{\beta}{s^2 + \alpha s + \beta}. \quad (7.15)$$

Therefore, by choosing  $\alpha$  and  $\beta$ , we can assign the closed-loop behaviour of the reduced-order system.

Equations 7.12 and 7.13 can be satisfied in different ways. For instance, one possible choice is to select

$$(K_x \ K_P) = -\alpha \begin{pmatrix} \tilde{L}_a^{-1} \\ \tilde{C}_a \end{pmatrix}^\dagger, \quad (7.16)$$

where  $^\dagger$  indicates the Moore–Penrose pseudoinverse, and

$$K_I = -\tilde{L}_a \tilde{L}_a^T \tilde{C}_a^T (\tilde{C}_a \tilde{L}_a \tilde{L}_a^T \tilde{C}_a^T)^{-1} \beta. \quad (7.17)$$

With the choice as in Equation 7.16 it is attempted to keep the proportional part of the control voltages in Equation 7.11 as low as possible. On the other hand, the choice (7.17) is aimed at keeping the steady-state currents *low* when tracking some references  $y_r$ ; indeed it can be shown that the static gain matrix between the references  $y_r$  and the PF coil currents  $x_a$  is given by  $-\tilde{L}_a^{-1} K_I / \beta$ .

By virtue of Theorem 7.1, our design approach guarantees the closed-loop stability of the overall system, if  $\epsilon$  is sufficiently small. To check if this is verified in our case, we compared the two closed-loop systems obtained applying the control law (7.11) to the reduced-order system (7.10) and to the full-order system (7.9). Our assumption turned out to be correct. In Figure 7.2 we show the Bode diagrams of the response of the two systems on one of the diagonal I/O channels: it is possible to see that the actual transfer function (solid) is close, up to 5 rad/s, to the desired one (7.15). Moreover the desired decoupling among the controlled variables (Equation 7.14) is achieved: we verified that the closed-loop full-order system exhibits an attenuation of more than 50 dB on the off-diagonal channels.

## 7.2 Simulation Results

In this section, we show some simulation results using a model of an ITER tokamak plasma equilibrium configuration. The plasma position, current and shape controller was designed as described in Section 7.1.1.

We carried out two different kinds of simulations:

- a vertical displacement event (VDE), defined as an initial vertical offset of 2 cm of the plasma centroid along the unstable eigenvector;
- the tracking of a 10 cm reference on the controlled gaps and 100 kA on the plasma current.

Hereafter we show the simulation results for the VDE, for the tracking of a 100 kA step reference on the plasma current and for the simultaneous tracking of a 10 cm step reference on gap #3 and gap #4. We chose these two gaps because they exhibited the worst behaviours in terms of coupling with

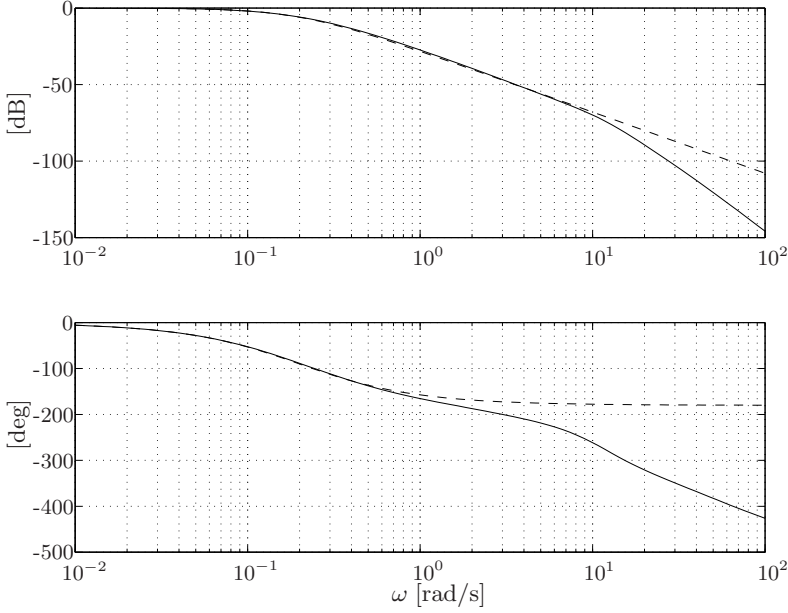


**Figure 7.2.** Bode diagrams of one closed-loop diagonal channel: full-order system solid, reduced-order system dashed

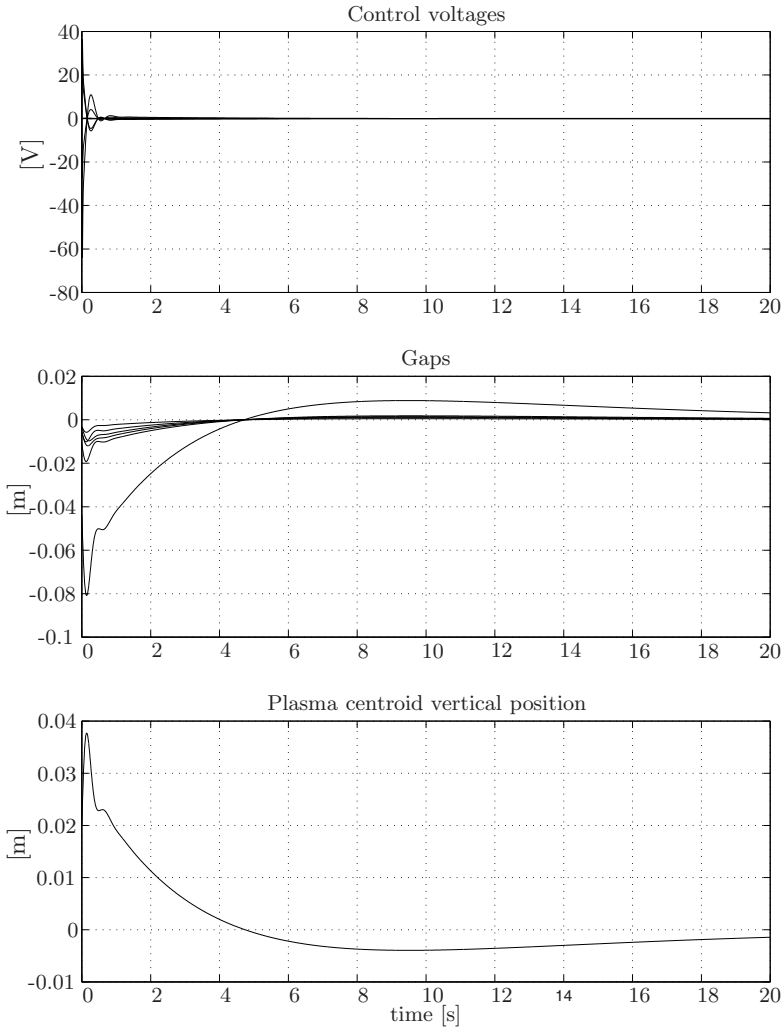
the other gaps; moreover control of gap #3 is important for the impedance coupling with the Ion Cyclotron Radio Frequency Heating antennae.

Figure 7.3 shows the control voltages, the gap and the plasma centroid vertical position time behaviours for the VDE. As can be seen, the results are satisfactory: the vertical displacement is recovered in 20 s with small gap deviations and negligible control effort.

In Figure 7.4 the plasma current tracking results are shown: the plasma current exhibits the desired time behaviour imposed on the reduced-order system (Equation 7.15), whereas all the gaps remain very close to zero, as desired (Equation 7.14).

In Figure 7.5 we present the results for gap tracking. Also in this case, gap #3 and gap #4 reach the desired values, while all the other gaps are practically zero.

In all cases, simulation results confirm the validity of our assumption of dividing the system into a slow and a fast part, and of designing the current and shape controller just on the basis of the slow part.



**Figure 7.3.** Control voltages, gaps and plasma vertical position for the VDE

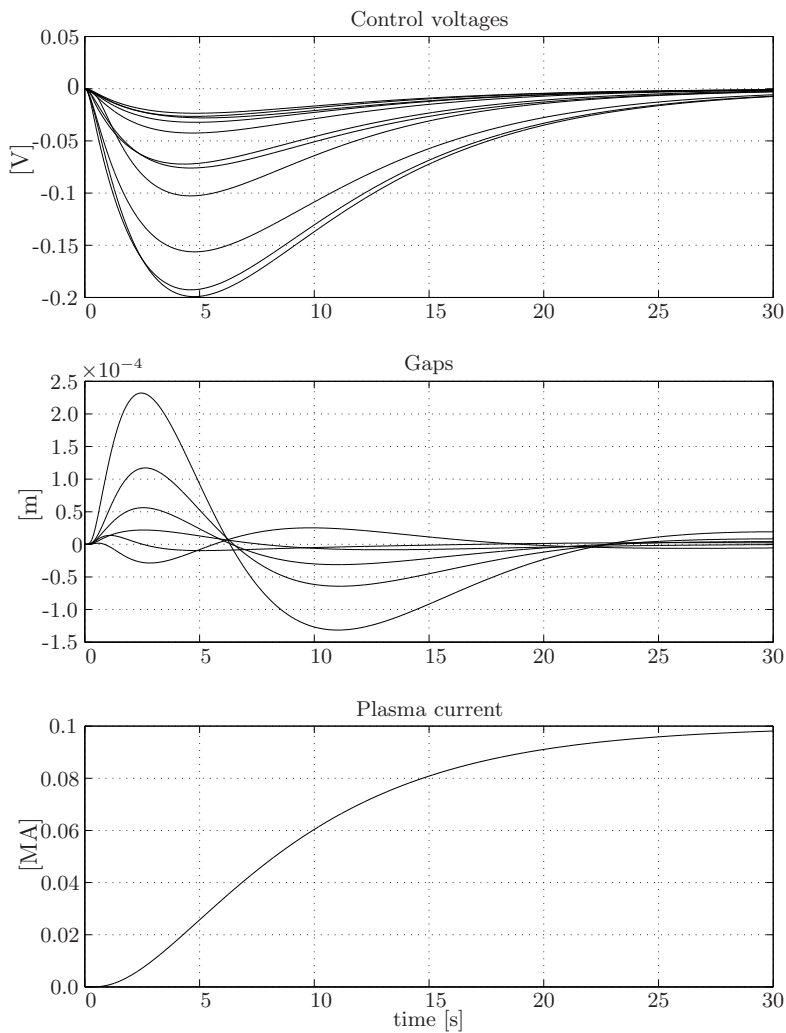


**Figure 7.4.** Control voltages, gaps and plasma current while tracking a 100 kA reference step in the plasma current



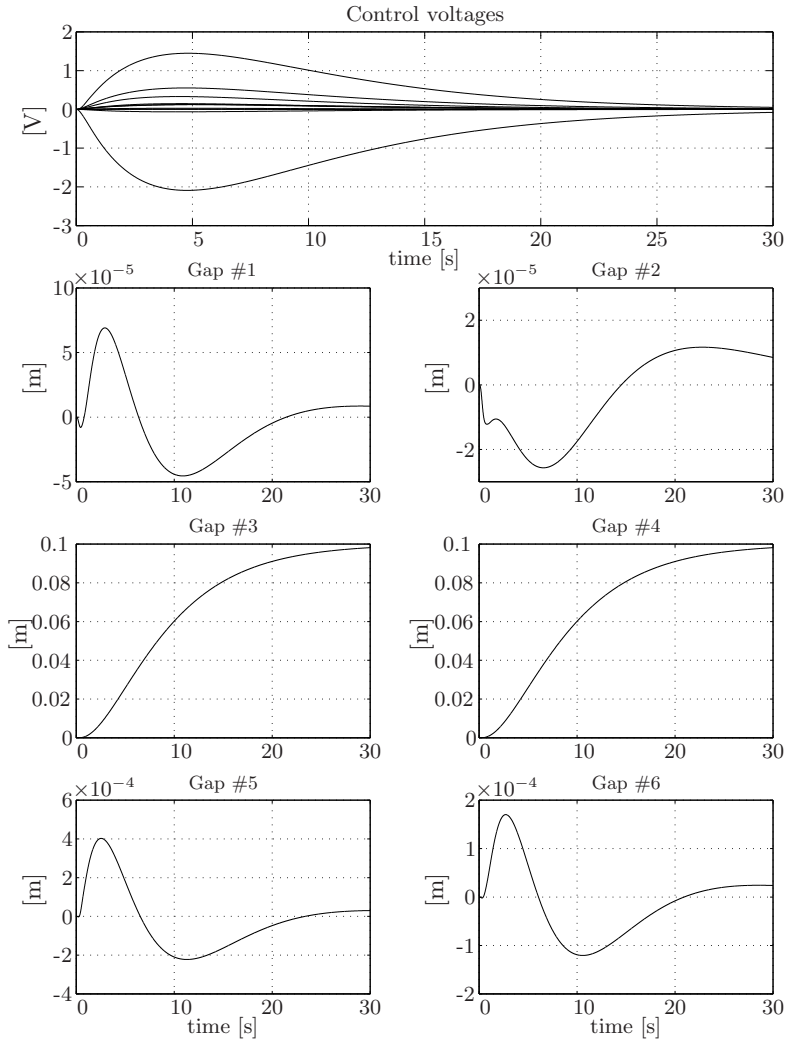


**Figure 7.5.** Control voltages and gaps while tracking 10 cm step references on gap #3 and gap #4

---

## Plasma Shape Control at TCV

### 8.1 Description of the TCV

A thorough description of the TCV is beyond the scope of this work. The interested reader is referred to [74]. Hereafter we will outline only those aspects that are relevant to control. The main parameters of the TCV tokamak are given in Table 8.1.

The TCV was originally constructed to explore the effect of the shape on plasma performance. Figure 8.1 shows a poloidal view of the tokamak. The vessel has an almost rectangular section with a height/width ratio of 3. The TCV is equipped with 16 independently powered shaping coils (E1–E8; F1–F8) distributed around the vessel; this gives the possibility of obtaining a wide range of plasmas: limiter or diverted; centred or up-down asymmetric; circular or elongated. Besides the poloidal field (PF) coils, there are two ohmic heating (OH) coils, whose main aim is to induce the plasma toroidal current. The high number of PF coils which can be used to generate the magnetic field needed to control the plasma, makes the TCV an ideal plant for control purposes. This, together with the growing interest in more sophisticated control algorithms, motivates the replacement of a hybrid analogue–digital system with a PID structure with an entirely new digital plasma control system (DPCS).

These characteristics make the TCV almost unique among the many existing tokamaks in the world. Typically each tokamak has *one* nominal configuration and only small perturbations around it are admissible. Here instead we can have a variety of different plasmas and moreover since the PF coils are distributed all around the chamber they produce different plasma responses.

During the discharges all the data are stored in the TCV database. In this database it is possible to find not only the quantities that are directly measured (*i.e.*, currents, magnetic fields, voltages, *etc.*) but also some reconstructed quantities, which are the outcome of post-process calculations. One of the codes used for these calculations is the inverse equilibrium solver LIUQE [75].

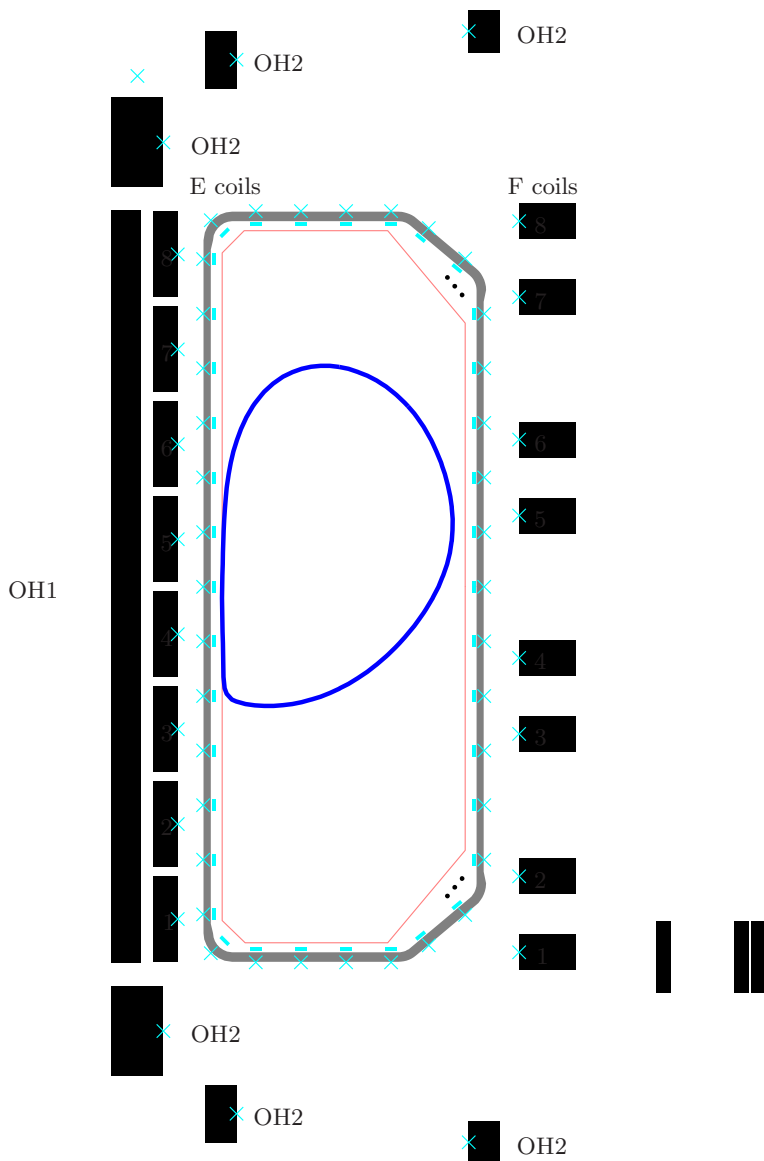


**Figure 8.1.** The TCV vessel and the poloidal field (PF) coils. The magnetic diagnostics are shown as bars (PF probes) and crosses (poloidal flux loops)

### 8.1.1 Magnetic Diagnostics

The unique flexibility of the TCV requires high precision in the magnetic measurements. These measurements are used both for real-time operations (such as, for instance, the feedback control) and for off-line reconstructions.

**Table 8.1.** Main TCV parameters

Plasma height [m]	up to 1.44
Plasma width [m]	up to 0.48
Plasma major radius [m]	0.875
Plasma current [MA]	up to 1.2
Plasma elongation	up to 3
Aspect ratio	3.6
Toroidal magnetic field on the magnetic axis [T]	up to 1.43
Additional heating (ECRH) [MW]	up to 4.5
Transformer flux [Vs]	3.4
Loop voltage [V]	up to 10
Plasma duration [s]	up to 2
Vessel width [m]	0.56
Vessel height [m]	1.54
Vessel ohmic resistance [ $\mu\Omega$ ]	55
Time constant of the vessel [ms]	6.7
Heating temperature [MJ]	up to 350°

The magnetic probes are located inside the vessel at 38 almost evenly spaced positions. They are indicated as bars in Figure 8.1. The poloidal flux loops are located outside the vacuum vessel. They are indicated as crosses in Figure 8.1. All the shaping and ohmic heating coils are equipped with a poloidal flux loop.

Based on these magnetic measurements, it is possible to reconstruct other variables. For instance, the estimate of the plasma current  $I_p$  is obtained with the following line integral

$$I_p = \mu_0 \oint_{\gamma} \mathbf{B} \cdot d\mathbf{l} \simeq \frac{1}{\mu_0} \sum_{i=1}^{38} B_i dl_i \quad (8.1)$$

where  $b_i$  is the magnetic field measured by the  $i$ th magnetic probe and  $dl_i$  indicates the distance between two successive probes. The line  $\gamma$  is chosen close to the vessel, where the probes are mounted.

In an analogous manner, an estimate of the vertical current moment can be obtained in the following way

$$\mu_0 z I_p \simeq \sum_{i=1}^{38} z_i b_i dl_i + \sum_{i=2}^{38} \alpha_i \Delta \psi_i. \quad (8.2)$$

In Equation 8.2  $z_i$  indicates the vertical position of the  $i$ th probe,  $\Delta \psi_i$  are 37 flux-loop differences with respect to the poloidal flux at the vessel midplane, on the inner side; the coefficients  $\alpha_i$  are chosen to minimize the contribution of the poloidal field current to the estimate of  $z I_p$  in the absence of any plasma current.

The key point to note is that both the plasma current  $I_p$ , as in Equation 8.1, and the vertical current moment  $z I_p$ , as in Equation 8.2, are obtained as *linear* combinations of the available flux and field magnetic measurements. Therefore the plasma linearized model, whose outputs are the magnetic fields and fluxes, remains linear also when we consider  $I_p$  and  $z I_p$  as outputs.

### 8.1.2 Description of the Controlled Variables

The TCV offers many possible choices for the variables to control. As we have seen in Section 8.1.1 we have 38 magnetic field and 38 flux measurements. Moreover, all the 18 coil currents are measured. Therefore we have a total of 94 available variables from which to choose. The variables that are usually controlled on the TCV [74] are:

- the plasma current  $I_p$ , evaluated as in Equation 8.1;
- the height of the plasma current centroid with respect to the middle of the vacuum vessel, multiplied by the instantaneous plasma current. This vertical current moment  $z I_p$  is evaluated as in Equation 8.2;
- the inboard–outboard flux imbalance  $P_v$  measured at the midheight of the vacuum vessel, which regulates the radial position of the outer flux surfaces;
- two linear estimators of the separatrix curvature on the inboard and outboard sides of the plasma, respectively,  $Tri_i$  and  $Tri_o$ ; these two parameters are derived from flux and field measurements at  $z = -15$ ,  $z = 0$  and  $z = 15$  cm from the middle of the vacuum vessel, and taken together they regulate the plasma shape.

These five parameters are obtained as linear combinations of the available magnetic measurements. We group them in the vector of the controlled parameters  $c_p$

$$c_p = (I_p \ z I_p \ P_v \ Tri_i \ Tri_o)^T. \quad (8.3)$$

Before a discharge, the following reference signals are fixed

$$I_{pref} \quad z_{ref} \quad \left( \frac{P_v}{I_p} \right)_{ref} \quad \left( \frac{Tri_i}{I_p} \right)_{ref} \quad \left( \frac{Tri_o}{I_p} \right)_{ref}. \quad (8.4)$$

The reason why these are the variables to be controlled is that they have a physical meaning:  $I_p$  is the plasma current, whereas the last four quantities

in (8.4) are related to geometric quantities, such as, for instance, the vertical and radial position of the plasma current centroid. On the other hand, the variables that we can measure are

$$I_p(t) \quad z(t) \cdot I_p(t) \quad P_v(t) \quad Tri_i(t) \quad Tri_o(t). \quad (8.5)$$

For this reason the errors in the last four quantities in (8.3) are constructed multiplying the reference by the *measured* plasma current  $I_p(t)$  and then subtracting the measured value. Therefore the errors are given by

$$\begin{aligned} e_{I_p}(t) &= I_{p_{ref}} - I_p(t) \\ e_{zI_p}(t) &= z_{ref} \cdot I_p(t) - z \cdot I_p(t) \\ e_{P_v}(t) &= \left( \frac{P_v}{I_p} \right)_{ref} I_p(t) - P_v(t) \\ e_{Tri_i}(t) &= \left( \frac{Tri_i}{I_p} \right)_{ref} I_p(t) - Tri_i(t) \\ e_{Tri_o}(t) &= \left( \frac{Tri_o}{I_p} \right)_{ref} I_p(t) - Tri_o(t). \end{aligned} \quad (8.6)$$

These errors are the inputs to the feedback controller.

## 8.2 Design Specifications

As discussed earlier, the design of a current and shape controller for a plasma is a very challenging problem. Some specified performance should be guaranteed, without violating the limits imposed by the actuators.

We decided to use the  $H_\infty$  technique to carry out the design of the current and shape controller. Using this technique, it is possible to specify many different constraints on the desired closed-loop response of the system, guaranteeing at the same time some robustness against plant uncertainties.

In our problem, we have specifications for the plasma response to square pulse references on the controlled parameters with, at the same time, constraints on the bandwidth of the controller, because of the uncertain dynamics of the power supplies, and for the maximum amplitudes of the voltages on the poloidal field coils.

In any case, closed-loop stability is the main requirement for the controller.

### 8.2.1 Controller Robustness

The main concern in the controller design is robust stabilization of the plasma. Since this was the very first attempt at controlling a plasma discharge, even though only during the flat-top, with a multivariable robust controller designed with no experimental tuning, the design had to be rather cautious.

To increase the chance of success, the following set of design goals was chosen to enhance the robustness of the new controller.

- The controller should stabilize the reference plasma, namely a plasma programmed to be offset from the vessel midplane. We also imposed the requirement that similar weakly shaped, symmetric plasmas positioned at the midplane also be stabilized, guaranteeing robustness against variations of the plasma vertical position, since the relative roles of the different poloidal field coils are sensitive to the plasma vertical position. To check this, simulations were performed using plasma models appropriate to these different equilibria. By comparing these different plasma models, we extracted a model of the uncertainty of the “nominal” plasma model we chose for the design.
- The controller must be designed to tolerate uncertainties in the poloidal field coil currents with respect to an equilibrium calculated on the basis of the reference plasma waveforms. Departures of the coil currents from these equilibrium currents should not be compensated, since the poloidal field currents do not have a control error in the sense that they ought to be exactly those programmed. This corresponds to requiring robustness against variations in the precise plasma equilibrium, due to changes in plasma quantities.
- The controller has to be robust to unpredictable behaviour of the poloidal field coil supplies themselves. Although the power supplies can operate in all four quadrants, they have to be instructed to cross zero current at any particular instant. If such a command is not given, crossing does not occur and the power supply appears to be inactive, namely, it shows saturation at zero current. During normal operation, this crossing can be handled, but if a coil current hovers around zero current due to the controller action, the preprogramming of the zero crossing is not correct. The poloidal field coils then appear to have noise on them, not corresponding to the linearized model used to design the controller.
- The controller has to be insensitive to real experimental noise in the control parameter estimators. Data from typical discharges with the noise to be expected were available during controller design.
- The closed-loop bandwidth was allowed to be relatively low to allow for lower power consumption and to minimize any possibility of voltage saturation.

The main design challenge was to demonstrate that the controller could function given real conditions in the tokamak operation not included explicitly in the linearized model.

### 8.2.2 Quantization Errors in the Measurements

A careful analysis of the input signals of the controller from the TCV database (errors between the desired and the measured controlled parameters) showed the presence of quantization errors on the controlled variables.

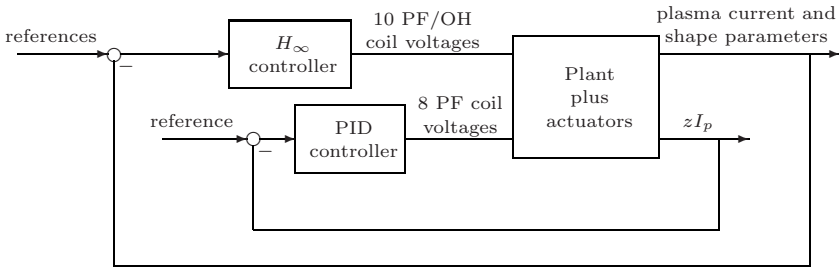


**Figure 8.2.** Block diagram of the closed-loop system

These quantization errors, though not high from a precision point of view, can deteriorate the control signals in the presence of a large controller bandwidth. This is especially true for the vertical position, since, in this case, the controller action must necessarily be *fast*. Therefore this problem must be taken into account in the implementation of the digital controller.

### 8.3 A Solution Based on the $H_\infty$ theory

We decided to set the design of this controller in the  $H_\infty$  framework, trying to guarantee the following:

1. *Nominal Performance*: find a controller  $K(s)$  which internally stabilizes the nominal plant  $P(s)$  and guarantees some closed-loop performance, usually expressed in terms of appropriate weighting matrix functions.
2. *Robust Stability*: find a controller which internally stabilizes not only the nominal plant  $P(s)$  but also all the plants belonging to a specified set  $\Pi$ .

We first describe the plant used for the design and then we detail the method we used to guarantee the closed-loop nominal performance and robust stability. We use the symbol  $\|\cdot\|$  to denote the  $\infty$ -norm of a matrix transfer function, and the symbols  $0_n$  and  $I_n$  to denote the zero and the identity matrices of dimension  $n \times n$ , respectively.

A block diagram of the closed-loop system is shown in Figure 8.2. In Section 6.2 we described the design of the vertical stabilization controller. In the next section we present the design of the  $H_\infty$  compensator for the control of the four parameters

$$I_p(t) \quad P_v(t) \quad Tri_i(t) \quad Tri_o(t).$$



### 8.3.1 Choice of the Plant for the Design

The  $H_\infty$  controller was designed on the basis of the nominal plasma model (a limited plasma shifted about 11 cm above the midplane) already stabilized using a PID controller, as discussed in Section 6.2. This plasma model was augmented, premultiplying it by a block  $10 \times 10$  diagonal matrix function whose diagonal entries have the expressions

$$W_i(s) = \frac{e^{-s\tau_d}}{1 + s\tau},$$

where  $\tau_d$  is the total time delay. There are two main sources of delay:

1. the digital equipment on which the controller should eventually be implemented. This delay includes the conversion time, the transfer time and the calculation time;
2. the conversion to discrete-time that was to be operated after the design.

The delay term  $e^{-s\tau_d}$  was approximated with a second-order Padé term.

The resulting model has more than 80 states; hence it cannot be used directly in the design, since the controller from an  $H_\infty$  design is of the same order as the generalized plant used, that is the nominal plant plus all the weighting matrix functions. Therefore the model needed to be reduced in order. We used a balanced model reduction to reduce the system to 21 states.

This model presents 10 inputs (the PF coils not used by the PID) and four outputs (the other four controlled outputs). We chose to augment this plant adding four more outputs: the integrals of the four controlled parameters. This is one of the ways it is possible to introduce an integral action in the  $H_\infty$  framework.

### 8.3.2 Description of the Weighting Functions

In the attempt to guarantee, besides closed-loop robust stability, the simultaneous satisfaction of the many constraints and specifications, we chose to find a controller  $K(s)$  minimizing the following performance index (Figure 8.3)

$$\sup_{\|\bar{d}\|_2 \leq 1} (\|\bar{e}\|_2^2 + \|\bar{u}\|_2^2 + \|\bar{y}\|_2^2) = \left\| \begin{pmatrix} W_e S_0 W_d \\ W_u K S_0 W_d \\ W_y T_0 W_d \end{pmatrix} \right\|_\infty^2 \quad (8.7)$$

where  $S_0$  is the output sensitivity matrix defined as

$$S_0 = (I + P_\Delta K)^{-1}, \quad (8.8)$$

$T_0$  is the output complementary sensitivity matrix defined as

$$T_0 = (I - S_0) = P_\Delta K (I + P_\Delta K)^{-1} \quad (8.9)$$

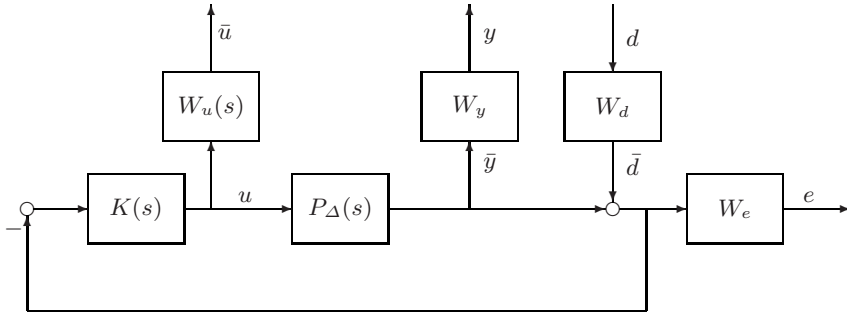


**Figure 8.3.** The closed-loop system augmented with the weighting matrix functions

and  $W_e$ ,  $W_d$ ,  $W_u$  and  $W_y$  are weighting matrix functions used to specify the closed-loop performance. The components of the vector  $y$  are the four controlled parameters. The plant  $P_\Delta$  belongs to a specified set  $\Pi$  (Section 8.3.3).

The performance index (8.7) consists of three terms.

- The first term in Equation 8.7 is the error on the controlled variables due to a disturbance applied at the plant output. The matrix  $W_d$  is a constant diagonal matrix which is used to scale the external disturbance  $w$  acting on the four controlled parameters. These scalars allow the designer to modify the relative weights of the transfer functions between each disturbance and the corresponding controlled parameter. They have been tuned by a trial-and-error procedure.

The matrix  $W_e$ , on the other hand, should ensure the desired performance of the closed-loop system. The variables for which some specifications are assigned are the four controlled parameters. At steady-state these four variables should return to zero even in the presence of a constant disturbance  $w$ . Since we have augmented the plant outputs with the integrals of the four parameters, we can weight both the parameter and their integrals. We choose  $W_e$  as a diagonal constant matrix.

It should be noted that with our choice of the matrices  $W_e$  and  $W_d$ , we also have decoupling among the four variables that we require to control accurately. Indeed if we minimize only the first term in Equation 8.7, these four variables accurately track a reference input at the plant output, with small coupled responses. This is a consequence of the diagonal structure of  $W_e$  and  $W_d$ .

- The second term in Equation 8.7 is used to limit the control bandwidth and amplitude. It is a  $10 \times 10$  diagonal matrix with diagonal terms

$$W_{contr_i}(s) = \frac{K_V}{V_{sat_i}} W_{hp}(s) \quad (8.10)$$

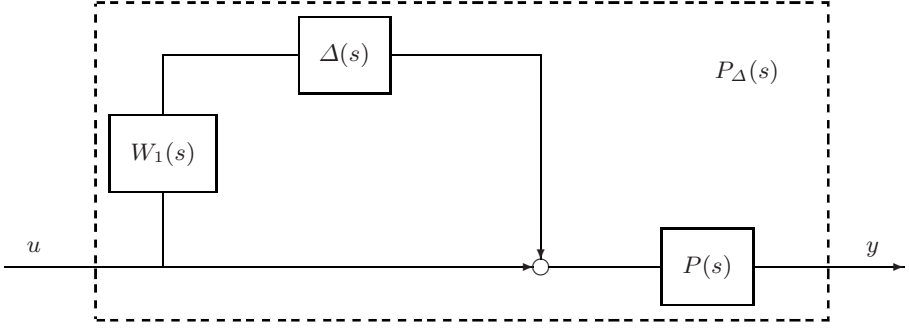


**Figure 8.4.** Structure of the uncertain plant model

where  $K_V$  is a scalar gain,  $V_{sat_i}$  is the maximum control voltage available on coil  $i$  and  $W_{hp}(s)$  is a high-pass filter, with unit gain, used to limit the bandwidth of the controller.

- The third term in Equation 8.7 is used to limit the amplitude of the currents at the output of the plant.  $W_y$  is a diagonal constant matrix whose elements were chosen on the basis of the pre-programmed currents.

### 8.3.3 Robust Stability

To describe the plasma model (plasma plus actuators) the nominal model  $P$  is not sufficient, for at least three reasons:

1. It has been obtained from a particular model of the plasma, whereas the controller is expected to work efficiently during a real discharge. The main problem is that before a shot we are not sure that the equilibrium reached during the experiment will be the same as the pre-programmed equilibrium. These differences must be accounted for in the controller design.
2. It is a reduced order model. Therefore a high frequency error is introduced with respect to the full-order model.
3. The actuator model is approximated and so it introduces another source of plant uncertainty.

For the last two reasons (high frequency neglected dynamics and actuator errors) we decided to model our plant uncertainty through an input unstructured multiplicative uncertainty.

The system model is assumed to belong to the set (Figure 8.4)

$$\Pi = \{P_\Delta = P(\Delta W_1 + I), \Delta \text{ stable}, \|\Delta\|_\infty \leq 1\}, \quad (8.11)$$

where  $W_1(s)$  is a stable matrix function.

It is well known that if a controller  $K$  internally stabilizes the nominal plant  $P$ , then a necessary and sufficient condition for the internal stability for all  $P_\Delta \in \Pi$  is that the following holds

$$\|W_1 T_i\|_\infty \leq 1 \quad (8.12)$$

where  $T_i$  is the input complementary sensitivity matrix defined as

$$T_i = KP(I + KP)^{-1}. \quad (8.13)$$

We chose the matrix function  $W_1(s)$  as a block  $10 \times 10$  diagonal matrix whose generic entry is a first-order high-pass filter. With this matrix we try to capture the uncertainties in the plasma model; it was chosen by comparing the frequency responses of different plasma models.

### 8.3.4 Current and Shape Controller Synthesis

To find a current and shape controller to meet the nominal performance and the robust stability specifications described above, we used the command `hinfsyn` of [76], after rearranging the plant in such a way to exactly fit the  $H_\infty$  framework.

In order to find a satisfactory trade-off among the different specifications, a trial and error tuning of the weighting functions was necessary. These trial and error iterations were carried out by testing the controller on the various plasma configurations, and looking at the performance obtained; the weighting functions were changed on the basis of this analysis. The iterations stopped when a satisfactory compromise was achieved.

In particular, we found that, as expected, there is a trade-off between the speed of response and the amplitude of the transient displacements of the controlled parameters, influenced by the elements of  $W_e$ , and the maximum amplitude of the control voltages, which can be modulated by the weights  $K_V$ .

## 8.4 Simulation Results

The controller designed for the TCV was finally obtained with the following steps:

- The  $H_\infty$  controller was augmented with the integrators which had been added to the plant.
- The PID designed for the vertical stabilization (Section 6.2) and the  $H_\infty$  controller designed for current and shape control were grouped together.
- The controller obtained was converted to discrete-time using the Tustin bilinear approximation [77]. According to the timing specifications, the sampling time was chosen equal to  $T = 100 \mu\text{s}$ .

The resulting controller had 54 states. This digital controller has been tested using simulations carried out including band-limited white noise on the magnetic measurements. The bandwidth of the noise and its variance have been chosen after spectral analysis of experimental data [35].

The simulation results are shown in Figure 8.5. On each of the plots three traces are shown: the reference, the experimental data of a shot with the digital MIMO controller currently working on the TCV plant, and simulation results obtained with the proposed  $H_\infty$  controller. This figure shows a significant enhancement in the decoupling, especially with respect to the plasma shape parameters  $Tri_o$  and  $Tri_i$  and the absence of oscillations on  $zI_p$ . The design targets were met. This performance was actually delivered during TCV operation [36].

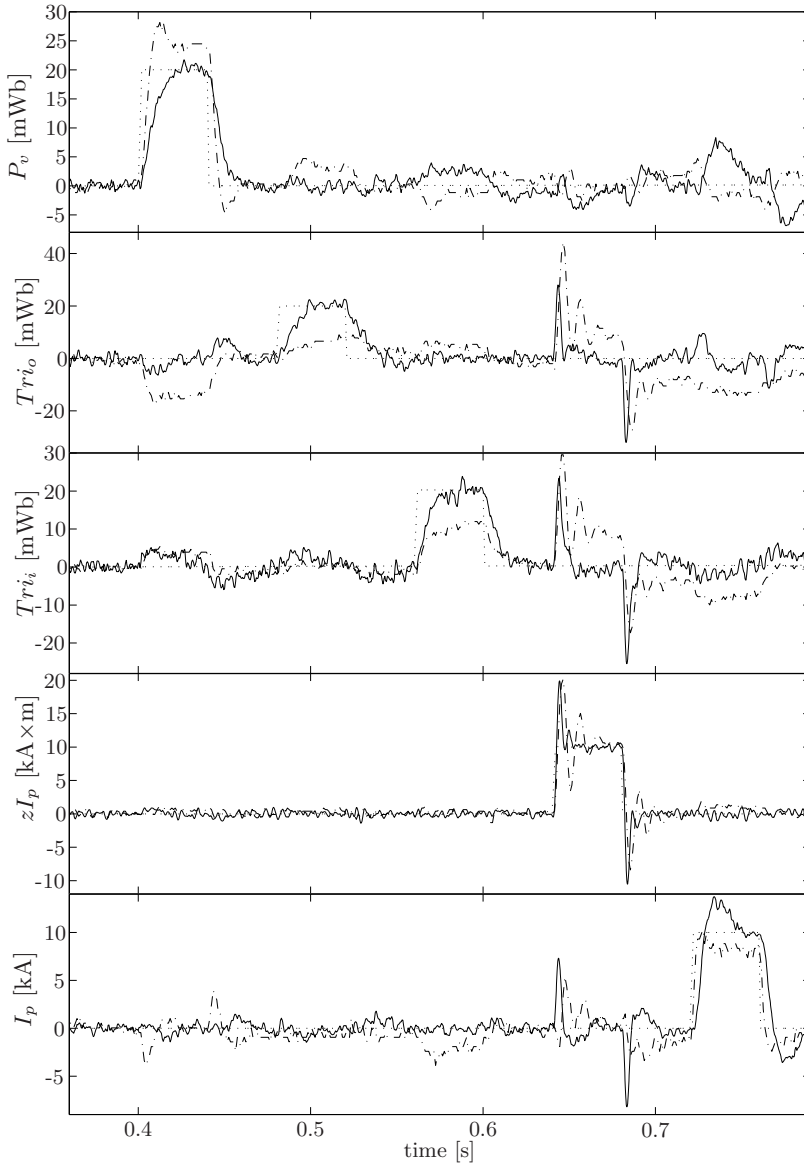


**Figure 8.5.** Comparison between the experimental results of the TCV controller (dash-dot) and simulation results of the proposed controller (solid). The traces of the references to be tracked are plotted dashed.

---

## Plasma Shape Control at JET

The controller design described in this chapter has been carried out in the framework of a project aimed at assessing the possibility of controlling accurately highly elongated plasmas at JET with the existing active circuits and control hardware [78]. One of the steps needed to achieve this objective has been the redesign of the Joint European Torus (JET) shape controller, since the previous controller did not guarantee satisfactory performance. This section describes the features of the new JET controller, which is called the eXtreme Shape Controller (XSC). This new controller is the first example of a multivariable tokamak controller that enables control with high accuracy of the overall plasma boundary, specified in terms of a certain number of gaps. The problem is formulated as an output regulation problem for a non-right-invertible plant, that is a plant in which the number of *independent* control variables is less than the number of *independent* outputs to regulate. In this case it is not possible to guarantee that the difference between the reference and the controlled plant output (*tracking error*) is zero at steady-state. To tackle this problem, we essentially make use of singular value decomposition in order to isolate the part of the plant output that can be better regulated at steady-state. Moreover singular value decomposition gives us an insight into the steady-state control effort: since some of the singular values of the plant static gain are *small*, we truncate these singular values introducing a trade-off between the tracking error and the control effort.

### 9.1 Control Requirements and Simplified Plasma Modelling

JET is the world's largest fusion experiment. It was designed in the 1970s and started operation in 1983. A detailed description of JET and of the results over the first 20 years of research activity can be found in [79]. More recent results are reported in [80]. The main parameters of the JET tokamak are shown in Table 9.1.

**Table 9.1.** Main JET parameters

Major torus radius [m]	2.96
Vacuum vessel [m]	4.2 high, 2.5 wide
Plasma volume [m <sup>3</sup> ]	80–100
Plasma current [MA]	up to 5
Toroidal magnetic field [T]	up to 3.5
Plasma volume [m <sup>3</sup> ]	837
Additional heating [MW]	up to 25

In the JET tokamak (Figure 9.1) there are eight poloidal field coils available to the plasma shape control system. These coils are denoted P1, ..., P4, and D1, ..., D4. The P-coils are connected to form five circuits. The currents flowing in these circuits are indicated by  $I_{P1E}$ ,  $I_{PFX}$ ,  $I_{SHA}$ ,  $I_{P4T}$ ,  $I_{IMB}$ , whereas the currents flowing in the D-coils are indicated by  $I_{Di}$ , with  $i = 1, \dots, 4$ . Therefore we have nine circuits available to the plasma control system. One of these circuits, P1E, is used to control the plasma current, whereas the other eight circuits can be used to control the plasma shape.

The controller we want to design should be able to control the plasma shape. One problem regarding plasma shape control is the choice of controlled variables. In this case the plasma shape has been characterized by a finite number of parameters that are identified on the basis of the available magnetic measurements. More specifically (Figure 9.2), the geometrical parameters controlled by the XSC are a set of 28 gaps all around the vessel, the radial and vertical position of the X-point, and finally two parameters describing the strike point positions. The strike points are the contact points with the tiles in the divertor zone (at the bottom in Figure 9.2). Since the plasma exhaust is taken to the divertor, the tiles are capable of handling high power flux (presently carbon-fibre composites). The strike points with these tiles still need to be carefully controlled.

To sum up, the system we want to control is characterized by the fact that the number of controlled outputs, 32, is much larger than the number of control inputs, eight. As a matter of fact at JET, despite the availability of eight separately powered poloidal circuits available for plasma shape control, there are in fact only five or six (depending on the magnetic configuration of the specific plasma considered) independent degrees of freedom (Figures 9.3 and 9.4).

In this work we have made use of the LTI model described in [81] for the design and assessment of the controller performance through simulations, before implementation on the plant. The model describes the stable part of the plant: the unstable mode is stabilized by means of a separate dedicated



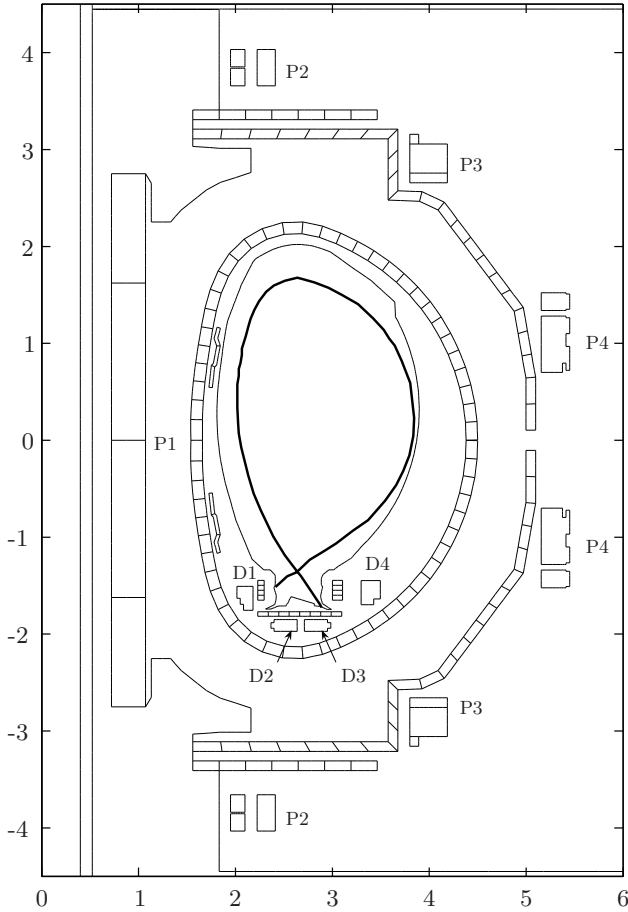


**Figure 9.1.** The JET cross-section. The plasma boundary is shown as a solid line. The poloidal coils (P1–P4 and D1–D4) and the toroidal coils, which surround the plasma ring, produce the necessary confinement magnetic field.

loop. This model can be written in the standard state-space form

$$\begin{aligned}\frac{d}{dt}i &= Ai + Bv \\ y &= Ci,\end{aligned}$$

where  $i$  are the currents in the nine PF coils and in the plasma,  $v$  are the voltages applied to the PF coils, and  $y$  are the 32 controlled shape parameters. The plasma current is controlled using a dedicated SISO loop, by means of a proportional controller that calculates the voltage to apply to the P1E circuit; the other eight circuits are used to control the plasma shape.

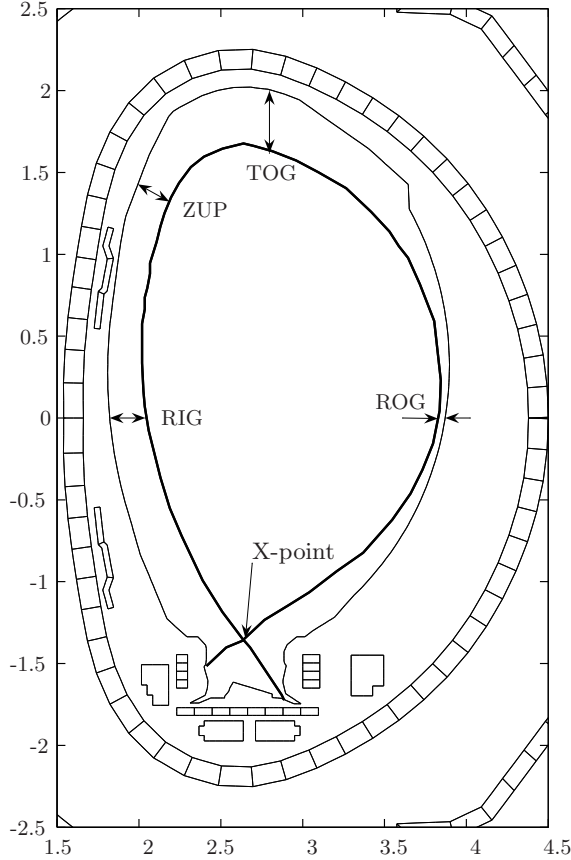


**Figure 9.2.** Some JET gaps. The figure shows some of the gaps defined for the JET control system: RIG is the Radial Inner Gap, TOG is the Top Gap, and ROG is the Radial Outer Gap. A gap is the distance between the plasma surface and the first wall, measured along a given line; this definition simplifies the calculations needed by the plasma shape identification code.

The controller is separated into two parts: the inner loop (*current controller*) is dedicated to the control of the eight PF coils currents, the outer loop (*shape controller*) calculates the PF current that are needed to achieve and maintain a certain shape. This controller structure is motivated by the fact that there are some phases of a discharge, typically in the first time instants, when the control system is required to track some specified current waveforms, rather than guarantee a certain shape. In these cases, the outer loop is simply disconnected and the current references go directly to the current controller. Therefore this separation into two loops can be seen as a requirement for the controller design, rather than a design choice.

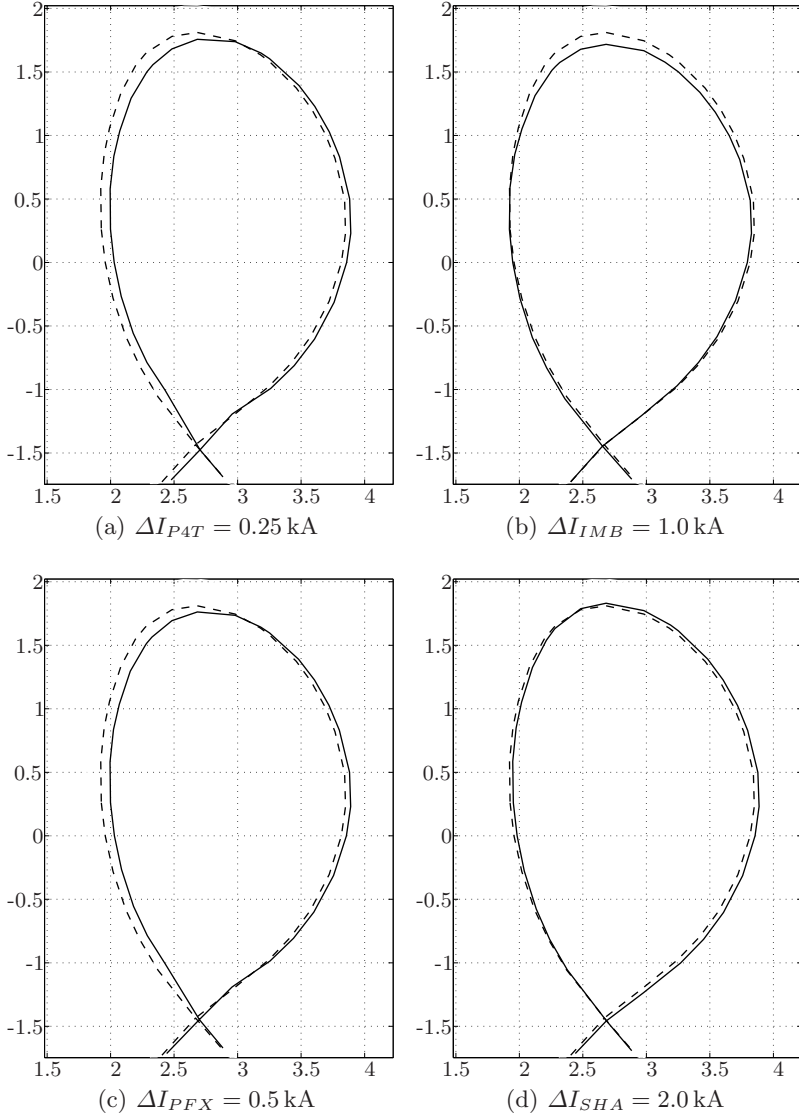


**Figure 9.3.** Plasma shape before (dashed) and after (solid) a current variation in one of the JET poloidal field circuits for  $I_{P4T}$ ,  $I_{IMB}$ ,  $I_{PFX}$  and  $I_{SHA}$ . It is evident that current variations in different coils can cause similar variations in the shape.

The current controller, which is described in detail in [37], guarantees that the transfer matrix between the PF current references and the PF currents is approximately equal to the diagonal matrix  $W(s) = \frac{1}{1+0.1s} I_8$ , where  $I_8$  is the  $8 \times 8$  identity matrix. As a consequence, for the design of the plasma shape

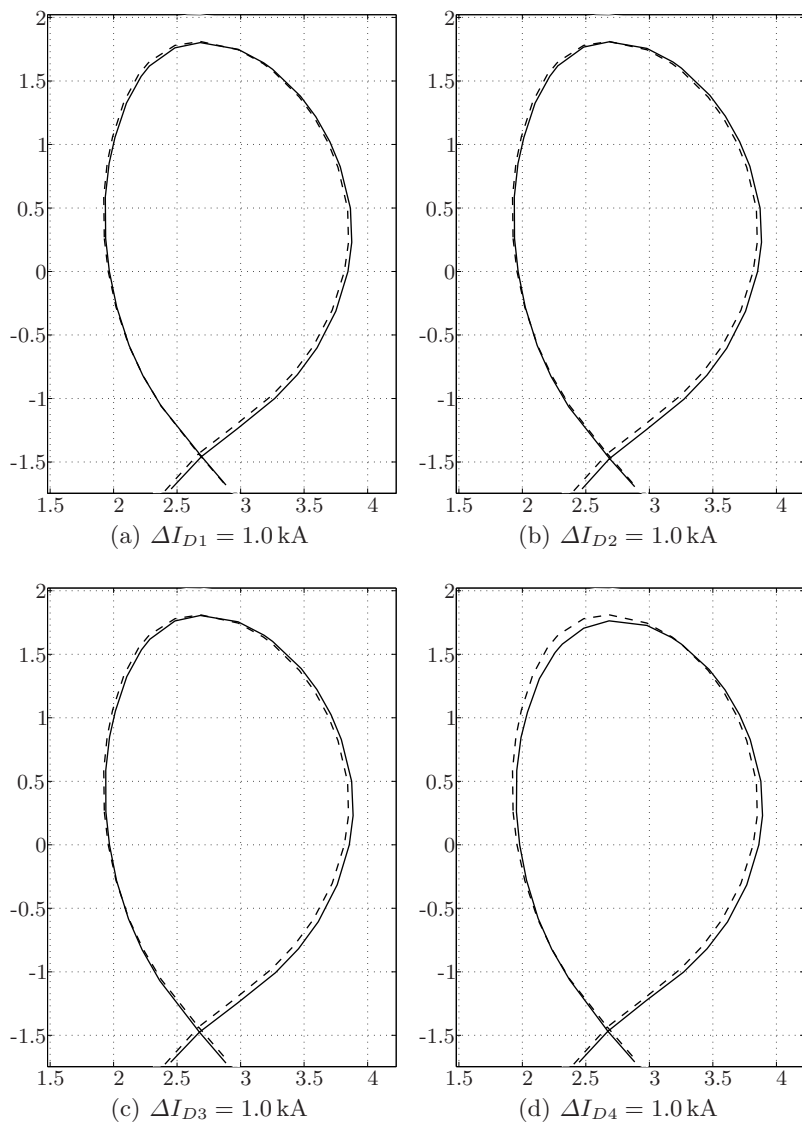


**Figure 9.4.** Plasma shape before (dashed) and after (solid) a current variation in one of the JET poloidal field circuits for  $I_{D1}$ ,  $I_{D2}$ ,  $I_{D3}$  and  $I_{D4}$ . It is evident that current variations in different coils can cause similar variations of the shape.

controller we are reduced to the following linearized simplified model

$$Y(s) = P(s)U(s) \quad (9.1)$$

where  $Y(s)$  are the controlled parameters described in the previous section,  $U(s)$  are the current references for the  $m = 8$  circuits that are available to the shape controller, and

$$P(s) = \frac{C}{1 + s\tau} \quad (9.2)$$

with  $\tau = 0.1$  s, and  $C \in \mathbb{R}^{p \times m}$  with  $p = 32$ . The model (9.1) is the starting point for our controller design.

## 9.2 The Controller Design

### 9.2.1 Requirements and Motivations

The main requirements for the shape control problem that should be guaranteed are the following:

- once a certain desired shape for the plasma boundary is chosen by the physicists, it should be achieved by the feedback controller. In order to specify the required performance, the boundary is divided into five regions (Figure 9.2): the LOG region, the ROG region, the TOG region, the RIG region, the divertor region. In certain regions, the precision is more critical (especially around ROG and the X-point) whereas in other regions a certain tolerance is acceptable (around 2–3 cm);
- the target shape should be maintained also in the presence of “disturbances” acting on the plasma. Typically the amplitude of these disturbances is known in advance and therefore it is possible to evaluate during simulation the effects of the disturbances;
- the PF currents cannot exceed a prescribed range of values; if this happens, the discharges is terminated by what is called a *soft stop*.

The benchmark for the new shape controller was given by the controller previously designed and in operation at JET. This controller [82] was simple in its structure, consisting of a static matrix gain, and guaranteed acceptable performance in most cases. Its main drawback is that it cannot guarantee a specific boundary shape but only control a very few gaps. There are some situations when control of these few gaps is not sufficient to guarantee the overall plasma shape requested by the physicists during experiments. The challenge of the XSC was to guarantee to control as accurately as possible the whole plasma shape with no modification to the existing active circuits and control hardware.

The shape control problem basically consists in determining the circuit currents that minimize the errors in the geometrical descriptors at steady-state. Since we are using  $m$  currents, only  $m$  linear combinations of the geometrical descriptors can be reduced exactly to zero at steady-state. Our problem then becomes that of determining the  $m$  linear combinations of the errors in the geometrical parameters that minimize the overall error in a quadratic sense.

On the other hand, once these  $m$  linear combinations have been selected, the  $m$  values of the control circuit currents at steady-state are univocally determined. Hence this approach could lead to high values of the currents; these values could possibly exceed the saturation limits. To overcome this problem, the number of linear combinations of geometrical descriptor errors to reduce to zero could be chosen to be less than  $m$ . This extra degree-of-freedom can be used to reduce the amplitude of the requested currents.

As a matter of fact, in JET, despite the availability of  $m = 8$  separately powered poloidal coils available for plasma shape control, there are in fact only 5 or 6 (depending on the magnetic configuration of the specific plasma considered) *independent* degrees of freedom.

In the next section, we show how the design problem can be tackled using a singular value decomposition approach. This approach can be cast in the more general framework of regulation for non-right-invertible plants, as shown in [83], where a two-degree-of-freedom control scheme is considered.

### 9.2.2 Optimal Output Regulation

In our control problem we want a constant reference  $\bar{r}$  to be tracked by the controlled output variable  $y(t)$ . We will denote the tracking error by

$$e(t) = \bar{r} - y(t).$$

Let us consider a controller  $K(s)$  with input  $e(t)$  and output  $u(t)$ . Therefore the closed-loop system is specified by the equations (Figure 9.5)

$$y = Pu, \quad u = Ke, \quad e = \bar{r} - y. \quad (9.3)$$

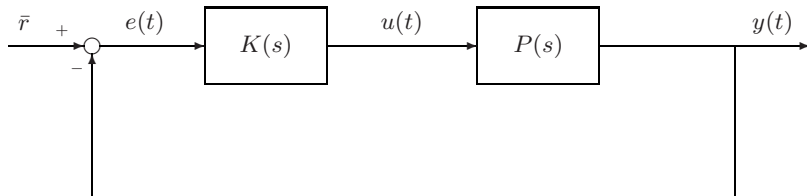


**Figure 9.5.** The feedback scheme

Our aim is to find a controller  $K(s)$  that internally stabilizes the closed-loop system (9.3), and makes the error  $e(t)$  *small* in some sense at steady-state. When some conditions are verified [84, 85], it is possible to have  $e(t) \rightarrow 0$  as  $t \rightarrow +\infty$ ; then a possible choice is to minimize a weighted  $\mathcal{L}_2$ -norm of the error signal [86]. In our case,  $p > m$  (number of output variables to regulate

greater than number of control inputs), and the conditions that allow a zero steady-state error are typically not met. Therefore we consider the problem of minimizing a steady-state performance index in the form

$$J = \lim_{t \rightarrow +\infty} e^T(t) Q e(t), \quad (9.4)$$

where  $Q \in \mathbb{R}^{p \times p}$  is a positive definite weighting matrix.

In general when considering the tracking problem the reference signal  $r$  is supposed to be generated by a so-called exosystem  $\dot{r} = Sr$ . Here we limit our attention to constant references; otherwise, because of the fact that  $p > m$ , the optimal value of the cost function (9.4) could not be definite (that is the limit in (9.4) could not exist or could be unlimited).

Assuming that the controller  $K(s)$  internally stabilizes the closed-loop system (9.3), it is possible to define the following quantities

$$\begin{aligned} \bar{y} &= \lim_{t \rightarrow +\infty} y(t), \\ \bar{u} &= \lim_{t \rightarrow +\infty} u(t), \\ \bar{e} &= \lim_{t \rightarrow +\infty} e(t), \end{aligned}$$

where

$$\bar{e} = \bar{r} - \bar{y} = \bar{r} - C\bar{u}.$$

Let us now consider the singular value decomposition of the following matrix (Equation 9.2)

$$\tilde{C} = Q^{1/2} C R^{-1/2} = U \Sigma V^T, \quad (9.5)$$

where  $\Sigma = \text{diag}(\sigma_1, \sigma_2, \dots, \sigma_m) \in \mathbb{R}^{m \times m}$ ,  $U \in \mathbb{R}^{p \times m}$ ,  $V \in \mathbb{R}^{m \times m}$ , and  $R \in \mathbb{R}^{m \times m}$  is a positive definite weighting matrix.

The two positive definite matrices  $R$  and  $Q$  are introduced to weight the steady-state control effort and tracking error, respectively.

We recall the following properties of the SVD (9.5)

$$V^T V = V V^T = I, \quad (9.6a)$$

$$U^T U = I. \quad (9.6b)$$

The properties of the SVD imply that the columns of the matrix  $Q^{-1/2} U \Sigma$  form a basis for the subspace of the obtainable steady-state output values. The reference signal can be split into two components, one of which lies in this subspace; therefore we can write

$$\bar{r} = Q^{-1/2} U \Sigma \bar{w} + \bar{b}, \quad (9.7)$$

where we let  $\bar{w} \in \mathbb{R}^m$  be given by

$$\bar{w} = \Sigma^{-1} U^T Q^{1/2} \bar{r}. \quad (9.8)$$

From Equations 9.7 and 9.8, making use of Equation 9.6b, it follows that  $\bar{b}$  satisfies

$$U^T Q^{1/2} \bar{b} = 0. \quad (9.9)$$

Now let us decompose the plant output as has been done for the reference (9.7). Therefore let us define

$$z(t) = \Sigma^{-1} U^T Q^{1/2} y(t). \quad (9.10)$$

The signal  $z(t)$  represents the component of the output signal  $y(t)$  that can be actually regulated; it has the same dimension as  $u(t)$ .

Denoting by  $\bar{z}$  the steady-state value of  $z(t)$ , we have

$$\begin{aligned} \bar{z} &= \Sigma^{-1} U^T Q^{1/2} \bar{y} = \Sigma^{-1} U^T Q^{1/2} C \bar{u} \\ &= \Sigma^{-1} U^T U \Sigma V^T R^{1/2} \bar{u} = V^T R^{1/2} \bar{u}, \end{aligned} \quad (9.11)$$

where we have used Equations 9.1, 9.5 and 9.6b. From Equation 9.11, using Equation 9.6a, we obtain

$$\bar{u} = R^{-1/2} V \bar{z}. \quad (9.12)$$

Finally using Equation 9.1 we have

$$\bar{y} = C \bar{u} = Q^{-1/2} U \Sigma V^T R^{1/2} \bar{u} = Q^{-1/2} U \Sigma \bar{z}. \quad (9.13)$$

The decomposition (9.7) has a direct consequence for the cost function (9.4); indeed using Equations 9.7 and 9.13 it is possible to write

$$\bar{e} = \bar{r} - \bar{y} = Q^{-1/2} U \Sigma \bar{w} + \bar{b} - Q^{-1/2} U \Sigma \bar{z}.$$

In this way we obtain

$$\begin{aligned} J &= (\bar{w} - \bar{z})^T \Sigma^2 (\bar{w} - \bar{z}) + \bar{b}^T Q \bar{b} \\ &= \sum_{i=1}^m \sigma_i^2 (\bar{w}^i - \bar{z}^i)^2 + \bar{b}^T Q \bar{b}, \end{aligned} \quad (9.14)$$

where  $\bar{w}^i$  (resp.  $\bar{z}^i$ ) indicate the components of  $\bar{w}$  (resp.  $\bar{z}$ ). The quadratic term involving the vector  $\bar{b}$  in Equation 9.14 does not depend on the choice of the controller, but only on the reference signal  $\bar{r}$  to be tracked. Therefore minimizing  $J$  is equivalent to minimizing the cost function

$$\tilde{J} = (\bar{w} - \bar{z})^T \Sigma^2 (\bar{w} - \bar{z}) = \sum_{i=1}^m \sigma_i^2 (\bar{w}^i - \bar{z}^i)^2. \quad (9.15)$$

Let us imagine for the moment that we are able to design a controller such that the index (9.15) is zero. In this case we would have that

$$\lim_{t \rightarrow +\infty} (\bar{w} - z(t)) = \bar{w} - \bar{z} = 0. \quad (9.16)$$



Making use of Equations 9.12, 9.16 and 9.8 we can calculate the control effort  $\bar{u}$  that we would need at steady-state. It would evaluate to

$$\bar{u} = R^{-1/2} V \bar{z} = R^{-1/2} V \bar{w} = R^{-1/2} V \Sigma^{-1} U^T Q^{1/2} \bar{r}.$$

Therefore the steady-state control effort is related to the smallest singular value  $\sigma_m$  of  $\tilde{C}$  (Equation 9.5) since

$$\max_{\|Q^{1/2}\bar{r}\|=1} \|R^{1/2}\bar{u}\| = \|V \Sigma^{-1} U^T\| = \frac{1}{\sigma_m}. \quad (9.17)$$

It is interesting to note that, once an  $R$  matrix has been fixed, the steady-state value  $\bar{u}$  does not depend on the controller parameters, provided that the index (9.15) is zero. This is a consequence of the fact that we drive to zero a number  $m$  of error linear combinations, which is equal to the number of control inputs, and this can be done in a unique way.

Equation 9.17 shows that if we minimize the cost function (9.15), this can result in unacceptable steady-state values of  $u(t)$ . This is indeed true in our case for the JET tokamak, where an analysis of the singular values showed that  $\sigma_1 > \dots \sigma_k \gg \sigma_{k+1} > \dots \sigma_m$  for  $k = 5$ . As a consequence (see Equation 9.14 and Equation 9.17), if we minimize (9.15) taking into account all of the singular values, we spend a lot of control effort gaining just a little improvement in the value of the cost function. This suggests that we modify the cost function (9.15) neglecting the terms corresponding to the singular values  $\sigma_i$  with  $i > k$  (the smallest ones). In this way we are using just  $k$  linear combinations of the inputs and therefore we can minimize a weighted norm of the steady-state control vector  $\bar{u}$ , since this steady-state value is no longer independent of the controller parameters. To this aim we consider the new cost function (with  $k < m$  terms)

$$\tilde{J}_1 = \sum_{i=1}^k \sigma_i^2 (\bar{w}^i - \bar{z}^i)^2. \quad (9.18)$$

Hence our aim becomes to find a controller structure that solves the following *optimization problem*

$$\min_{\bar{u}} \bar{u}^T R \bar{u} \quad \text{such that } \tilde{J}_1 = 0. \quad (9.19)$$

Let us introduce the following partitions

$$U = (U_1 \ U_2), \quad V = (V_1 \ V_2), \quad \Sigma = \begin{pmatrix} \Sigma_1 & 0 \\ 0 & \Sigma_2 \end{pmatrix},$$

$$z(t) = \begin{pmatrix} z_a(t) \\ z_b(t) \end{pmatrix}, \quad \bar{z} = \begin{pmatrix} \bar{z}_a \\ \bar{z}_b \end{pmatrix}, \quad \bar{w} = \begin{pmatrix} \bar{w}_a \\ \bar{w}_b \end{pmatrix},$$

where  $U_1 \in \mathbb{R}^{p \times k}$ ,  $V_1 \in \mathbb{R}^{m \times k}$ ,  $\Sigma_1 \in \mathbb{R}^{k \times k}$ ,  $z_a(t) \in \mathbb{R}^k$ ,  $\bar{z}_a \in \mathbb{R}^k$  and  $\bar{w}_a \in \mathbb{R}^k$ . Using these partitions, Equations 9.6 become

$$\begin{pmatrix} V_1^T V_1 & V_1^T V_2 \\ V_2^T V_1 & V_2^T V_2 \end{pmatrix} = \begin{pmatrix} I & 0 \\ 0 & I \end{pmatrix}, \quad (9.20a)$$

$$V_1 V_1^T + V_2 V_2^T = I, \quad (9.20b)$$

$$\begin{pmatrix} U_1^T U_1 & U_1^T U_2 \\ U_2^T U_1 & U_2^T U_2 \end{pmatrix} = \begin{pmatrix} I & 0 \\ 0 & I \end{pmatrix}. \quad (9.20c)$$

Our performance index (9.18) can be rewritten as

$$\tilde{J}_1 = (\bar{w}_a - \bar{z}_a)^T \Sigma_1^2 (\bar{w}_a - \bar{z}_a). \quad (9.21)$$

From Equation 9.8 we have that

$$\bar{w}_a = \Sigma_1^{-1} U_1^T Q^{1/2} \bar{r}, \quad (9.22)$$

whereas from Equation 9.10 we have

$$z_a(t) = \Sigma_1^{-1} U_1^T Q^{1/2} y(t). \quad (9.23)$$

Finally making use of Equations 9.1, 9.5 and of 9.20c we have

$$\begin{aligned} \bar{z}_a &= \Sigma_1^{-1} U_1^T Q^{1/2} \bar{y} \\ &= \Sigma_1^{-1} U_1^T Q^{1/2} Q^{-1/2} U \Sigma V^T R^{1/2} \bar{u} \\ &= V_1^T R^{1/2} \bar{u}. \end{aligned} \quad (9.24)$$

Now let

$$u(t) = R^{-1/2} V_1 \tilde{u}(t), \quad (9.25)$$

and

$$K(s) = R^{-1/2} V_1 \tilde{K}(s) \Sigma_1^{-1} U_1^T Q^{1/2}. \quad (9.26)$$

In this way we arrive at the feedback scheme of Figure 9.6.

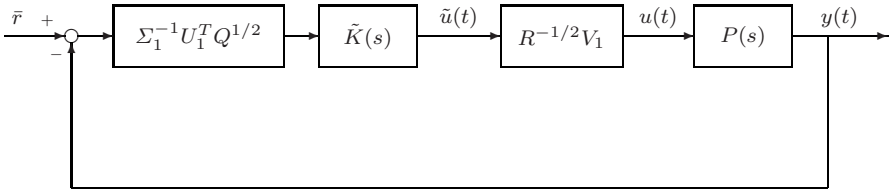


**Figure 9.6.** Feedback scheme with the controller (9.26)

Since we want to track constant references with the smallest possible error, we include an integral action in  $\tilde{K}(s)$ , letting

$$\tilde{K}(s) = \tilde{K}_a(s) + \frac{\tilde{K}_b(s)}{s}, \quad (9.27)$$

so that Equation 9.26 becomes

$$K(s) = R^{-1/2}V_1 \left( \tilde{K}_a(s) + \frac{\tilde{K}_b(s)}{s} \right) \Sigma_1^{-1}U_1^T Q^{1/2}. \quad (9.28)$$

Using Equations 9.22 and 9.23, it is easy to show that the feedback scheme of Figure 9.6 is equivalent to the one shown in Figure 9.7; hence, provided that the closed-loop system is internally stable, the integral action in the controller (9.27) guarantees that

$$\lim_{t \rightarrow +\infty} (\bar{w}_a - z_a(t)) = \bar{w}_a - \bar{z}_a = 0, \quad (9.29)$$

and therefore the performance index  $\tilde{J}_1$  defined in Equation 9.21 is equal to zero.

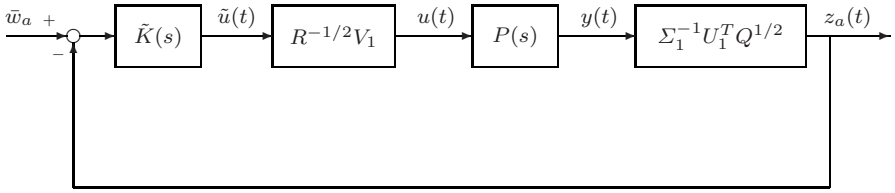


**Figure 9.7.** Feedback scheme equivalent to the one in Figure 9.6

Now let us go back to the solution of the optimization problem (9.19). This problem consists in finding the minimum of  $\bar{u}^T R \bar{u}$  with the constraint that  $\tilde{J}_1 = 0$ .

It is easy to show by standard static optimization techniques that this minimum value, which must satisfy Equation 9.24, is attained when

$$\bar{u} = R^{-1/2}V_1 \bar{w}_a.$$

On the other hand, using the controller structure (9.28)  $\tilde{J}_1 = 0$  and from Equations 9.24 and 9.25, using the fact that  $V_1^T V_1 = I$  (Equation 9.20a) we have

$$\bar{u} = R^{-1/2}V_1 \bar{z}_a.$$

Now note that  $\bar{z}_a = \bar{w}_a$  (Equation 9.29). As a consequence any controller with the structure (9.28), provided that it internally stabilizes the closed-loop system (9.3), solves our optimization problem (9.19).

### 9.2.3 Design of PI Controllers

In the previous section we have shown that any controller with the structure (9.28) solves the optimization problem (9.19), provided that it is an

internally stabilizing controller. Therefore, our last step is the design of a stabilizing controller with the specified structure.

Let us choose  $\tilde{K}(s)$  (Equation 9.27) in the simplified form

$$\tilde{K}(s) = K_P + \frac{K_I}{s},$$

with  $K_P, K_I \in \mathbb{R}^{k \times k}$ . In order to find a convenient choice for  $K_P$  and  $K_I$ , let us evaluate the loop gain transfer matrix  $F(s)$ ; using Equations 9.20a and 9.20c we have

$$\begin{aligned} F(s) &= \Sigma_1^{-1} U_1^T Q^{1/2} P(s) R^{-1/2} V_1 \tilde{K}(s) \\ &= \Sigma_1^{-1} U_1^T Q^{1/2} \frac{Q^{-1/2} U \Sigma V^T R^{1/2}}{1 + s\tau} R^{-1/2} V_1 \tilde{K}(s) \\ &= \Sigma_1^{-1} \begin{pmatrix} I & 0 \\ 0 & \Sigma_2 \end{pmatrix} \begin{pmatrix} I \\ 0 \end{pmatrix} \frac{\tilde{K}(s)}{1 + s\tau} \\ &= \frac{\tilde{K}(s)}{1 + s\tau}. \end{aligned}$$

Therefore exploiting the properties of the singular value decomposition, if we choose  $K_P$  and  $K_I$  as diagonal matrices

$$K_P = \text{diag}(K_{P_1}, \dots, K_{P_k}), \quad K_I = \text{diag}(K_{I_1}, \dots, K_{I_k}),$$

we reduce our problem to  $k$  decoupled SISO problems (Figure 9.8). Since we

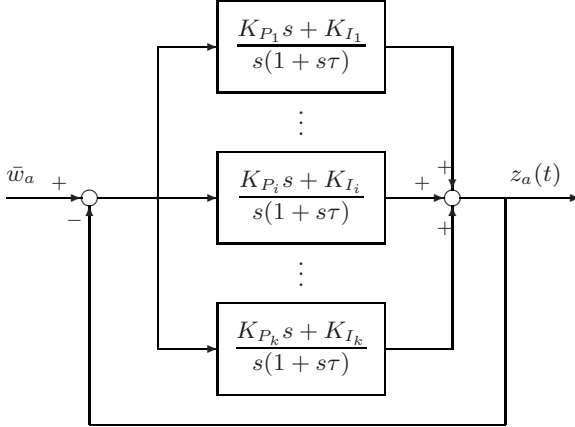


**Figure 9.8.** Decoupled scheme for the PI design

are controlling  $k$  linear combinations of the output  $y(t)$ , the most reasonable choice is to let

$$K_P = k_p I, \quad K_I = k_i I.$$

The values of the two scalars  $k_p$  and  $k_i$  have been chosen so as to assign to each SISO loop the behaviour of a second-order system with a natural frequency of 25 rad/s and a damping factor of 0.7.

### 9.3 Simulation Results

The XSC has been designed to control the plasma shape during the flat-top phase, when the plasma current has a constant magnitude.

Hereafter we show some results that have been obtained in simulations using the XSC. The simulation scheme includes also:

- a model of the reconstruction code XLOC, which is used at JET to calculate the controlled geometrical descriptors starting from the available magnetic measurements; this code introduces quantization at the controlled variables;
- noise on the controlled variables; the characteristics of the noise has been extrapolated by analysing experimental data.

In the simulation we show here, we suppose that the XSC takes control during the plasma flat-top at  $t = 54$  s. The XSC controller is asked to track a certain specified shape. Let us denote

- by  $\bar{r}$  the desired constant reference;
- by  $t_s$  the switching time, that is the time when the reference on the shape is changed;
- by  $t_{tr} = 3$  s a so-called *transition time*;
- by  $y$  the shape geometrical variables we want to regulate.

Then, to avoid large control signals, the shape reference given to the controller is linearly interpolated over  $t_{tr} = 3$  s in the following way

$$r(t) = \begin{cases} y(t_s) + (\bar{r} - y(t_s)) \frac{t - t_s}{t_{tr}} & t_s \leq t \leq t_s + t_{tr} \\ \bar{r} & t > t_s + t_{tr} \end{cases}$$

Figure 9.9 shows the reference shape and the shape obtained in simulation with the XSC: the shape is reached with a small steady-state error. Figure 9.10 shows the average value of the error on the 32 controlled gaps, evaluated as

$$e(t) = \frac{\|\bar{r} - y(t)\|_1}{32} \quad 54 \leq t \leq 61$$

where  $\bar{r}$  denotes the constant reference shape. As can be seen, initially, when the XSC is switched on, at  $t = 54$  s the mean error is about 8 cm, then the XSC reduces this error to less than 2 cm in about 3 s (the transition time

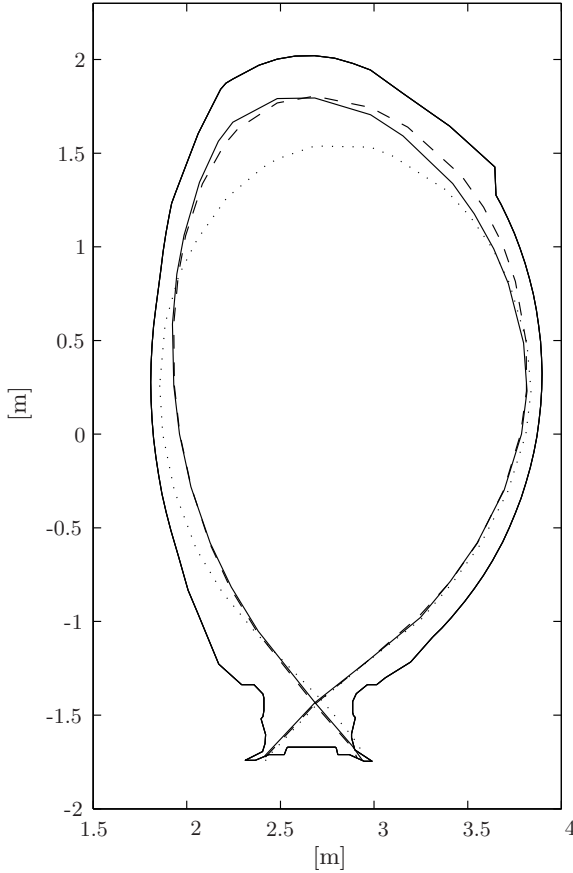


**Figure 9.9.** Simulation results using the XSC : the switching time is  $t_s = 54$  s and the transition time  $t_{tr} = 3$  s. The figure shows: (i) the reference shape to be tracked (dashed); (ii) the plasma boundary at  $t = 54$  s (dotted); (iii) the plasma boundary at  $t = 57$  s (solid).

interval). Figure 9.11 shows the tracking results for the two gaps ROG and TOG, and for the radial and vertical position of the X-point (Figure 9.2).

In 2003 the XSC was implemented at JET and it is currently in operation. It has been implemented on a 400 MHz G4 PowerPC; the controller software architecture has been designed so that it enables testing of all the software off-line, since at JET long commissioning periods are not available. It is used in all the experiments where accurate control of the plasma shape is needed. During a single experiment the XSC can be used to obtain different plasma shapes. In particular, at JET, the whole experimental pulse is divided into a number of time segments, called *time windows*. With a different plasma shape

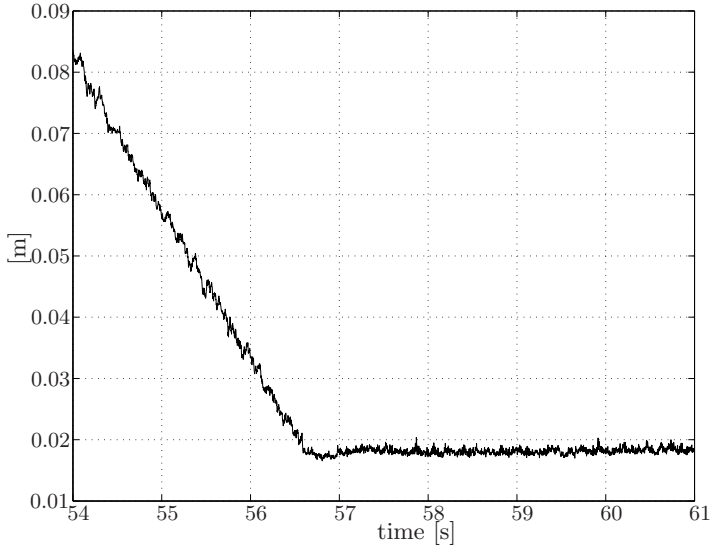


**Figure 9.10.** Simulation of the XSC: the average error on the 32 controlled shape variables when using the XSC

reference for each time window, the XSC guarantees transition between the different shapes [38].

The XSC has been successfully used also in the presence of injection of heating power to the plasma. These injections act as disturbances to the shape, that, without adequate feedback control, would change. The XSC has been able to counteract these disturbances, rejecting them, and keeping the shape almost unchanged.

Modified versions of the XSC have also been designed and implemented at JET to tackle specific control problems: strike-point sweeping and boundary flux control. Strike point sweeping is the movement of the plasma strike points, in the lower region of the vessel, at a prescribed frequency, to avoid excessive heat in that region. During sweeping, the plasma boundary is maintained almost fixed except for the movements in the strike point region [39]. The plasma boundary flux control is used on tokamaks with the aim of increasing the fraction of plasma current supplied by noninductive means. This is a crucial step for steady-state operation in future devices since if the plasma flux is kept constant, then all of the plasma current is induced by the additional heating and current drive devices available on the tokamak. The paper [40] describes the way the plasma flux control has been implemented at JET using a modified version of the XSC.

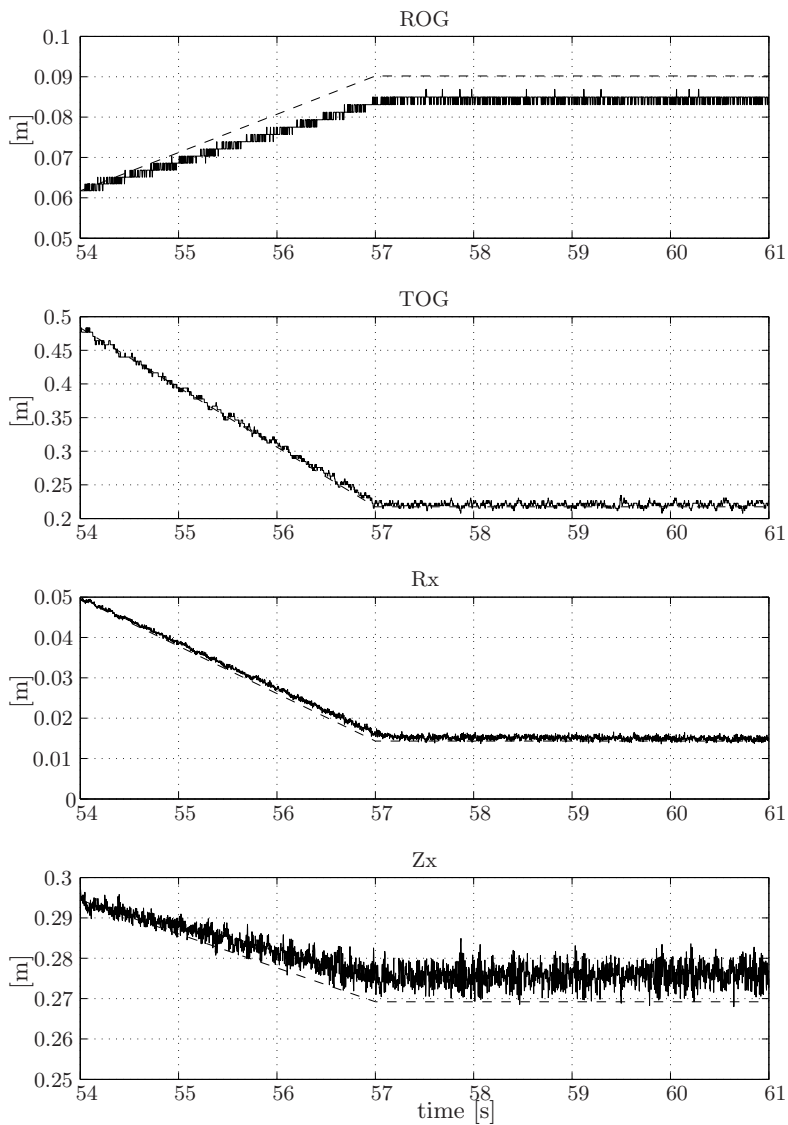


**Figure 9.11.** Simulation results of the XSC: the behaviour of two gaps and of the X-point while using the XSC. From the top to the bottom: ROG, TOG, the radial and the vertical position of the X-point. The simulated traces are solid, the references are dotted.



# A

---

## Some Mathematical Background

### A.1 Green's Functions for the Homogeneous Grad-Shafranov Equation

The material covered in this section can be found in many advanced calculus book, however we prefer to cite the classic book by Morse and Feshbach [87].

The  $\Delta^*$  operator introduced in Chapter 2 plays an important role in determining the plasma equilibrium. In particular, given the toroidal current density, the poloidal flux function can be determined by solving the partial differential Equation 2.15. Analytical solutions for this equation can be found with the aid of Green's function method. Consider the generalized partial differential equation

$$\Delta^* G(\mathbf{r}, \tilde{\mathbf{r}}) = -\mu_0 r \delta(\mathbf{r} - \tilde{\mathbf{r}}), \quad (\text{A.1})$$

where  $\delta$  is the Dirac function, and the operator  $\Delta^*$  is applied with respect to the  $\mathbf{r}$  variable. If boundary conditions are not specified, the solutions of Equation A.1 are infinite, differing from each other by a function  $\chi$  solving the homogenous equation  $\Delta^* \chi = 0$ . It can be shown by using Green's third identity that given a Green's function and assigning Dirichlet and Neumann type boundary conditions on a domain  $D$  for the poloidal flux function, the solution of Equation 2.15 can be expressed as

$$\begin{aligned} \psi(\mathbf{r}) = & \int_D G(\mathbf{r}, \tilde{\mathbf{r}}) J_\varphi(\tilde{\mathbf{r}}) d\tilde{S} \\ & - \oint_{\partial D} \frac{1}{\mu_0 \tilde{r}} \left( \psi(\tilde{\mathbf{r}}) \frac{\partial}{\partial n} G(\mathbf{r}, \tilde{\mathbf{r}}) - G(\mathbf{r}, \tilde{\mathbf{r}}) \frac{\partial}{\partial n} \psi(\tilde{\mathbf{r}}) \right) d\tilde{l}. \end{aligned} \quad (\text{A.2})$$

Hence Equation A.2 allows us to evaluate the poloidal flux function inside a domain  $D$  if a Green's function  $\psi$  and  $\frac{\partial \psi}{\partial n}$  on  $\partial D$  are given. Note that if a Green's function satisfies a homogeneous Neumann condition on  $\partial D$  then Dirichlet conditions on  $\psi$  are sufficient to evaluate the poloidal flux function.

On the other hand if Green's function satisfies a homogeneous Dirichlet condition then just Neumann conditions on  $\psi$  have to be assigned. It is interesting to note that of the two terms that appear on the right-hand side of Equation A.2 the former one represents the contribution given to the  $\psi$  function by the toroidal current density inside the domain  $D$ , while the latter term represents the contribution to the  $\psi$  function given by the toroidal current density external to the domain  $D$ . Allowing the  $D$  domain to cover the whole poloidal plane and imposing the following boundary conditions on Green's function

$$\begin{aligned} \lim_{\mathbf{r} \rightarrow \infty} G(\mathbf{r}, \tilde{\mathbf{r}}) &= 0 \quad \text{if } \|\tilde{\mathbf{r}}\| < M \in \mathbb{R} \\ \lim_{\mathbf{r} \rightarrow 0} G(\mathbf{r}, \tilde{\mathbf{r}}) &= 0 \quad \text{if } \|\tilde{\mathbf{r}}\| > M \in \mathbb{R} - \{0\}, \end{aligned}$$

one obtains the so-called free space Green's function  $G_0$ . For the free space, Green's function Equation A.2 reduces to

$$\psi(\mathbf{r}) = \int_{\mathbb{R}^2} G_0(\mathbf{r}, \tilde{\mathbf{r}}) J_\varphi(\tilde{\mathbf{r}}) d\tilde{\mathbf{r}}. \quad (\text{A.3})$$

The function  $G_0$  represents the flux produced by an infinitesimal toroidal filament carrying a unitary current; the analytical expression for  $G_0$  is

$$\begin{aligned} G_0(\mathbf{r}, \tilde{\mathbf{r}}) &= \mu_0 \frac{\sqrt{r\tilde{r}}}{\pi k} \left[ \left( 1 - \frac{k^2}{2} \right) K(k^2) - E(k^2) \right] \\ &= \mu_0 \frac{\sqrt{r\tilde{r}}}{\pi k} \left[ \frac{1}{3} R_D(0, 1 - k^2, 1) - \frac{1}{2} R_F(0, 1 - k^2, 1) \right], \end{aligned} \quad (\text{A.4})$$

where

$$k^2 = \frac{4r\tilde{r}}{(r + \tilde{r})^2 + (z - \tilde{z})^2}.$$

The functions  $K$  and  $E$  are the elliptic integral of the first and second kind respectively [88]. The functions  $R_F$  and  $R_D$  have been introduced by Carlson [89] and enable one to evaluate (A.4) with better accuracy (see also [90]).

## A.2 Solutions of the Homogeneous Grad–Shafranov Equation

The homogeneous Grad–Shafranov equation

$$\Delta^* \psi = 0 \quad \Longleftrightarrow \quad r \frac{\partial}{\partial r} \left( \frac{1}{r} \frac{\partial}{\partial r} \psi \right) + \frac{\partial^2}{\partial z^2} \psi = 0 \quad (\text{A.5})$$

plays an important role in the plasma shape identification algorithms discussed in Chapter 3. In particular, its solutions in the not simply connected set  $\Omega_v$  are used to obtain an approximation of the poloidal flux function fitting the available magnetic measurements.

### A.2.1 Green's Functions

The Green's functions have been defined in Section A.1; from Equation A.1 it is evident that a Green's function  $G(\mathbf{r}, \tilde{\mathbf{r}})$  satisfies the homogeneous Grad-Shafranov equation everywhere except at the point  $\tilde{\mathbf{r}}$  where the impulsive source is located. A Green's function is, thus, a solution of Equation (A.5) in  $\Omega_v$  if  $\tilde{\mathbf{r}} \notin \Omega_v$ .

### A.2.2 Toroidal Harmonics

A toroidal coordinate system  $(\eta, \zeta, \varphi)$  is defined with respect to the cylindrical coordinate system  $(r, z, \varphi)$  introduced in Section 2.2 by the relations [87, 91]

$$r = \frac{r_0 \sinh(\zeta)}{\cosh \zeta - \cos \eta} \quad (\text{A.6})$$

$$z = \frac{r_0 \sin \eta}{\cosh \zeta - \cos \eta} + z_0 \quad (\text{A.7})$$

where  $\mathbf{r}_0 = (r_0, z_0)$  is the position on the poloidal plane of the singular point ( $\zeta = +\infty$ ) of the toroidal coordinate system.

In a toroidal coordinate system Equation A.5 is written as

$$\frac{\cosh \zeta - \cos \eta}{r_0} \left[ \sinh \zeta \frac{\partial}{\partial \zeta} \left( \frac{\cosh \zeta - \cos \eta}{r_0} \frac{\partial}{\partial \zeta} \psi \right) + \frac{\partial}{\partial \eta} \left( \frac{\cosh \zeta - \cos \eta}{r_0} \frac{\partial}{\partial \eta} \psi \right) \right] = 0. \quad (\text{A.8})$$

Analytical solutions to the partial differential Equation A.8 can be found using the variable separation method. Let

$$\psi(\eta, \zeta) = \frac{r_0 \sinh \zeta}{\sqrt{\cosh \zeta - \cos \eta}} h(\zeta) g(\eta); \quad (\text{A.9})$$

by substituting Equation A.9 in A.8 one obtains the two *separated* equations

$$\frac{1}{\sinh \zeta} \frac{\partial}{\partial \zeta} \left( \sinh \zeta \frac{\partial}{\partial \zeta} h \right) - \frac{1}{\sinh^2 \zeta} h - \left( \lambda^2 - \frac{1}{4} \right) h = 0 \quad (\text{A.10a})$$

$$\frac{\partial^2}{\partial \eta^2} g + \lambda^2 g = 0, \quad (\text{A.10b})$$

where  $\lambda$  is the separation constant. Due to the fact that the coordinate  $\eta$  represents an angle, the function  $g$  must be periodic at  $2\pi$ . From Equation A.10b it follows that  $\lambda^2$  must be an integer. Moreover, with the change of variable  $s = \cosh \zeta$  it is possible to show that Equation A.10a becomes the Legendre differential equation [88, 87]. From these considerations we obtain a pair of linearly independent solutions for each of the Equations A.10

$$h_1(\zeta) = P_{n-\frac{1}{2}}^1(\cosh \zeta) \quad (\text{A.11a})$$

$$h_2(\zeta) = Q_{n-\frac{1}{2}}^1(\cosh \zeta) \quad (\text{A.11b})$$

$$g_1(\eta) = \cos(n\eta) \quad (\text{A.11c})$$

$$g_2(\eta) = \sin(n\eta), \quad (\text{A.11d})$$

where  $n = \lambda^2$  and  $P_\beta^\alpha$ , and  $Q_\beta^\alpha$  are the grade  $\alpha$  and order  $\beta$  *associate Legendre function* of first and second kind, respectively [88, 92]. With the aid of the functions defined in Equations A.11 the following set of solutions to (A.5) are obtained

$$\psi_{\text{int},n}^c(\eta, \zeta) = \frac{r_0 \sinh \zeta}{\sqrt{\cosh \zeta - \cos \eta}} P_{n-\frac{1}{2}}^1(\cosh \zeta) \cos(n\eta) \quad (\text{A.12a})$$

$$\psi_{\text{int},n}^s(\eta, \zeta) = \frac{r_0 \sinh \zeta}{\sqrt{\cosh \zeta - \cos \eta}} P_{n-\frac{1}{2}}^1(\cosh \zeta) \sin(n\eta) \quad (\text{A.12b})$$

$$\psi_{\text{ext},n}^c(\eta, \zeta) = \frac{r_0 \sinh \zeta}{\sqrt{\cosh \zeta - \cos \eta}} Q_{n-\frac{1}{2}}^1(\cosh \zeta) \cos(n\eta) \quad (\text{A.12c})$$

$$\psi_{\text{ext},n}^s(\eta, \zeta) = \frac{r_0 \sinh \zeta}{\sqrt{\cosh \zeta - \cos \eta}} Q_{n-\frac{1}{2}}^1(\cosh \zeta) \sin(n\eta). \quad (\text{A.12d})$$

It is possible to give a physical meaning to the functions defined in Equations A.12, which are called toroidal harmonics. In particular, the functions  $\psi_{\text{int},n}^c$  ( $\psi_{\text{int},n}^s$ ) give the poloidal flux produced by a toroidal current multipole of order  $2n$ ; the multipole is located at the point  $\mathbf{r}_0$  and is arranged in such a way that it produces a symmetric (antisymmetric) flux with respect to the  $z = z_0$  line. The functions  $\psi_{\text{ext},n}^c$  ( $\psi_{\text{ext},n}^s$ ) give the flux produced by a current multipole located at the point  $(0, z_0)$  of the poloidal plane. It is therefore clear that the functions (A.12) solve the homogeneous Grad–Shafranov equation everywhere in the poloidal plane except at the points  $(r_0, z_0)$  and  $(0, z_0)$ . The level line of some such functions are shown in Figure A.1 and A.2. Assuming that the singular points  $(r_0, z_0)$  and  $(0, z_0)$  do not belong to  $\Omega_v$  it is possible to show that the toroidal harmonics constitute a complete set of solution of Equation A.5 so that each solution of this equation can be written as

$$\psi = \sum_{n=0}^{\infty} [a_n^c \psi_{\text{int},n}^c + a_n^s \psi_{\text{int},n}^s + b_n^c \psi_{\text{ext},n}^c + b_n^s \psi_{\text{ext},n}^s] . \quad (\text{A.13})$$

Note that if the point  $(r_0, z_0)$  is located in the plasma region  $\Omega_p$  the first two terms in the summation (A.13) represent the flux produced by the current distribution in the plasma, while the last two terms represent the flux produced by the current distribution outside the  $\Omega_v$  region.

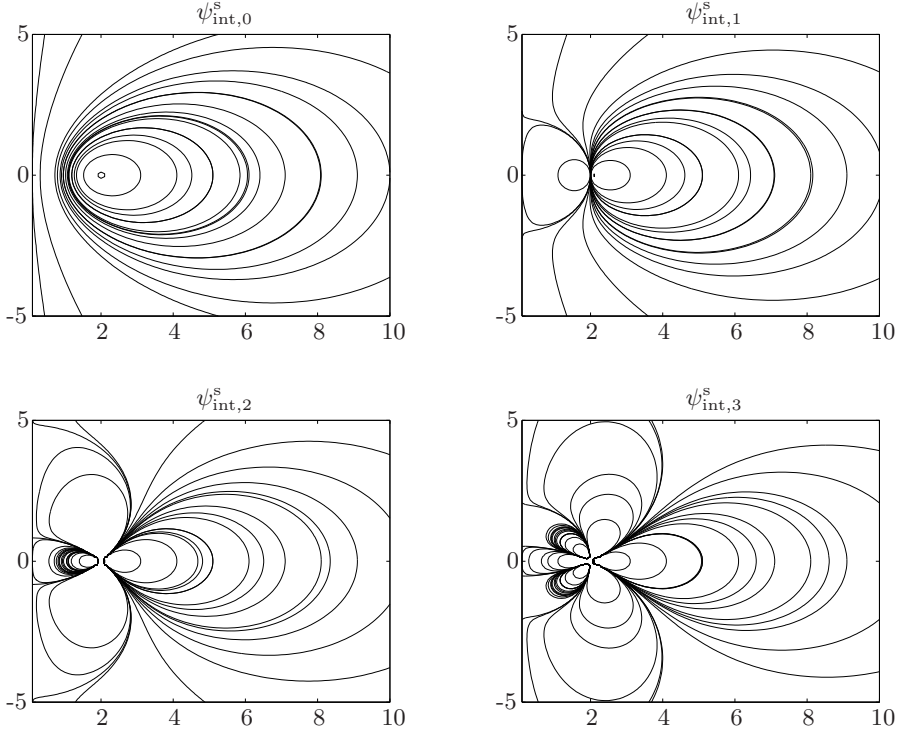


**Figure A.1.** Level lines of some toroidal harmonics of internal type, with  $r_0 = 2, z_0 = 0$

### A.3 Ill-posedness and Plasma Shape Identification Problem

From a mathematical point of view, estimation of the plasma boundary is the problem of evaluating the function  $\psi$ , satisfying Equation 3.14, with certain boundary conditions given on the measurement contour  $\Gamma_m$  (Section 3.4). These boundary conditions can be of Dirichlet type (when flux sensors are used)

$$\psi(\mathbf{r}_m) = f_m, \quad \mathbf{r}_m \in \Gamma_m, \quad (\text{A.14})$$

or they can be of Neumann type (when tangential magnetic field sensors are used)

$$-\frac{\partial}{\partial z} \psi(\mathbf{r}_m) \cos(\theta_m) + \frac{\partial}{\partial r} \psi(\mathbf{r}_m) \sin(\theta_m) = r_m f_m, \quad (\text{A.15})$$

where the angle  $\theta_m$  individuates, with respect to the radial axis, the direction of the tangent in  $\mathbf{r}_m$ . From Equation 2.8, it is simple to recognize that the right-hand side of Equation A.15 is the normal (with respect to  $\Gamma_m$ ) derivative of the  $\psi$  function, so that this equation can also be written as

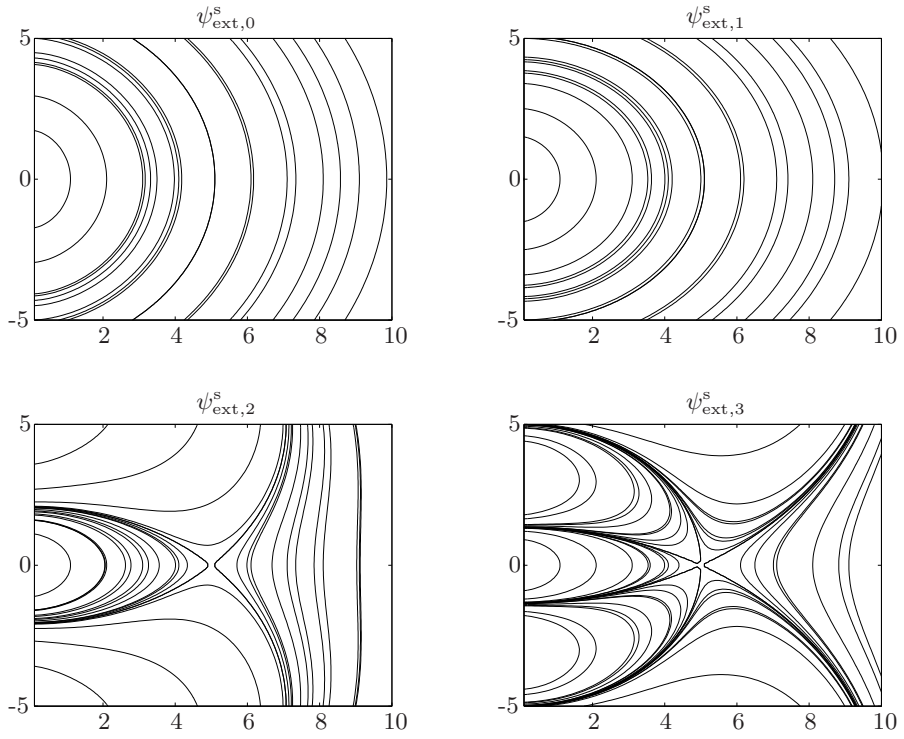


**Figure A.2.** The level lines of some toroidal harmonics of external type, with  $r_0 = 2$ ,  $z_0 = 0$

$$\frac{\partial}{\partial n} \psi(\mathbf{r}_m) = r_m f_m. \quad (\text{A.16})$$

Following the arguments in Chapter 6 of [87], and considering that (3.14) is an elliptic equation, it results that if  $\Gamma_m$  is an open contour, neither Dirichlet nor Neumann conditions are sufficient to univocally determine the function  $\psi$ . On the other hand the knowledge of both the values of  $\psi$  and of its normal derivative  $\partial\psi/\partial n$  (giving rise to a Cauchy problem for Equation 3.14) enables one to determine  $\psi$ ; unfortunately in this case the solution will not depend continuously on the boundary data (in other words the solution is unstable). But even if  $\Gamma_m$  is a closed contour, the plasma shape identification problem remains a difficult mathematical problem; indeed for an elliptic equation, with boundary conditions given on a closed contour, Dirichlet or Neumann conditions are sufficient to unambiguously determine the solution, if the domain where the equation must be satisfied is simply connected. This is not the case for the problem under consideration, where the domain of validity of Equation 3.14 is a doughnut shaped area surrounding the plasma (Figure 3.5). Taking also into account that in a realistic situation the condi-

tions of Equations A.14 and A.16 are not given at all points of  $\Gamma_m$  but only at a finite number of points (where the magnetic sensors are located), it is possible to conclude that the problem of identification of the plasma shape from the magnetic measurements is, as defined by Hadamard [93], an ill-posed problem. This is not surprising since this is often the case in inverse problems like the one under consideration. The book [55] is a good reference for this kind of problem; concerning the plasma shape identification problem, a viable solution is a procedure based on representing the flux function through a truncated Fourier expansion as detailed in Section 3.4.

B

Units Used in Plasma Physics

In this chapter we summarize the dimensions of the most common quantities involved in the electromagnetic and plasma physics fields (Table B.2). We refer to the International System (SI) nomenclature, which is based on the units reported in Table B.1.

Table B.1. The International System (SI) base units

Physical Quantities	Symbol for Quantities	Name of Unit	Symbol for Unit
Length	$l$	metre	m
Mass	$m$	kilogram	kg
Time	$t$	second	s
Current	$I, i$	ampere	A
Temperature	$T$	kelvin	K
Amount of substance		mole	mol
Luminous intensity		candela	cd



**Table B.2.** Units of some physical quantities encountered in plasma physics. Dimensions are expressed in SI base units where  $l$  = length in metres,  $m$  = mass in kg, and  $t$  = time in seconds.

Physical Quantity	Symbol	Dimensions	SI units	Comment
Capacitance	$C$	$\frac{t^2 q^2}{ml^2}$	farad (F)	
Charge	$q$	$\frac{q}{q}$	coulomb (C)	
Charge density	$\rho$	$\frac{q}{l^3}$	C/m <sup>3</sup>	
Conductance		$\frac{tq^2}{ml^2}$	siemens (S)	
Conductivity	$\sigma$	$\frac{tq^2}{ml^3}$	S/m	
Current	$I, i$	$\frac{q}{t}$	ampere (A)	
Current density	$\mathbf{J}, \mathbf{j}$	$\frac{q}{l^2 t}$	A/m <sup>2</sup>	
Displacement	$\mathbf{D}$	$\frac{q}{l^2}$	C/m <sup>2</sup>	$\mathbf{D} = \epsilon \mathbf{E}$
Electric field	$\mathbf{E}$	$\frac{ml}{t^2 q}$	V/m	
Energy	$U, W$	$\frac{ml^2}{t^2}$	joule (J)	electronvolt (eV) is also used; 1eV $\simeq$ 1.60 $\times$ 10 <sup>-19</sup> J
Inductance	$L$	$\frac{ml^2}{q^2}$	henry (H)	
Magnetic intensity	$H$	$\frac{q}{lt}$	A/m	$\mathbf{B} = \mu \mathbf{H}$
Magnetic flux	$\phi, \psi$	$\frac{ml^2}{tq}$	weber (Wb)	$\psi = \int_S \mathbf{B} \cdot d\mathbf{S}$
Magnetic induction	$\mathbf{B}$	$\frac{ml}{tq}$	tesla (T)	gauss (G) is also used; 1G = 10 <sup>-4</sup> T
Permeability	$\mu$	$\frac{ml}{q^2}$	H/m	In plasma $\mu \simeq \mu_0 = 4\pi \times 10^{-7}$ Hm <sup>-1</sup>
Permittivity	$\epsilon$	$\frac{t^2 q^2}{ml^3}$	F/m	In plasma $\epsilon \simeq \epsilon_0 = 8.8542 \times 10^{-12}$ Fm <sup>-1</sup>
Potential	$V$	$\frac{ml^2}{t^2 q}$	volt (V)	
Power	$P$	$\frac{ml^2}{t^3}$	watt (W)	
Resistance	$R$	$\frac{ml^2}{tq^2}$	ohm ( $\Omega$ )	
Resistivity	$\eta, \rho$	$\frac{ml^3}{tq^2}$	$\Omega$ m	
Magnetic vector potential	$\mathbf{A}$	$\frac{ml}{tq}$	Wb/m	$\mathbf{B} = \nabla \times \mathbf{A}$

---

## References

1. Chen F.F. (1974) Introduction to Plasma Physics. Plenum Press, New York
2. Wesson J. (1987) Tokamaks. Oxford Engineering Science Series. Clarendon Press, Oxford
3. Weisz P.B. (2004) Basic choices and constraints on long-term energy supplies. *Physics Today* 57:47–52
4. Sheffield J. (1994) The physics of magnetic fusion reactors. *Reviews of Modern Physics* 66:1015–1103
5. Glasstone S., Lovberg R. (1960) Controlled Thermonuclear Reactions. D. Van Nostrand Company, Inc., Princeton, New Jersey
6. Huba J.D. (2007) NRL Plasma Formulary. Naval Research Laboratory Report NRL/PU/6790–07-500. Washington DC
7. The JET team. (1992) Fusion energy production from a deuterium-tritium plasma in the JET tokamak. *Nuclear Fusion* 32:187–203
8. Ishida S. (1999). JT-60U high performance regimes. *Nuclear Fusion* 39:1211–1226
9. Lawson J.D. (1957) Some Criteria for a Power Producing Thermonuclear Reactor. *Proceedings of the Physical Society B* 70:6–10
10. Freidberg J.P. (1987) Ideal Magnetohydrodynamics. Plenum Press, New York
11. Lackner K., Macmahon A.B. (1974) Numerical study of displacement instability in elongated tokamak. *Nuclear Fusion* 14:575–577
12. Lao L.L., John H.St., Stambaugh R.D., Kellman A.G., Pfeiffer W. (1985) Reconstruction of current profile parameters and plasma shapes in tokamaks. *Nuclear Fusion* 25:1611–1622
13. Sartori F., Cenedese A., Milani F. (2003) JET real-time object-oriented code for plasma boundary reconstruction. *Fusion Engineering and Design* 66–68:735–739
14. Robinson D.C., Wootton A.J. (1978) An experimental study of tokamak plasmas with vertically elongated cross-sections. *Nuclear Fusion* 18:1555–1567
15. Blum J., Le Foll J., Thooris B. (1981) The self-consistent equilibrium and diffusion code SCED. *Computer Physics Communications* 24:235–254
16. Rebhan E., Salat A. (1978) Feedback stabilization of axisymmetric MHD instabilities in tokamaks. *Nuclear Fusion* 18:1431–1444
17. Jardin S.C., Larrabee D.A. (1982) Feedback stabilization of rigid axisymmetric modes in tokamaks. *Nuclear Fusion* 22:1095–1098

18. Moriyama S., Nakamura K., Nakamura Y., Itoh S. (1985) Analysis of optimal feedback control of vertical plasma position in a tokamak system. *Japanese Journal of Applied Physics* 24:849–855
19. Al-Husari M.M.M., Hendel B., Jaimoukha I.M., Kasenally E.M., Limebeer D.J.N. (1991) Vertical Stabilization of Tokamak Plasmas. *Proc. 30th IEEE Conference on Decision and Control*, Brighton (UK)
20. Gossner J.R., Vyas P., Kouvaritakis B., Morris A.W. (1999) Application of cautious stable predictive control to vertical positioning in COMPASS-D tokamak. *IEEE Trans. on Control Systems Technology* 7:580–587
21. Lennholm M., Campbell D., Milani F., Puppini S., Sartori F., Tubbing B. (1997) Plasma vertical stabilisation at JET using adaptive gain adjustment. *Proc. 17th IEEE/NPSS Symposium on Fusion Engineering*, San Diego (CA)
22. Neilson G.H., Dyer G.R., Edmonds P.H. (1984) A model for coupled plasma current and position feedback control in the ISX-B tokamak. *Nuclear Fusion* 24:1291–1302
23. Mori M., Suzuki N., Shoji T., Yanagisawa I., Tani T., Matsuzaki Y. (1987) Stability limit of feedback control of vertical plasma position in the JFT-2M tokamak. *Nuclear Fusion* 18:1555–1567
24. Albanese R., Coccoresse V., Rubinacci G. (1989) Plasma modeling for the control of vertical instabilities. *Nuclear Fusion* 29:1013–1023
25. Ward D.J., Hofmann F. (1994) Active feedback stabilization of axisymmetric modes in highly elongated tokamak plasmas. *Nuclear Fusion* 34:401–415
26. Humphreys D.A., Hutchinson I.H. (1993) Axisymmetric magnetic control design in tokamaks using perturbed plasma equilibrium response modeling. *Fusion Technology* 23:167–184
27. Vyas P., Morris A.W., Mustafa D. (1998) Vertical Position Control on COMPASS-D. *Fusion Technology* 33:97–105
28. Scibile L., Kouvaritakis B. (2001) A discrete adaptive near-time optimum control for the plasma vertical position in a Tokamak. *IEEE Transactions on Control Systems Technology* 9:148–162
29. Schuster E., Walker M.L., Humphreys D.A., Krstić M. (2005) Plasma vertical stabilization with actuation constraints in the DIII-D tokamak. *Automatica* 41:1173–1179
30. Morelli J.E., Hirose A., Wood H.C. (2005) Fuzzy-Logic-Based Plasma-Position Controller for STOR-M. *IEEE Transactions on Control Systems Technology* 13:328–337
31. Walker M.L., Humphreys D.A. (2006) A Multivariable Analysis of the Plasma Vertical Instability in Tokamaks. *Proceedings of the 45th IEEE Conference on Decision and Control*, San Diego (CA)
32. Gran R., Rossi M.J., Sobierajski F. (1977) Plasma position control for TFTR using modern control theory. *Proc. of 17th Symposium on Engineering Problems of Fusion Research*, Knoxville, TN
33. Firestone M.A. (1982) Analysis of modern optimal control theory applied to plasma position and current control in TFTR. *IEEE Trans. on Plasma Science* 10:105–115
34. Walker M.L., Humphreys D.A., Leuer J.A., Ferron J.R. (1999) Development of Multivariable Control Techniques for Use with the DIII-D Plasma Control System. *General Atomics Tech. Report GA-A23151*, San Diego (CA)

35. Ambrosino G., Ariola M., Pironti A., Lister J.B., Vyas P. (1998) A Model Based Controller Design Approach for the TCV Tokamak. Proc. 1998 IEEE International Conference on Control Applications, 202–206, Trieste (I)
36. Ariola M., Ambrosino G., Lister J.B., Pironti A., Villone F., Vyas P. (1999) A Modern Plasma Controller Tested on the TCV Tokamak. *Fusion Technology* 36:126–138
37. Ariola M., Pironti A. (2005) Plasma Shape Control for the JET Tokamak. *IEEE Control Systems Magazine* 25:65–75
38. De Tommasi G. *et al.* (2007) XSC Tools: A Software Suite for Tokamak Plasma Shape Control Design and Validation. *IEEE Transactions on Plasma Science* 35:709–723
39. Ambrosino G. *et al.* (2008) Plasma strike-points sweeping on JET tokamak with the eXtreme Shape Controller. *IEEE Transactions on Plasma Science*. To appear
40. Ariola M. *et al.* (2008) Integrated plasma shape and boundary flux control on JET tokamak. *Fusion Science & Technology* 53:789–805
41. Shafranov V.D. (1966) Plasma equilibrium in a magnetic field. *Reviews of Plasma Physics* 2:103–151
42. Freidberg J.P. (1982) Ideal magnetohydrodynamic theory of magnetic fusion systems. *Review of Modern Physics* 54:902
43. Albanese R., Rubinacci G. (1988) Integral formulation for 3D eddy-current computation using edge elements. *IEE Proceedings A. Physical Science, Measurements and Instrumentation, Management and Education, Reviews* 135:457–462
44. Lackner K. (1976) Computation of ideal MHD equilibria. *Computer Physics Communications* 12:33–44
45. Jardin S.C., Pomphrey N., De Lucia J. (1986) Dynamic modeling of transport and positional control of tokamaks. *Journal of Computational Physics* 66:481–507
46. Albanese R., Blum J., De Barbieri O. (1987) Numerical studies of the next european torus via the PROTEUS Code. Proc. of 12th Conference on Numerical Simulation of Plasmas, S. Francisco (CA)
47. Hofmann F. (1988) FBT A Free-Boundary Tokamak Equilibrium Code for Highly Elongated and Shaped Plasmas. *Computer Physics Communications* 48:207–221
48. Albanese R., Villone F. (1998) The linearized CREATE-L plasma response model for the control of current, position and shape in tokamaks. *Nuclear Fusion* 28:723–738
49. Luxon J.L., Brown B.B. (1982) Magnetic Analysis of Non-Circular Cross-Section Tokamaks. *Nuclear Fusion* 22:813–821
50. Deshko G.N., Kilovataya T.G., Kuznetsov Y.K., Pyatov V.N., Yasin I.V. (1983) Determination of the plasma column shape in a tokamak from magnetic measurements. *Nuclear Fusion* 23:1309–1317
51. Blum J. (1989) *Numerical Simulation and Optimal Control in Plasma Physics*. Wiley-Interscience, Chichester
52. Equipe TFR (1978) Tokamak plasma diagnostics. *Nuclear Fusion* 18:647–731
53. Hutchinson I.H. (1987) *Principles of Plasma Diagnostics*. Cambridge University Press, Cambridge
54. Braams B.J. (1991) The interpretation of tokamak magnetic diagnostics. *Plasma Physics and Controlled Fusion* 33:715–748

55. Thikhonov A.N., Arsenin V.Y. (1977) Solutions of Ill-Posed Problems. V.H. Winston & Sons, Washington DC
56. Kurihara K. (1990) Tokamak plasma shape identification with a Legendre-Fourier expansion of the vacuum poloidal flux function in the toroidal coordinates. ITER Specialist Meeting. Garching
57. Ambrosino G., Celentano G., Garofalo F., Glielmo L., Pironti A. (1992) On-line plasma shape identification via magnetic measurements. IEEE Transactions on Magnetics 28:1601–1604
58. Pironti A., Amato F. (1995) On-Line Plasma Shape Identification for Use in Control Systems. Proc. of the 4th IEEE Conference on Control Applications, Albany (NY)
59. Swain D.W., Neilson G.H. (1982) An Efficient Technique for Magnetic Analysis of Noncircular, High-Beta Tokamak Equilibria. Nuclear Fusion 22:1015–1030
60. Wotton A.J. (1979) Measurements of Plasma Shape in a Tokamak. Nuclear Fusion 19:987–990
61. O'Reilly J. (1983) Observers for Linear Systems. Academic Press, London
62. Albanese R., Ambrosino G., Celentano G., Garofalo F., Glielmo L., Martone R., Pironti A., Rubinacci G. (1992) Effects of the eddy current for some design and interpretation problem in a tokamak. Proceedings of 17th Symposium on Fusion Technology, Rome (IT)
63. Nagpal M., Khargonekar P.P. (1991) Filtering and Smoothing in an  $H_\infty$  Setting. IEEE Transactions on Automatic Control 36:152–166.
64. Khargonekar P.P., Rotea M.A. (1991) Mixed  $H_2/H_\infty$  Control Problem: A Convex Optimization Approach. IEEE Transactions on Automatic Control 36:824–837
65. Jardin S.C., Kessel C.E., Pomphrey H. (1994) Poloidal Flux Linkage Requirements for the International Thermonuclear Experiment Reactor. Nuclear Fusion 34:1145–1160
66. Bateman G. (1978) MHD Instabilities. MIT Press
67. Pironti A., Portone A. (1998) Optimal choice of the geometrical descriptors for tokamak plasma shape control. Fusion Engineering and Design 43:115–127
68. Albanese R., Ambrosino G., Ariola M., Calabrò G., Cocilovo V., Crisanti F., Pironti A., Villone F. (2003) Plasma modeling for position and current control in FTU. Fusion Engineering and Design 66–68:681–689
69. Doyle J.C., Francis B.A., Tannenbaum A.R. (1992) Feedback Control Theory. Macmillan Publishing Company. New York.
70. Zhou K., Doyle J.C., Glover K. (1996) Robust and Optimal Control. Prentice Hall Inc., Upper Saddle River, New Jersey
71. Sánchez Peña R.C., Sznaier M. (1998) Robust Systems: Theory and Applications. John Wiley & Sons, Inc.
72. Moore B.C. (1981) Principal component analysis in linear systems: controllability, observability, and model reduction. IEEE Transactions on Automatic Control 35:17–32
73. Kokotović P., Khalil H.K., O'Reilly J. (1986) Singular Perturbation Methods in Control: Analysis and Design. Academic Press
74. Lister J.B. *et al.* (1997) The Control of TCV Plasmas. Fusion Technology 32:321–373
75. Hofmann F., Tonetti G. (1988) Tokamak Equilibrium Reconstruction using Faraday Rotation Measurements. Nuclear Fusion 28:1871–1878

76. Balas G., Chiang R., Packard A., Safonov M. (2007) Robust Control Toolbox 3, User's Guide. The MathWorks Inc., Natick (MA)
77. Franklin G.F., Powell J.D., Workman M.L. (1998) Digital Control of Dynamic Systems. Addison-Wesley Publishing Company. Third edition
78. Crisanti F. *et al.* (2003) Upgrade of the present JET shape and vertical stability controller. Fusion Engineering and Design 66–68:803–807
79. Wesson J. (2000) The Science of JET. JET Joint Undertaking, Abingdon, Oxon. Available at <http://www.jet.efda.org/documents/wesson/wesson.html>
80. Pamela J. *et al.* (2003) Overview of JET results. Nuclear Fusion 42:1540–1554
81. Albanese R., Calabrò G., Mattei M., Villone F. (2003) Plasma response models for current, shape and position control in JET. Fusion Engineering and Design 66–68:715–718
82. Garibba M., Litunovsky R., Noll P., Puppini S. (1996) The new control scheme for the JET plasma position and current control system. Proceedings of the 15th SOFE Conference, Lisbon
83. Ambrosino G., Ariola M., Pironti A. (2007) Optimal steady-state control for linear non right-invertible systems. IET Proc. Control Theory & Applications 1:604–610
84. Davison E.J. (1975) A Generalization of the Output Control of Linear Multivariable Systems with Unmeasurable Arbitrary Disturbances. IEEE Transactions on Automatic Control 20:788–792
85. Francis B.A. (1977) The linear multivariable regulator problem. SIAM Journal on Control and Optimization 15:486–505
86. Saberi A., Stoorvogel A., Sannuti P., Shi G. (2003) On optimal output regulation for linear systems. International Journal of Control 76:319–333
87. Morse P.M., Feshbach H. (1953) Methods of Theoretical Physics. McGraw-Hill, New York
88. Abramowitz M., Stegun I.A. (1964) Handbook of mathematical functions. National Bureau of Standards, Washington DC
89. Carlson B.C. (1977) Special Functions of Applied Mathematics. Academic Press, New York
90. Numerical Algorithm Group (1983) NAG Fortran Manual for Mark 10. Numerical Algorithm Group, Oxford
91. Korn G.A., Korn T.M. (1961) Mathematical Handbook for Scientists and Engineers. McGraw-Hill, New York
92. Edèrlyi A., Magnus W., Oberhettinger F., Tricomi F.G. (1953) Higher Transcendental Functions. Vol. II. McGraw-Hill, New York
93. Hadamard J. (1923) Lectures on the Cauchy Problem in Linear Partial Differential Equations. Yale University Press, New Haven (CT)

---

# Index

- Ampere's law 26
- Amplification factor 7
- ASDEX 62
  
- Baffles *see* Plasma baffles
- Blanket *see* Tokamak blanket
- Boundary flux control *see* Plasma  
boundary flux control
- Break-even 8
- Breakdown phase 65
- Bremsstrahlung 7
  
- Confinement
  - gravitational 4
  - inertial 4
  - magnetic 4
- Constitutive relations 26
- Controller
  - $H_\infty$  17, 18, 20, 77, 96, 115, 117, 118,  
121, 122
  - LQ 17, 18
  - PD 17–19
  - PI 99, 104, 138
  - PID 19, 72, 84, 86, 96–98, 111, 118,  
121
- DIID-D 10, 19
- Divertor plasma 44, 46
  
- Eddy currents 35, 60
- electronvolt 4, 152
- Elongation 47
- Energy confinement time 7
- Extreme shape controller 20, 77, 125
  
- Faraday's law 26
- First wall *see* Tokamak first wall
- Flat-top phase 65
- Flux
  - function *see* Poloidal flux function
  - loops 50
- FTU 10, 19, 75, 76, 78–86
  
- Gap *see* Plasma gap
- Gauss's law 26
- Geometrical descriptors *see* Plasma  
geometrical descriptors
- Grad-Shafranov equation 37, 54, 144
- Green's functions 32, 40, 56–58, 60,  
143, 145
  
- Ignition 8
- Ill-posed problems 54
- Inductance matrix 34
  - modified 42
- Inner radius *see* Plasma inner radius
- ITER xi–xiii, 10, 14, 18, 60, 61, 71, 73,  
75, 77, 89–91, 93, 99–106
  
- JET xiii, 8, 10, 13, 20, 21, 71, 75, 77,  
100, 124–141
- JT-60 8
  
- Lawson's criterion 9
- Limiter plasma 44, 45
- Lorentz force 25
  
- Magnetic measurements 50
- Magnetohydrodynamics (MHD) 25

- Major radius *see* Plasma major radius
- Mass conservation law 25
- Maxwell's equations 26
- Measurement contour 53
- Minor radius *see* Plasma minor radius
- Newton's law 25
- Nuclear
  - fission 2
  - fusion 2, 5, 7, 8
  - reaction cross-section 4, 5, 7
  - reactions 4, 8
  - reactor 8
- Null point *see* Plasma X-point
- Observer 18, 62
  - $H_2/H_\infty$  62
- Ohm's law 30
- Outer radius *see* Plasma outer radius
- Pick-up coils 51
- Plasma 3
  - accessible region 47
  - baffle 44
  - boundary 44
  - boundary flux control 20
  - cross-section 12, 19, 36, 47, 66, 69, 76, 79
  - current 38
  - current centroid 39, 47
  - discharge 65
  - elongation 49
  - equilibrium 35–37
  - gap 49
  - geometrical descriptors 49
  - inner radius 48
  - linearized model 40
  - major radius 48
  - maximum height 48
  - minimum height 48
  - minor radius 48
  - outer radius 48
  - radial position 47
  - scenario 11, 12, 20
  - separatrix 44
  - shape
    - control 19, 68, 69, 72
    - estimation *see* Plasma shape
    - identification
      - 16, 53, 55
    - strike point 21, 44
      - sweeping 21
    - triangularity 49
    - vertical position 47
    - vertical stabilization 16, 72, 89–98
    - X-point 44
- Poloidal
  - beta 38
  - field coils 10, 25
  - flux function 27, 32, 40, 44, 56, 143, 144
  - magnetic field 28, 29
  - plane 27
- Poloidal coils *see* Toroidal field coils
- Ramp-down phase 65
- Ramp-up phase 65
- Reaction rate 7
- Reactivity 7
- Resistance matrix 34
- Rogowski coil 51
- Saddle loops 51
- Strike points *see* Plasma strike points
- Sweeping *see* Plasma strike point
  - sweeping
- TCV xiii, 10, 18, 71, 73, 75, 77, 89, 93–98, 110–122
- Tokamak 1, 9–12
  - blanket 6, 7, 10
  - diagnostics *see* Magnetic measurements
  - divertors 44
  - electromagnetic model 30
  - first wall 44, 45
  - vacuum vessel 10, 11
- Toroidal
  - angle 26
  - coordinates 145
  - current density 29, 38
  - direction 27
  - field coils 10
  - filament 57, 144
  - geometry 26
  - harmonics 55, 56, 146
  - magnetic field 29
- Toroidal coils *see* Poloidal field coils



- TOSCA 16
- Triangularity 47
- Vacuum vessel *see* Tokamak vacuum vessel
- Vertical stabilization *see* Plasma vertical stabilization
- X-point *see* Plasma X-point
- XSC *see* Extreme shape controller

### Other titles published in this series (continued):

*Soft Sensors for Monitoring and Control of Industrial Processes*

Luigi Fortuna, Salvatore Graziani,  
Alessandro Rizzo and Maria G. Xibilia

*Adaptive Voltage Control in Power Systems*

Giuseppe Fusco and Mario Russo

*Advanced Control of Industrial Processes*

Piotr Tatjewski

*Process Control Performance Assessment*

Andrzej W. Ordys, Damien Uduchi and  
Michael A. Johnson (Eds.)

*Modelling and Analysis of Hybrid Supervisory Systems*

Emilia Villani, Paulo E. Miyagi and  
Robert Valette

*Process Control*

Jie Bao and Peter L. Lee

*Distributed Embedded Control Systems*

Matjaž Colnarič, Domen Verber and  
Wolfgang A. Halang

*Precision Motion Control* (2nd Ed.)

Tan Kok Kiong, Lee Tong Heng and  
Huang Sunan

*Optimal Control of Wind Energy Systems*

Iulian Munteanu, Antoneta Iuliana Bratcu,  
Nicolaos-Antonio Cutululis and Emil  
Ceangă

*Identification of Continuous-time Models from Sampled Data*

Hugues Garnier and Liuping Wang (Eds.)

*Model-based Process Supervision*

Arun K. Samantaray and  
Belkacem Bouamama

*Diagnosis of Process Nonlinearities and Valve Stiction*

M.A.A. Shoukat Choudhury, Sirish L.  
Shah, and Nina F. Thornhill

*Model Predictive Control Design and Implementation Using MATLAB®*

Liuping Wang  
Publication due October 2008

*Real-time Iterative Learning Control*

Xu Jian-Xin, Sanjib K. Panda and Lee  
Tong Heng  
Publication due November 2008

*Design of Fault-tolerant Control Systems*

Hassan Noura, Didier Theilliol,  
Jean-Christophe Ponsart and Abbas  
Chamseddine  
Publication due January 2009

*Dry Clutch Control for Automated Manual Transmission Vehicles*

Pietro J. Dolcini, Carlos Canudas-de-Wit  
and Hubert Béchart  
Publication due May 2009